Population Balance Modelling of Colloidal Aggregates in Laminar Shear Flow

by

Ricardo Andrade Rossi

A thesis submitted in partial fulfillment of the requirements for the degree of

Master of Science

in

Chemical Engineering

Department of Chemical and Materials Engineering

University of Alberta

Abstract

Shear-induced aggregation is an important process in the solid-liquid separation of colloidal particles, i.e., solid particles in the micron size range. In this process, the solid particles are mixed with chemical destabilizers in shear flow to induce the formation of aggregates or flocs, which are easier to separate than individual particles due to their larger size. Depending on the shear rate of the system, the hydrodynamic forces acting on flocs can break them into smaller fragments or induce their restructuring, which leads to the formation of small compact flocs. Aggregate breakage is an undesirable process because it decreases the efficiency of industrial solid-liquid separation systems. In order to prevent floc breakage and enhance the control of the final aggregate size and structure from shear-induced aggregation, it is crucial to quantitatively understand the restructuring and breakage mechanisms in shear flows. Therefore, the objective of the present work is to investigate the breakage and restructuring of populations of aggregates in laminar shear flow via a statistical approach.

A population balance model (PBM) was developed to predict the evolution of the average aggregate size, the floc size distribution, and the morphology of populations of aggregates from breakage experiments that were conducted in a previous study (Gustavo Cifuentes, Aggregate Breakage in Laminar Couette Flow, 2022). These experiments were performed in a Taylor-Couette cell at laminar flow conditions. The aggregates were composed of 2 μm latex spheres, and they were formed in a neutrally buoyant fluid-particle system at a shear rate of 17.6 s^{-1}. Then, the breakage and restructuring of aggregates were facilitated by doing a step increase in the shear rate to values ranging from 28.9 s^{-1} to 86.8 s^{-1}.

The current work focused on modelling the behaviour of floc populations after the step increase in the shear rate from Cifuentes' breakage experiments. The results from this work

proved that the breakage and restructuring of aggregates in laminar flow can be modelled via PBM. It was observed that the shear-induced breakage mechanism of relatively compact aggregates ($D_f \geq 2.2$) is non-uniform, i.e., fragments of different sizes have different probabilities of occurring. Additionally, the scaling exponent from the aggregate strength power-law relationship $R_g^{ss} \propto \dot{\gamma}^{-p}$ was proved to be $p = 0.5$. The local shear rate ($G_{b,i}$) required to break an aggregate of size $R_{g,i}$ was shown to scale with the floc population Reynolds number at steady-state, i.e., $G_{b,i} \propto \mathrm{Re}_{D_{32}}^{ss}$. This relationship can be used to estimate the fitting parameter B of the breakage kernel in PBM simulations. Regarding the modelling of floc collisions, it was noticed that floc permeability must be considered in order to produce accurate predictions of the floc size distribution. Lastly, the initial aggregate restructuring after the step increase in shear rate from Cifuentes' experiments can be assumed to be instantaneous, i.e., it occurs much faster than the observed time scale and measurement sampling time. This assumption allows the PBM to model the long-term floc restructuring and to produce better predictions of the evolution of average floc size and size distribution over time for different shear rates.

To my mother

For committing her entire life to giving me an excellent education.

Acknowledgements

I want to start by expressing my sincere appreciation to my supervisors, Prof. Sean Sanders and Dr. Jean-Sébastien Kroll-Rabotin. I had the great privilege to work under the supervision of these two amazing professionals and human beings, who constantly encouraged and trusted me with this research project. This thesis would not have been accomplished without them.

To Prof. Sanders, thank you for giving me the opportunity to do an MSc at the renowned University of Alberta, and for always keeping the safety and mental health of students the top priority in your research group. Also, thank you for sharing your passion for teaching with me and for giving me the opportunity to be your teacher assistant on multiple occasions. Thank you for showing me the value of communicating research in an interesting and understandable way. Lastly, thank you for your patience and guidance in my MSc project. I am eternally grateful for this professional experience.

To Dr. Kroll-Rabotin, thank you for your immense technical support and input in the development of the numerical methods and interpretation of the results of my research project. Before I met you, Prof. Sanders said that it would be a miracle for me to work with you. Now I understand why: you have a singular way of approaching physical problems from a practical mathematical standpoint. Your technical brilliance has inspired me to pursue this research project and to do my absolute best to extract meaningful results from it. I am really proud of the results of this work and I owe most of that to you.

I would like to thank my colleagues from the Pipeline Transport Processes research group, for making this journey exciting and enjoyable. To Dr. Akash Saxena, thank you for introducing me to the topic of my research project and for your patience in explaining your work to me. To Gustavo Cifuentes, thank you for teaching me in detail how your experiments were conducted and for facilitating access to your experimental data: my work could not have been done without it. I would like to thank my friend Sahil Sood for always being

there for me, and for the great conversations about work and life. I would like to show my appreciation to Aref Kangarshahi and Dr. Marcio Machado, for always providing me with great professional advice. I also would like to thank Terry Runyon for her administrative support throughout these years.

I am grateful to my wife Fernanda, whose love motivates me to be the greatest version of myself. Finally, I am thankful to my mother and grandmother for always putting my education in first place.

Contents

List of Tables

List of Figures

List of Symbols

Greek

$\alpha_{i,j}$	Collision efficiency, [−]
α^{i}	Collision efficiency of impermeable flocs, , [−]
α^{p}	Collision efficiency of permeable flocs, , [−]
$\beta_{i,j}$	Orthokinetic rectilinear collision kernel, $[\mathrm{m}^3 \cdot \mathrm{s}^{-1}]$
$\dot{\gamma}$	Shear rate, [−]
$\Gamma_{i,j}$	Breakage distribution function, [−]
ϵ_o	Vacuum permittivity, $[\mathrm{F} \cdot \mathrm{m}^{-1}]$
ϵ_r	Relative permittivity of the carrier fluid, [−]
$\iota_{k,i}$	percentage of a floc with k particles that is from i-th class size, [−]
κ_d^{-1}	Debye length, [m]
κ_i	Permeability of i-th class size floc, m^2
$\Lambda_{i,j}$	aggregation kernel, $[\mathrm{m}^3 \cdot \mathrm{s}^{-1}]$
$\lambda_{i,j}$	Size ratio of flocs from classes i and j, [−]
μ	Dynamic viscosity, $[\mathrm{Pa} \cdot \mathrm{s}]$
ν	Kinematic viscosity, $[\mathrm{m}^2 \cdot \mathrm{s}^{-1}]$
ξ_i	Dimensionless floc size based on permeability, [−]
ρ_f	Fluid density, $[\mathrm{kg} \cdot \mathrm{m}^{-3}]$
ρ_s	Solid density, $[\mathrm{kg} \cdot \mathrm{m}^{-3}]$
ϕ_i	Dimensionless density of i-th class size floc, [−]
Ψ_o	Surface potential, [V]

Roman

A	Floc area, $[\mathrm{m}^2]$
A^B	Aggregation birth term, $[\mathrm{m}^{-3} \cdot \mathrm{s}^{-1}]$
A^D	Aggregation death term, $[\mathrm{m}^{-3} \cdot \mathrm{s}^{-1}]$
A_h	Hamaker constant, $[\mathrm{N} \cdot \mathrm{m}]$
A_N	Avogadro number, $[\mathrm{mole}^{-1}]$
B	Fitting parameter of the breakage kernel, $[\mathrm{m}^4 \cdot \mathrm{s}^{-2}]$
B^B	Breakage birth term, $[\mathrm{m}^{-3} \cdot \mathrm{s}^{-1}]$
B^B	Breakage death term, $[\mathrm{m}^{-3} \cdot \mathrm{s}^{-1}]$

c_i	Molar concentration of $i-$type ion, $\mathrm{mol} \cdot \mathrm{m}^{-3}$
C_v	solids volume concentration, [−]
C_s	Shielding coefficient, [−]
d_{10}	Diameter of floc percentile 10 %, [m]
d_{50}	Diameter of floc percentile 50 %, [m]
d_{90}	Diameter of floc percentile 90 %, [m]
d_{gap}	Gap distance between cylinders of Taylor-Couette cell, [m]
d_o	Diameter of primary particle, [m]
D_{pq}	Weighted average size, [m]
D_{32}	Surface mean diameter, [m]
D_{43}	Volume mean diameter, [m]
D_f	Mass fractal dimension, [−]
$D_{f,ss}$	Mass fractal dimension at steady-state, [−]
$D_{p,f}$	Perimeter fractal dimension, [−]
e_c	Elementary charge of an electron, [C]
$f_{k,j}$	Fragments with k primary particles formed from the breakage of the j-th class floc, [−]
F_c	Cohesive (particle-particle) force, N
$\boldsymbol{F}_b$	External body force, [N]
F_{DLVO}	DLVO force, N
F_{EDL}	EDL force, N
F_{VDW}	VDW force, N
F_{viscous}	Viscous force, N
F_f	Hydrodynamic (fluid-particle) force, N
$Fl_{i,j}^{\mathrm{sp}}$	Flow number of solid particles, [−]
G	Average shear rate, $[\mathrm{s}^{-1}]$
$G_{b,i}$	Breakage shear rate of i-th class size floc, $[\mathrm{s}^{-1}]$
H	Surface-to-surface distance between particles, [m]
k_c	Proportionality constant related to the packing density, [−]
k_B	Boltzmann constant, $[\mathrm{J} \cdot \mathrm{K}]$
L	Floc length, [m]
M	Floc mass, [kg]
m_k	Moment of order k of the floc size distribution, $[\mathrm{m}^k]$
n'	Continuous number density, $[\mathrm{m}^{-3}]$
n_c	Total number of class sizes tracked by the MOC PBE, [−]
N_i	Number density from i-th class size, $[\mathrm{m}^{-3}]$
n_j^b	number of breakage scenarios for the j-th class floc, [−]
n_p	Number of primary particles in a floc, [−]
$n_{p,i}$	Number of primary particles from i-th class size floc, [−]
n_{pixel}	Number of pixels within a floc 2D picture, [−]
P	Floc perimeter, [m]
p	Scaling exponent of floc strength, [−]
Pe	Peclet number, [−]

r	Common ratio of geometric progression, [−]
r_o	Primary particle radius, [m]
r_i	Distance between primary particle and floc center of mass, [m]
Re_{agg}	Aggregate Reynolds number, [−]
$\mathrm{Re}_{D_{32}}$	Population Reynolds number, [−]
R_g	Radius of gyration, [m]
$R^*_{g,i}$	Dimensionless radius of gyration, [−]
R_g^{ss}	Radius of gyration at steady-state, [m]
R_{in}	Inner radius of Taylor-Couette cell, [m]
R_{out}	Outer radius of Taylor-Couette cell, [m]
s	Fitting parameter of breakage dist. funciton, [−]
S_i	Breakage kernel, [s^{-1}]
T	Absolute temperature, [K]
Ta_{cri}	Critical Taylor number, [−]
Ta	Taylor number, [−]
t_r^{-1}	Aggregate rate of restructuring, [s^{-1}]
$\vec{\boldsymbol{u}}$	Fluid velocity, [$\mathrm{m} \cdot \mathrm{s}^{-1}$]
w_i	Weight of FSD of QMOM approach, [−]
$w_{k,j}$	Fragment size probability, [−]
w_{in}	Angular velocity of inner cylinder of Taylor-Couette cell, [$\mathrm{rad} \cdot \mathrm{s}^{-1}$]
z	Valency of the counter-ion

Acronyms

CCC	Critical Coagulation Concentration
CFD	Computational Fluid Dynamics
DLVO	Derjaguin-Landau-Verwey-Overbeek
EDL	Electric Double Layer
FSD	Floc size distribution
MOC	Method of Classes
ODE	Ordinary differential Equation
PBE	Population Balance Equation
PBM	Population Balance Modelling
QMOM	Quadrature Method of Moments
VDW	Van Der Waals

Chapter 1

Introduction

1.1 Background and motivation

The separation efficiency of industrial fluid-particle systems is a key economic and environmental challenge because it is intrinsically related to water consumption, recovery and recycle [1] and the final product quality [2–4] in many processes. The properties of the dispersed solids, such as size and density, directly influence their separation efficiency from the fluid phase. For instance, solid-liquid separation processes, such as sedimentation, filtration, and flotation, are more efficient when they operate with larger, denser solid particles. When the solids are too small to guarantee an effective and timely separation, different chemicals can be added to facilitate the formation of conglomerates of solid particles, also known as aggregates or flocs [5], that are easier to separate from the liquid phase due to their larger size when compared to individual particles [6].

The aggregation process is often required in aqueous colloidal fluid-particle systems, where the size range of solid particles is between 1 nm and 1 μm [6]. These systems usually form stable dispersions, i.e., the solid particles tend to repel one another via electrostatic forces and do not aggregate [7]. Hence, to induce the formation of aggregates, the colloidal dispersion must first become unstable. This can be achieved by adding chemical destabilizers into the system, such as inorganic salts and polymer flocculants. The former reduces the repulsive forces that keep particles apart, allowing them to get sufficiently close to one another and form aggregates via attractive van der Waals forces, also referred as cohesive forces [8–10]. The latter adsorbs into the surface of the colloidal particles, acting as a bridge between them which also enables the formation of aggregates via cohesive forces [11].

Colloidal dispersions and chemical destabilizers are often mixed together to accelerate

the formation of aggregates, e.g., in stirred tanks [12] or pipelines [13]. The fluid motion in these systems has a two-fold effect: it increases the frequency of particle-particle collisions, accelerating aggregate formation [9]; and it changes the floc size and structure due to the presence of external fluid forces acting on the aggregate [10]. If the hydrodynamic forces acting on the floc (due to mixing) are significantly greater than the cohesive forces holding two particles together, the aggregate breaks into smaller fragments [10, 14], and thus may not longer have the desired size for efficient solid-liquid separation [15]. If the hydrodynamic forces (F_h) and the cohesive forces (F_c) are of similar order of magnitude, the primary particles, i.e., the solid particles that comprise the floc, can restructure to produce small compact aggregates, which are more difficult to break [10, 16]. The aggregation, restructuring and breakage mechanisms are illustrated in Figure 1.1.

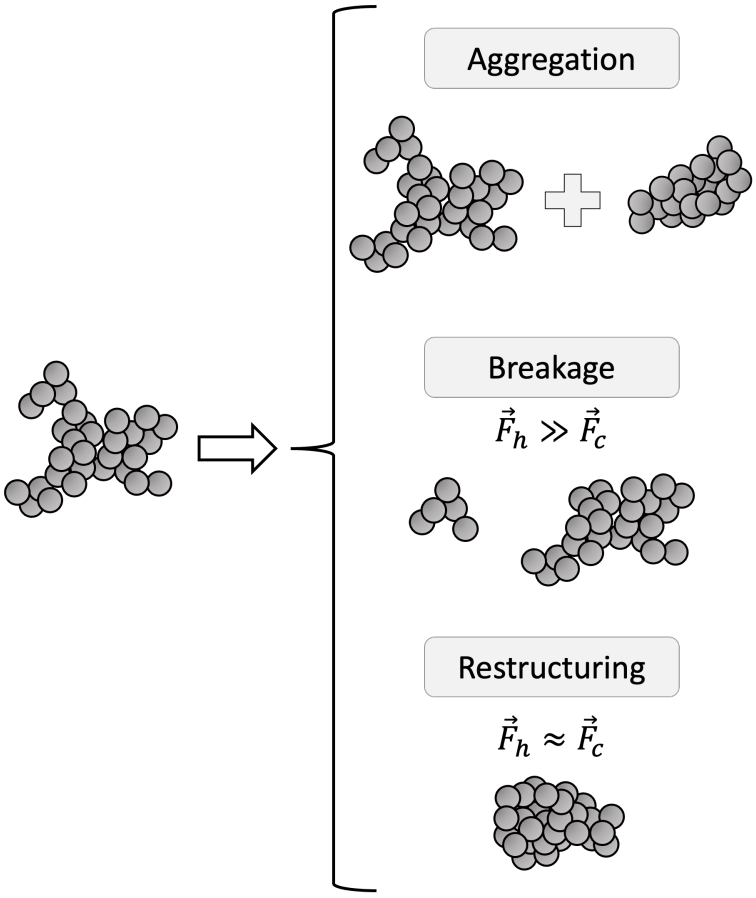

Figure 1.1: Effect of mixing in floc size and structure due to aggregation, restructuring ($F_h \approx F_c$), and breakage ($F_h \gg F_c$) mechanisms (modified from Cifuentes [17]).

In order to improve the design and control of aggregation systems, it is crucial to predict

how the floc size and morphology evolve over time [18, 19]. This can be achieved with population balance models (PBMs), which use mathematical equations to model the effect of aggregation, breakage, and restructuring mechanisms on the size and structure of populations of aggregates [20]. The PBM can provide crucial information, such as how the aggregate average size varies during aggregation for different mixing conditions and types of chemical destabilizers [11, 21, 22]. They can also be used to determine the optimal residence times of different solid-liquid separation units, which is essential in the design of such equipment [2, 11].

Aggregation control is essential in many industries, e.g., water treatment [4], papermaking [22], food processing [23], pharmaceutical manufacturing [24], metallurgy [2], and mining [11]. The following three subsections highlight how population balance models have been used to enhance the control and understanding of aggregation in different industries:

- Section 1.1.1 describes the role of aggregation in oil sands tailings treatment and how population balance can be used in a quantitative approach to monitor and control the tailings treatment process.
- Section 1.1.2 outlines how steel alloys can be purified via aggregation and how population balance models can be used to provide a deeper understanding of the aggregation mechanism.
- Section 1.1.3 describes the importance of aggregation in the papermaking industry and how the use of population balances can provide quantitative predictions describing the effect of chemical (flocculant) type and concentration on aggregate size.

1.1.1 Oil sands tailings treatment

In the oil sands industry, the extraction of bitumen from surface-mineable oil sands reserves requires large volumes of warm water, e.g., around 3 barrels of water are used to produce 1 barrel of refined bitumen from surface mining [25]. The waste produced from this extraction process is called tailings, which is composed of process water, coarse solids (sand), and fine solids (particles smaller than 44 μm) [26, 27]. The tailings are stored in ponds, where sand particles rapidly settle due to their relatively large size and density, and the fine solids remain suspended in water, creating a mud-like slurry known as Mature Fine Tailings (MFT). The MFT is a stable colloidal dispersion due to the repulsive forces that

keep the small solid particles apart and prevent them from aggregating [28]. Due to the slow settling velocity of the fine particles, the area occupied by the tailings ponds grows larger every year, increasing the risks of tailings leakage, groundwater contamination, or tailings ponds collapse [29, 30]. Therefore, tailings treatment is an important and challenging process in the oil sands industry because it is directly related to the area occupied by the tailings ponds and the volume of recycled water that can be recovered.

To accelerate the rate of water recycle/recovery and decrease the environmental risks posed by the tailings ponds, polymers flocculants are often mixed with the tailings to induce the formation of colloidal aggregates [1, 13, 31]. To quantitatively determine the best mixing condition and flocculant dosage for MFT aggregation, a recent population balance study was conducted by Vajihinejad and Soares [11]. Some of their results are displayed in Figure 1.2. As can be seen, their population balance model can accurately predict the experimental evolution of the average floc size for different flocculant dosages and average shear rates (G). The shear rate is a parameter that scales with the (mechanical) mixing intensity of the experiment equipment. These results reveal that larger aggregates are formed at lower shear rates and higher flocculant concentrations, and that the optimal mixing time is around 200 s. This is valuable information for controlling the final floc size and structure after aggregation.

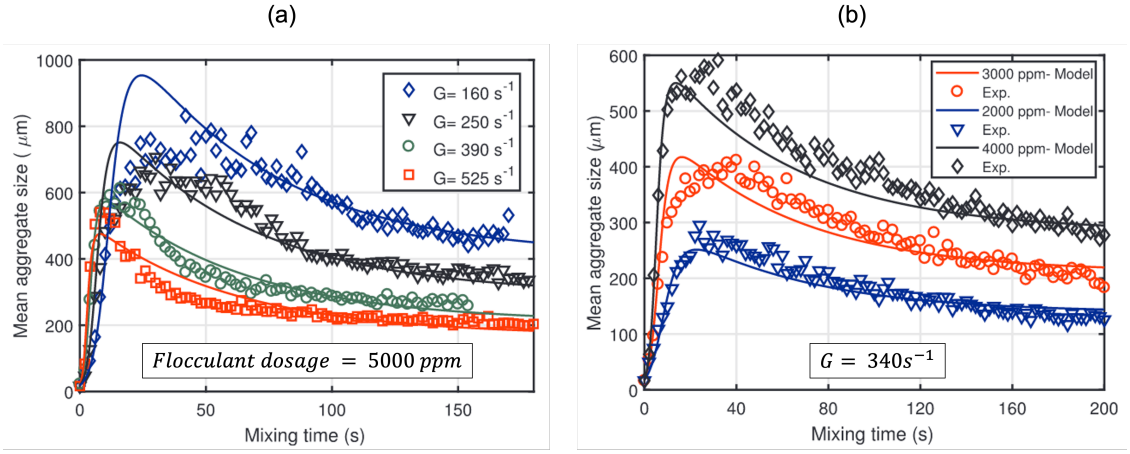

Figure 1.2: Effect of (a) average shear rate, G, and (b) flocculant dosage on the evolution of mean MFT aggregate size over time. The continuous lines correspond to population balance results and the symbols represent the experimental data points (modified from Vajihinejad and Soares [11]).

1.1.2 Steel alloy purification

Due to the increased range of steel applications, e.g., automotive industry, metal wires, pipelines, and pressure vessels, there has been a continuous increase in the demand and value for cleaner steel alloys over the last few decades [32]. One of the most significant challenges in obtaining high purity alloy involves the removal of non-metallic inclusions (NMI) from the liquid steel [2, 32]. The concentration, morphology, size distribution, and chemical nature of NMI can cause several problems in the steel quality, e.g., sulfide and oxide inclusions greatly affect the endurance and structural integrity of steel alloys. The size distribution of inclusions is especially important because large inclusions are extremely harmful to the mechanical properties of steel, e.g., major defects in the steel alloy can occur by the presence of a single large inclusion in the system [32]. Therefore, the purification process of steel alloys must minimize the NMI concentration and eliminate large inclusions from the metal.

The gas-stirred ladle treatment is a secondary metallurgy technique that is commonly used in the steel industry during which removal of NMI is achieved by flotation [2, 33]. As shown in Figure 1.3, the inert gas argon is injected through porous plugs at the bottom of the steel ladle, which contains liquid steel. As the gas bubbles flow upwards, they induce turbulence in the liquid, i.e., high shear rates, which increases the collision frequency between NMI particles and promotes the formation of aggregates. Since NMI are hydrophobic, their flocs easily attach to the gas bubbles that rise to the top of the ladle, where they can be removed from the liquid steel. Recent studies on the flotation of NMI successfully modelled this process by combining a population balance model with computation fluid dynamics (CFD) models [2, 33]. It was observed that the frequency of collisions between two particles dramatically decreases when there is a larger difference in the size of the colliding particles, and that the overall aggregation time is dictated by the collisions between particles of the same size. This type of study has the potential to predict the removal efficiency of NMI and their size distribution over time, which is valuable information for optimizing this flotation process.

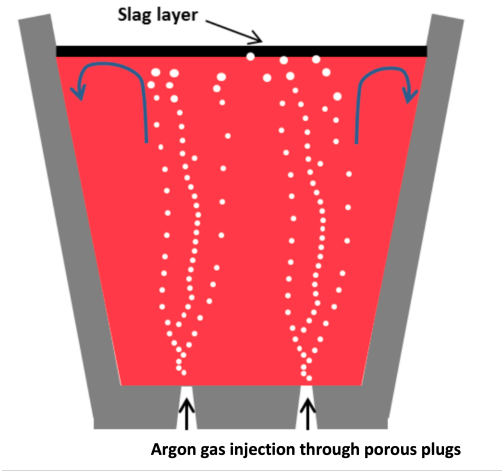

Figure 1.3: Schematic of liquid steel flotation unit (modified from Kroll-Rabotin et al. [2]).

1.1.3 Papermaking

In the papermaking industry, cellulosic fibre is mixed with water and chemical additives to produce different types of papers, e.g., cardboard boxes and printable paper sheets [34]. Precipitated calcium carbonate (PCC) is a key chemical additive in papermaking industry that significantly enhances the opacity and brightness of papers at relatively low cost [35]. As can be seen is Figure 1.4, the PCC particles fill the gaps between the fibres, changing the paper properties. To ensure that the PCC particles remain attached to fibre and do not disperse in water, they are aggregated with polymer flocculants. Due to their large size, the PCC aggregates easily attach to the paper sheet [34].

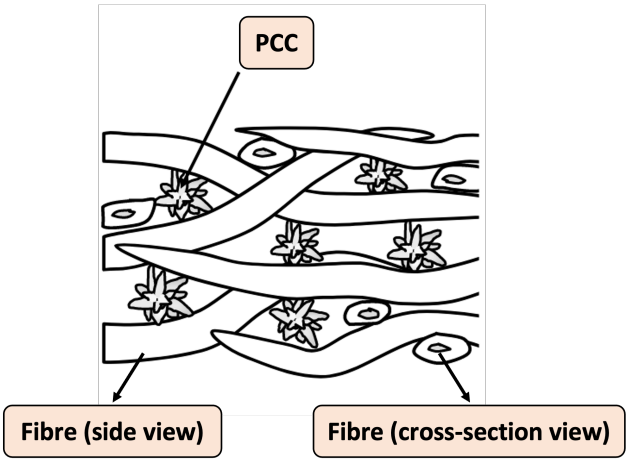

Figure 1.4: Illustration of PCC chemical additives filling the gaps between cellulosic fibres (modified from Hubbe and Gill [35])

Given the importance of PCC aggregation in the papermaking industry, Seghir et al. [22] successfully used population balance models to investigate the effect of different types and dosages of polymer flocculants on the evolution of PCC aggregate size with time. Some of their results are displayed in Figure 1.5. As can be seen, equal dosages of flocculants E1 and E2 result in very different median floc sizes (d_{50}). This information is critical for determining the optimal aggregation time and the best flocculant type and concentration for specific types of papers.

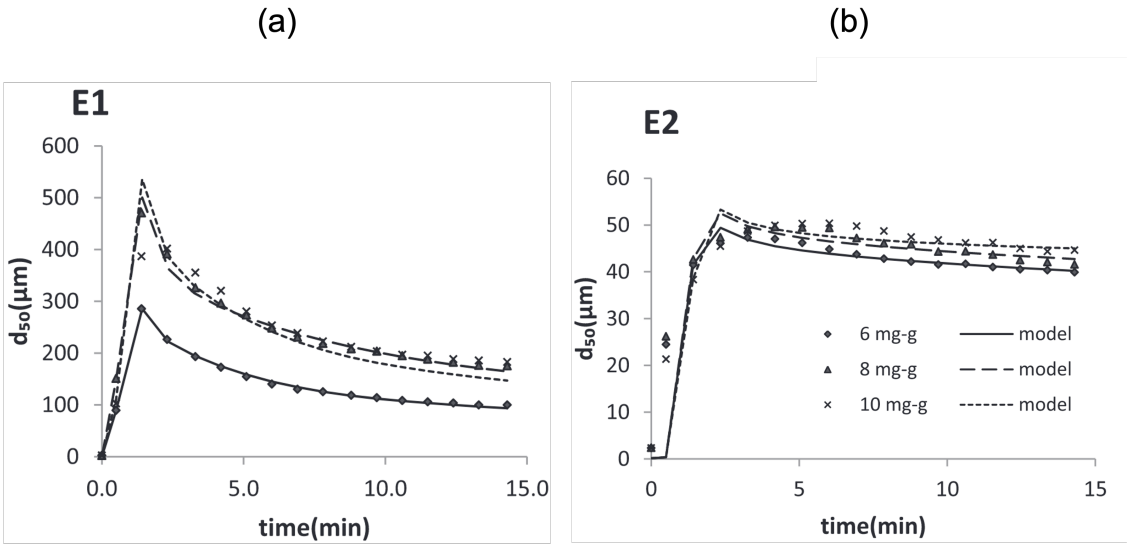

Figure 1.5: Evolution of median PCC aggregate size with time for different dosages of (a) E1 and (b) E2 polymer flocculants. The lines correspond to population balance results and the symbols are the experimental data points (modified from Seghir et al. [22])

1.2 Problem statement

As explained in Section 1.1, aggregation is a common step in solid-liquid separation processes when the solid particles are in the colloidal size range [6]. Additionally, the population balance model (PBM) is a valuable resource that can quantitatively predict the evolution of aggregate properties over time, and thus is often used to optimize aggregation in different industries [2, 11, 22]. Recent PBM studies have shown that shear-induced aggregation, i.e., the aggregation process where particles are mechanically mixed with chemical destabilizers, can be modelled via PBM by considering the combined effect of aggregation, breakage, and restructuring mechanisms [18, 36, 37]. It has been shown that the breakage frequency of aggregates increases with the shear rate, resulting in smaller flocs at the end of the aggregation

process. In industry, since most mixing processes (including pipeline transport) operate under turbulent conditions, i.e., very high shear rates, aggregate breakage is often unavoidable [38]. This size reduction often adversely impacts the separation efficiency of colloidal flocs [14].

In order to prevent the detrimental effect of floc breakage in solid-liquid separation, it is important to understand why and how breakage occurs at a fundamental level. Unfortunately, this cannot be done through investigations in turbulent flows because the hydrodynamic (fluid-particle) forces acting on the aggregate are highly variable [38], making it difficult to analyze their effect on floc size and structure. Hence, previous studies investigated the breakage and restructuring of aggregates under laminar shear flow conditions, i.e., relatively low shear rates, in which the hydrodynamic forces acting on the aggregates can be readily determined. For example, Blaser [39] investigated the evolution of single flocs via experiments, observing that aggregates experience periodic fluid forces that compress and stretch them, which leads to their restructuring and breakage. Later, Cifuentes [17] experimentally studied the breakage and restructuring of populations of aggregates in laminar flow, where aggregates were initially formed at low shear rates, after which a steep increase in the shear rate was applied to the system, which facilitated the breakage and restructuring of flocs. Among other findings, Cifuentes [17] observed that the fluid-particle force (F_h) acting on the flocs after breakage had a similar magnitude to the cohesive force between two primary particles (F_c). This suggests that large aggregates will break until the fluid-particle and particle-particle forces are balanced, i.e., $F_h \approx F_c$, and that the rupture of a single bond between two primary particles can lead to aggregate breakage. Cifuentes [17] also noticed via 2D image analysis that breakage occurs in the weakest link within the floc, as shown in Figure 1.6, but due to limitations in the image resolution, he was not able to confirm that this was the result of only a single bond failure between two primary particles.

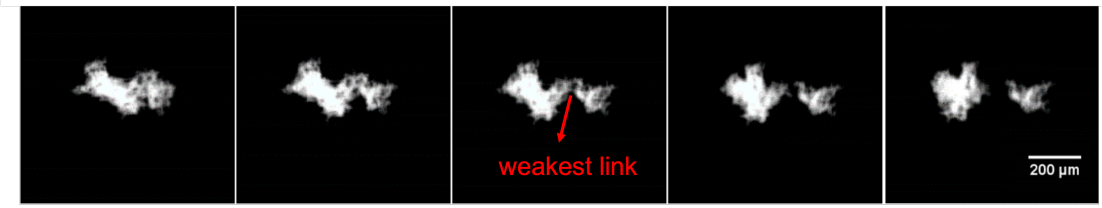

Figure 1.6: Floc breakage occurring in the weakest link within the aggregate (modified from Cifuentes [17])

The research findings from Cifuentes [17] were confirmed by Saxena et al. [10, 40], who investigated the breakage and restructuring of aggregates in laminar flow via computational simulations that can track fluid-particle and particle-particle interactions over time. This type of study can determine the exact moment that breakage occurs, as well as the size of the fragments formed after breakage. The simulation results confirmed that floc breakage is caused by the rupture of a single bond between primary particles. Saxena [40] also noticed that similar aggregates could form fragments of varying sizes, and that there was no particular preference for a certain fragment size. This is clearly illustrated in Figure 1.7, in which aggregates with equivalent initial size and structure broke into very different fragment sizes. This important finding goes against the simplifying assumption often made in PBMs that aggregates can only break into two fragments of equal sizes [11, 18, 19, 22, 36, 37, 41, 42].

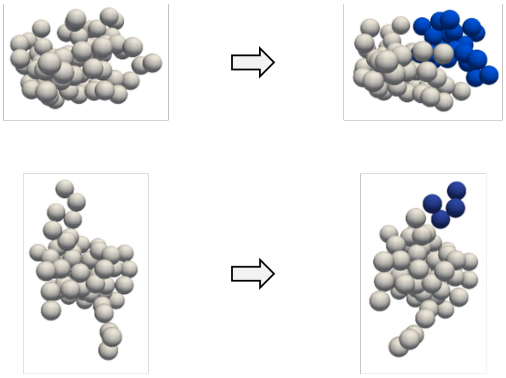

Figure 1.7: Different fragment sizes being formed from the breakage of aggregates of similar size and structure (modified from Saxena [40])

Since the results from Saxena et al. [10, 40] regarding fragment size are based on simulations that studied only 10 different aggregates, they cannot be extrapolated to an entire population of aggregates, but they can be validated via population balance modelling. To the author's knowledge, there are no population balance models that accounted for the latest findings in aggregate breakage. In fact, there are no population balance studies focused on the modelling of breakage experiments. To fill this research gap, the major objective of this research project is to investigate the breakage and restructuring of aggregates in laminar flow via population balance modelling.

1.3 Research objectives

The purpose of this research project is to study the breakage and restructuring mechanisms of colloidal aggregates in laminar shear flow. The principal objectives of this study are:

- To statistically investigate the effect of shear rate on the evolution of floc size and morphology over time;
- To determine how different physical parameters, such as shear rate and initial floc size and structure, influence the final size and morphology of aggregates after breakage.

To accomplish these objectives, the significant activities of this research project are the following:

- Improve the current approach to implementing PBMs for colloidal aggregation by developing new equations that incorporate the research findings from Saxena et al. [10, 40] regarding fragment size after breakage.
- Use the improved PBM to analyze Cifuentes' [17] breakage experiments in laminar flow.

1.4 Thesis outline

Chapter 1 provides the background and motivation of studying colloidal aggregation via population balance modelling. It also states the current research gaps concerning floc breakage and how this research project plans to address some of them.

Chapter 2 lays out the relevant information about colloidal aggregates that is crucial for understanding this work. This chapter also provides a critical evaluation of some of the the previous research on colloidal aggregation and breakage, and details the research gaps related to floc breakage.

Chapter 3 presents a summary of Cifuentes [17] breakage experiments and describes in detail the PBM that was used to model them. It also presents the new equations developed in this work based on Saxena et al. [10, 40] findings.

Chapter 4 compares the PBM results from this work and the experimental results from Cifuentes [17], and explains the important conclusions that can be extracted from this comparison.

Chapter 5 summarizes the significant findings from this research project and how future studies can use them to improve the current PBM that are focused on monitoring colloidal aggregation.

1.5 Significance of contributions

In the current work, the PBM from Selomulya et al. [18] was enhanced based on recent research publications related to aggregation, breakage, and restructuring of flocs in simple shear flow. New equations within the PBM were developed to improve the physical understanding of how floc breakage and aggregation occur in laminar shear flow. These equations also improved the PBM predictions of breakage experiments. For instance, the experimental evolution of the average aggregate size and floc size distributions over time at different shear rates were obtained via PBM with high accuracy. Additionally, the restructuring of aggregates in breakage experiments was also predicted by the modified PBM, where it was observed that the long-term restructuring of aggregates plays an important role in the PBM predictions of floc size. This modified PBM can be used in future research to model both aggregation and breakage experiments. This PBM can also be used in industry to improve the control of aggregation systems.

1.6 Author's contributions

In this research project, the author implemented and validated a population balance model for colloidal aggregates in laminar shear flows, planned case studies, performed simulations, and analyzed data. The author validated the numerical model developed here by comparing its results against experimental data from the literature. The author also developed a new breakage distribution function and collision efficiency equation with the help of his co-supervisor Dr. Kroll-Rabotin. The supervisors Prof. Sanders and Dr. Kroll-Rabotin provided invaluable support throughout the research project by giving constructive feedback on the model implementation and helping interpret the simulation results. The following list provides the detailed contribution of each author based the on the Elsevier Contributor Roles Taxonomy (CRediT) author statement:

- **PI. Prof. Sean Sanders (principal investigator)**: conceptualization, resources,

data curation, writing (review & editing), supervision, project administration, funding acquisition.

- **Dr. Kroll-Rabotin (co-supervisor)**: conceptualization, methodology, data curation, writing (review & editing), supervision.
- **Ricardo Andrade Rossi (MSc student)**: Conceptualization, methodology, software, validation, formal analysis, investigation, writing (original draft), visualization.

Chapter 2

Literature Review

As explained in Chapter 1, floc breakage is an undesirable phenomenon in shear-induced systems because it decreases the solid-liquid separation efficiency of different industrial processes [6]. To avoid aggregate breakage, or to be able to produce more robust aggregates, it is vital to quantitatively understand how aggregates break [10]. Therefore, the major objective of this current work is to investigate the breakage and restructuring of colloidal aggregates via a population balance model (PBM).

This chapter lays out the essential information that is required to understand the theory behind the application of PBMs in colloidal science and provides a critical evaluation of the current research on floc breakage and restructuring in sheared systems. The literature review is divided into five sections:

- Section 2.1 describes how the size and morphology of aggregates can be characterized in experiments and computational studies.
- Section 2.2 explains the inter-particle and fluid-particle forces that are present in colloidal systems and highlights their importance to developing PBM equations.
- Section 2.3 introduces how PBM works and describes the most common PBMs for shear-induced aggregation.
- Section 2.4 presents the latest research findings on floc breakup and restructuring in shear flow, and how they can be used to enhance the current PBMs.
- Section 2.5 summarizes the critical information provided in this chapter and the current knowledge gaps on floc breakage and restructuring. Then, the research scope of the present work is provided.

2.1 Aggregate characterization

To investigate how colloidal aggregates break and restructure in shear flow, it is necessary to measure their physical properties over time [10, 17]. Hence, this section describes how the floc morphology (Section 2.1.1) and size (Section 2.1.2) can be characterized in experiments, PBMs, and CFD simulations with single aggregates.

2.1.1 Morphology

When aggregates are composed of particles with identical size and chemical nature, they form fractals, i.e., self-similar structures that preserve their geometrical shape at different length scales [8, 18, 43]. Fractal aggregates can be described by the power-law relationship [44]

$$M \propto L^{D_f} \tag{2.1}$$

where M and L are the floc mass and size, respectively, and $D_f \in [1\ 3]$ is the mass fractal dimension, which is a dimensionless parameter that can retrieve information about the density and shape of aggregates. When $D_f = 1$, it represents the morphology of a straight rod of particles, and when $D_f = 3$, it denotes the structure of a highly compact sphere of particles [5, 45]. In shear-induced or orthokinetic aggregation, where the colloidal particles and chemical destabilizers are mechanically mixed, small compact flocs are formed, i.e., $2.2 \leq D_f \leq 2.7$ [9, 17, 46, 47]. In perikinetic aggregation, where particles collide via Brownian motion and there is no mechanical mixing, large porous aggregates are formed, i.e., $1.6 \leq D_f \leq 1.8$ [9, 43]. Figures 2.1 (a) and (b) illustrate the morphology difference of flocs produced via perikinetic aggregation and orthokinetic aggregation, respectively.

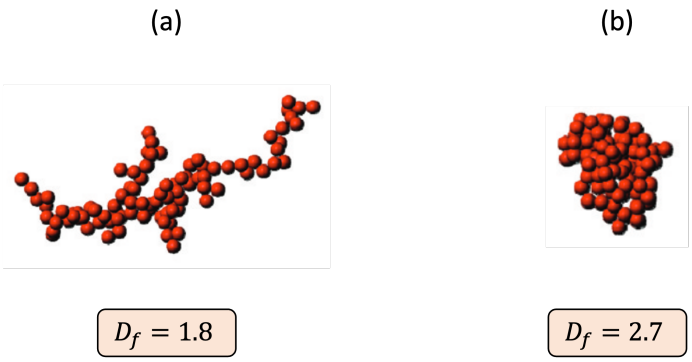

Figure 2.1: Illustration of different floc morphologies for (a) perikinetic aggregation and (b) orthokinetic (shear-induced) aggregation (modified from Harshe et al. [9]).

To investigate the evolution of floc morphology in aggregation and breakage experiments, D_f must be measured in situ, i.e., during the experiment [5, 17, 43, 46, 48, 49]. The most commonly used in situ technique is static light scattering, which determines D_f from a correlation with the intensity of the light that is scattered by a sample of aggregates [50]. Unfortunately, this method requires the pumping of aggregates from a controlled shear device to the light scattering equipment, which can affect the morphology of aggregates during measurements [5, 47]. To overcome this issue, a new image analysis technique that is both in situ and non-intrusive has been developed over the last couple of decades [17, 48, 51], which prevents any flow disturbance by directly monitoring the aggregates inside the controlled mixing device via 2D pictures. This experimental method was recently used in Cifuentes [17], whose results will be modelled via PBM in the current work. In 2D image analysis, D_f can be determined from the following correlation [52]:

$$D_f = -1.5 \times D_{pf} + 4.4 \tag{2.2}$$

where $D_{pf} \in [1\ 2]$ is the perimeter fractal dimension. This morphological parameter is similar to the mass fractal dimension, but it describes 2D objects, where $D_{pf} = 2$ denotes a straight rod of particles and $D_{pf} = 1$ represents a perfect disc of primary particles [53]. Equation (2.2) can be used for $D_f \in [1.7\ 2.9]$, and therefore it is generally taken to be suitable for shear-induced aggregation and breakage experiments, where $2.2 \leq D_f \leq 2.8$ [17]. In image analysis, D_{pf} is directly obtained via [51, 54]

$$A \propto P^{\,2/D_{pf}} \tag{2.3}$$

where A and P are the area and perimeter of the floc, respectively. As shown in Figure 2.2, D_{pf} is estimated from the slope of the log plot of A *vs.* P. Since each blue circle represents one floc, this technique can retrieve only the global morphology of a sample of aggregates, i.e., it cannot determine the D_f of each observed floc.

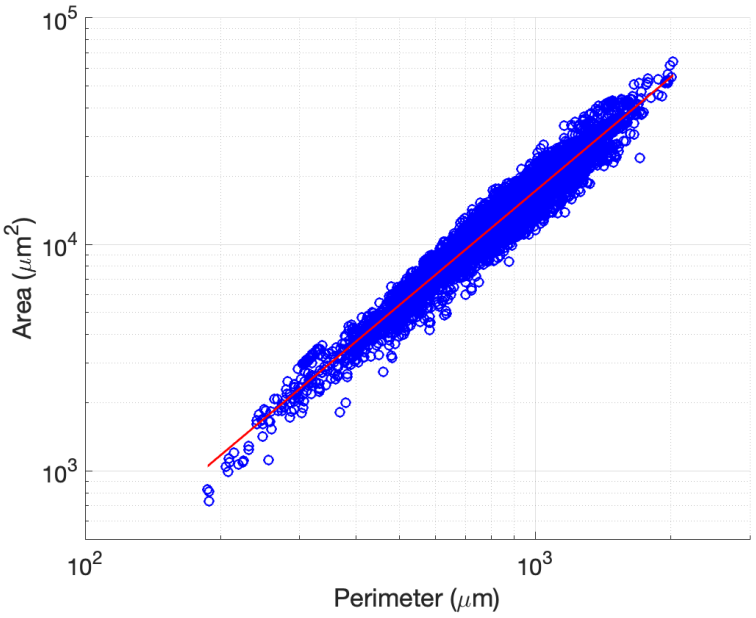

Figure 2.2: Example of D_{pf} calculation based on the slope of the logarithmic plot of Equation (2.3) (modified from Cifuentes [17]).

In the present work, the mass fractal dimension from Cifuentes' [17] breakage experiments is obtained via Equation 2.2, and the impact of using the global D_f to approximate the morphology of populations of aggregates is discussed in Chapter 4.

2.1.2 Size

The floc size is often characterized by the radius of gyration (R_g) [9, 10, 18, 43, 48, 55, 56], which is mathematically defined as [40]

$$R_g = \sqrt{\frac{1}{M}\int r^2 \mathrm{d}M} \tag{2.4}$$

where M is the floc mass and $\int r^2 \mathrm{d}M$ is the second mass moment around the floc center of mass. Given an aggregate with a total number of n_p identical primary particles of radii r_o,

if $R_g \gg r_o$, Equation (2.4) can be discretized as

$$R_g = \sqrt{\frac{\sum_{i=1}^{n_p} r_i^2}{n_p}} \tag{2.5}$$

where r_i is the distance between the primary particle i and the floc center of mass. Equation (2.5) is used in CFD simulations where the exact primary particle position is tracked over time, e.g., in Saxena et al. [10, 40], whose results will be used in the present work to improve current PBM equations.

In 2D image analysis, the specific primary particle location cannot be obtained due to limitations in the image resolution [17, 48, 51]. Hence, R_g is defined in terms of pixels [48],

$$R_g = \sqrt{\frac{\sum_{i=1}^{n_{\text{pixel}}} \left[(x_i - x_c)^2 + (y_i - y_c)^2 \right]}{n_{\text{pixel}}}} \tag{2.6}$$

where n_{pixel} is the total number of pixels within the floc perimeter in a 2D image, (x_i, y_i) are the i-th pixel coordinates, and (x_c, y_c) are the floc centroid coordinates. Since R_g can be experimentally measured for each observed aggregate, it is considered a local property as opposed to the experimentaly determined value of D_f, where a single value is used to represent the morphology of a population of aggregates at a given time. The radius of gyration can also be written in terms of mass fractal dimension [57],

$$R_g = r_o \left(\frac{n_p}{k_c} \right)^{1/D_f} \tag{2.7}$$

where k_c is a proportionality constant related to the packing density of the floc and is often assumed to be unity [18, 19, 36, 42]. Equation (2.7) is used in PBMs to account for the fractal nature of aggregates in the aggregation and breakage mechanisms [18, 20]. This equation is also used in CFD simulations of single aggregates to calculate their fractal dimension.

Aggregates usually present a broad distribution of sizes that can be characterized via percentiles or weighted average sizes [17, 18, 46]. The percentile is a statistical measure that indicates the value below which a certain percentage of the distribution is observed [58], e.g., the percentile d_{50} corresponds to the aggregate diameter below which 50% of the observations are found. Figure 2.3 demonstrates the use of percentiles d_{10}, d_{50}, and d_{90} to characterize an aggregate size distribution. As can be seen, these three values provide a essential information about the range of floc sizes within the distribution.

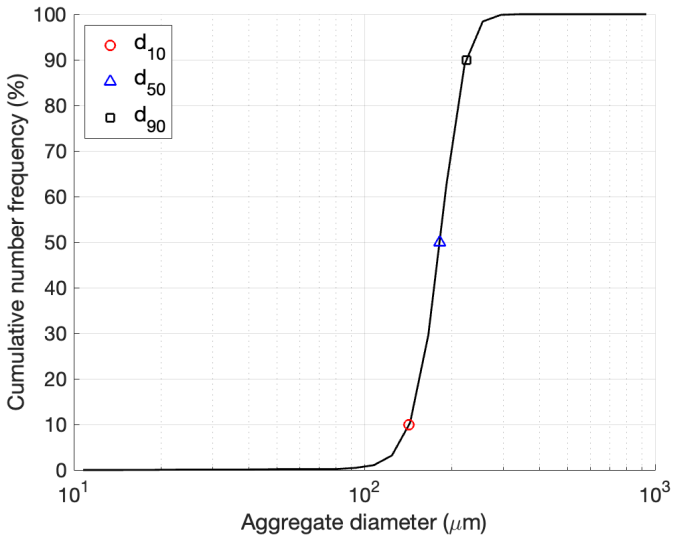

Figure 2.3: Example of how percentiles can be used to characterize an aggregate size distribution.

The floc size distribution can also be characterized by weighted average sizes, which use a single value to represent the entire size distribution. A generic expression for calculating different weighted average diameters is given by [59]

$$D_{pq} = \left(\frac{\sum_{i=1}^{n_{\text{class}}} N_i \cdot d_i^p}{\sum_{i=1}^{n_{\text{class}}} N_i \cdot d_i^q} \right)^{\frac{1}{p-q}} \tag{2.8}$$

where p and q are indices of the weighted average size, n_{class} is the total number of class sizes in the distribution, and N_i and $d_i = 2\,R_{g,i}$ are the number of aggregates and the aggregate diameter from the i-th class size, respectively. In colloidal aggregation and breakage research, the most commonly used average sizes are the surface mean diameter (D_{32}) and the volume mean diameter (D_{43}) [17, 18, 36, 41]. The former provides the average diameter based on the volume-to-surface area ratio, whereas the latter corresponds to the volume weighted mean diameter, which is sensitive to large aggregates in the system [59].

In the current work, the surface mean diameter is used to characterize the average floc size aggregate populations from Cifuentes' [17] breakage experiments, and the percentiles d_{10}, d_{50} and d_{90} are used to quantitatively describe the size range in the floc size distribution. Lastly, Equations 2.6 and 2.7 are used to obtain the aggregate radius of gyration from Cifuentes' experiments [17] and the population balance model, respectively.

2.2 System forces

When aggregates experience shear flows, their fate depends on the balance between hydrodynamic and cohesive forces [10]. Depending on the magnitude of these forces, the flocs can aggregate, break, or restructure [18]. In PBMs, it is necessary to know how to calculate the system forces to predict the aggregation frequency, i.e., the rate of floc collisions that leads to aggregation [60]. Therefore, this section explains how to characterize the cohesive (Section 2.2.1) and hydrodynamic forces (Section 2.2.2) in colloidal fluid-particle systems.

2.2.1 Cohesive forces

The interactions between colloidal particles can be most simply modelled by the Derjaguin-Landau-Verwey-Overbeek (DLVO) theory [8–10], where the net force between two primary particles is equal to the sum of the van der Waals (VDW) and electric double layer (EDL) forces [7]

$$F_{\mathrm{DLVO}} = F_{\mathrm{VDW}} + F_{\mathrm{EDL}} \tag{2.9}$$

Both F_{VDW} and F_{EDL} are normal forces, i.e., they are perpendicular to the particle surface [7]. The VDW force between two identical spherical colloidal particles is always attractive and arises from electrostatic interactions modelled by [61]

$$F_{\mathrm{VDW}} = -\frac{A_h\, r_o}{12\, H^2} \tag{2.10}$$

where r_o is the particle radius, H is the surface-to-surface distance between particles, and A_h is the Hamaker constant, which depends on the chemical composition of the particles and the continuous phase where they are immersed [7].

When colloidal particles are dispersed in a fluid medium, their surfaces are electrically charged due to different mechanisms, e.g., ionization of surface groups and adsorption of charged species from the fluid solution to a neutrally charged solid surface [28]. To electrically neutralize the fluid-particle system, the charged surfaces attract oppositely charged ions (counter-ions) and repel equally charged ions (co-ions). This phenomenon forms a distribution of ions as shown in Figure 2.4, where the Stern layer has counter-ions bound to the charged solid surface, and the diffuse layer has co-ions and counter-ions, which are constantly moving due to the Brownian motion of the continuous phase. This system of charges is known as the electric double-layer (EDL), and it works similarly to a capacitor, where an

electric potential is created by the accumulation of charges surrounding the particle [7, 28, 62].

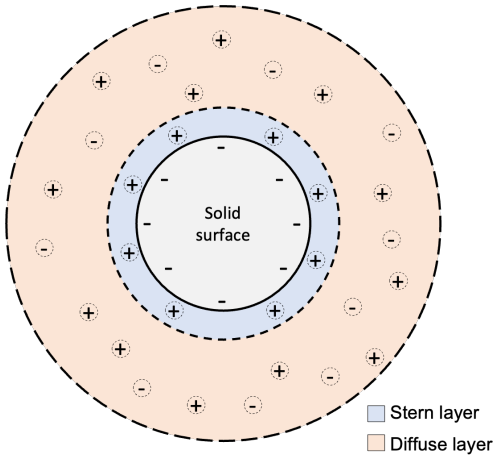

Figure 2.4: Electric double layer (EDL) of a negatively charged spherical particle (Modified from [7]).

If the EDLs of two spherical colloidal particles overlap, the repulsive force will be[7]

$$F_{\mathrm{EDL}} = \frac{64\pi\, R_p\, \epsilon_r\, \epsilon_o}{2} \cdot \left(\frac{k_B\, T}{e_c}\right)^2 \cdot \tanh^2\left(\frac{z\, e_c\, \psi_o}{4k\, T}\right) \cdot \left(\kappa_d\, \mathrm{e}^{-\kappa_d\, H}\right) \tag{2.11}$$

where ϵ_r is the relative permittivity of the carrier fluid, ϵ_o is the vacuum permittivity, k_B is the Boltzmann constant, T is the absolute temperature, e_c is the elementary charge of an electron, z is the valency of the counter-ion, Ψ_o is the surface potential, and κ_d^{-1} is the Debye length, which is written as [28]

$$\kappa_d^{-1} = \left[\frac{e_c^2}{\epsilon_r \epsilon_o kT} \cdot \sum_i z_i^2 c_i A_N\right]^{-1/2} \tag{2.12}$$

where z_i and c_i are the valency and molar concentration of $i-$type ion, respectively, and A_N is the Avogadro number. The Debye length, also known as the double-layer thickness, is an important parameter because it gives the approximate distance between two interacting charged surfaces and therefore their EDL force range [7]. It is important to mention that Equation 2.11 is valid for symmetrical 1:1 electrolyte solutions, e.g., NaCl [7].

Figure 2.5 shows the effect of the separation distance between two spherical particles on their DLVO interaction forces in a 1:1 electrolyte solution with a molar concentration of 2 M. As can be seen, both F_{VDW} and F_{EDL} increase in magnitude with decreasing separation

distance, resulting in a net energy barrier that must be overcome in order to induce aggregation. When this "activation energy" is surpassed, relatively strong aggregates are formed in the primary minimum, where $H \leq 0.1$ nm. If the magnitude of the energy barrier is too high, the colloidal particles will either form weak aggregates in the secondary minimum or remain as a stable dispersion in the system [7].

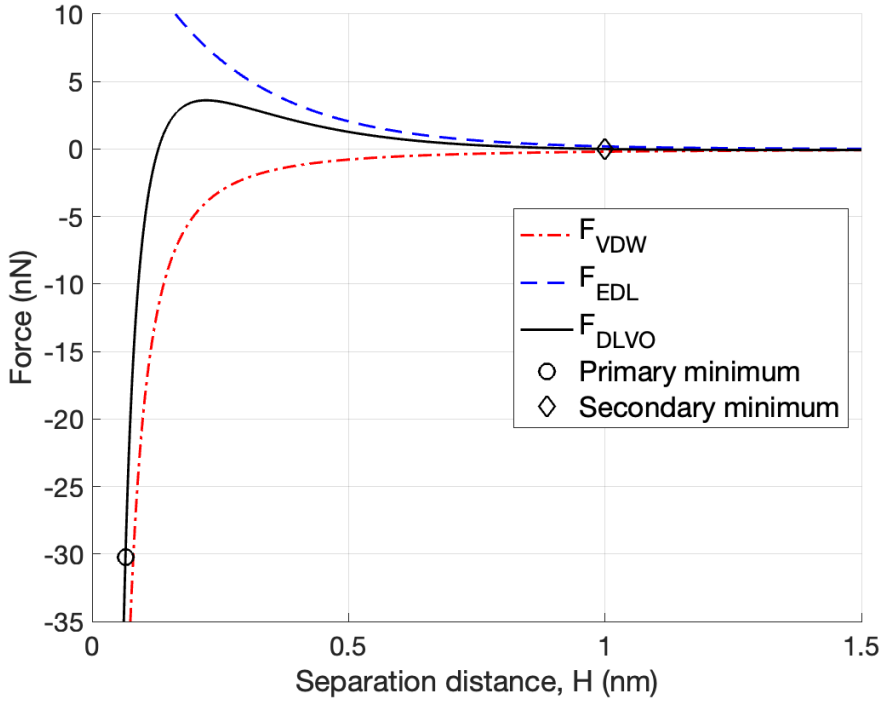

Figure 2.5: Interparticle forces between two spherical colloidal particles ($r_o = 0.735\ \mu m$, $A_h = 1 \cdot 10^{-20}\ J$) in a 2 M 1:1 electrolyte solution (Modified from [8]).

In order to induce the formation of aggregates via VDW forces, one possible approach is to reduce the EDL forces of the system [17, 38]. The EDL forces can be reduced by changing the solution pH, which directly affects the magnitude of the surface potential [7, 62]. Another way to minimize the EDL forces is by reducing the Debye length, which can be achieved by increasing the ionic strength of the system, i.e., the electrolyte concentration [43]. There is a specific electrolyte dosage, known as the critical coagulation concentration (CCC), in which the EDL forces are reduced to a point where the activation energy to form aggregates at the primary minimum is zero [7]. This is illustrated in Figure 2.6, which shows the effect of different 1:1 electrolyte concentrations on the net interaction potential of two spherical colloidal particles. The net potential energy shown in the y-axis was obtained from the relationship $F = -\mathrm{d}V/\mathrm{d}H$ [7]. In this example, CCC = 6.7 M, where $V_{\mathrm{DLVO}}^{\mathrm{max}} = 0\ e\mathrm{V}$. The

CCC can be used in aggregation and breakage experiments where the chemical destabilizers are inorganic salts [9, 38], e.g., in Cifuentes' [17] experiments, which are modelled in the present work via PBM.

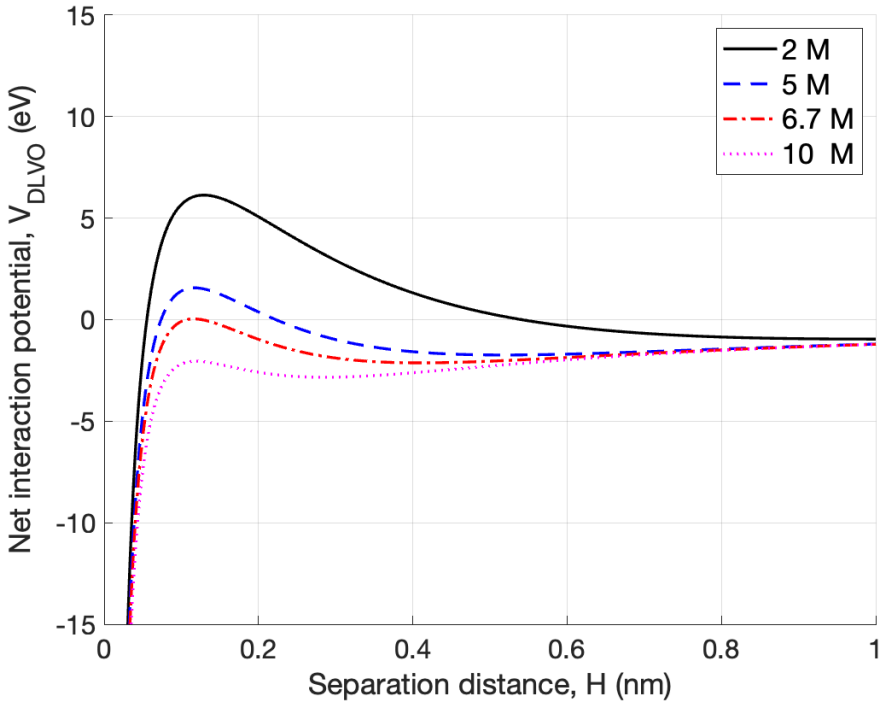

Figure 2.6: Effect of 1:1 electrolyte concentration on the net interaction potential between two spherical particles of $r_o = 0.735\ \mu m$ and $A_h = 1 \cdot 10^{-20}\ J$ (Modified from [7, 8]).

In PBMs, the DLVO forces are essential for the development of aggregation kernels, i.e., equations that predict the rate collisions between flocs that leads to aggregation [60]. Most aggregation kernels are based on an ideal system where only VDW and fluid-particle forces are present [63, 64], which is the case when the CCC is reached [7]. A detailed description of aggregation kernels is given in Section 3.2.1 of Chapter 3.

Besides the normal DLVO forces, colloidal particles can also interact via tangential forces [65], which can affect the aggregate ability to restructure and are important in the modelling of breakage and restructuring of single aggregates in shear flow [8–10]. Since tangential forces were recently discovered [65], they are still not regularly considered in PBMs [20, 22, 55].

2.2.2 Hydrodynamic forces

The fluid motion is characterized by the continuity and momentum conservation equations [66]

$$\frac{\partial \rho_f}{\partial t} + \nabla \cdot (\rho_f \, \vec{\boldsymbol{u}}) = 0 \tag{2.13}$$

$$\frac{\partial (\rho_f \, \vec{\boldsymbol{u}})}{\partial t} + \underbrace{\vec{\boldsymbol{u}} \left[\nabla \cdot (\rho_f \, \vec{\boldsymbol{u}}) \right]}_{\text{Convection}} = \underbrace{\mu \nabla^2 \vec{\boldsymbol{u}}}_{\text{Diffusion}} - \nabla P + \vec{\boldsymbol{F}}_b \tag{2.14}$$

where ρ_f is the fluid density, $\vec{\boldsymbol{u}}$ is the fluid velocity, μ is the dynamic viscosity of the fluid, ∇P is the pressure gradient, and $\boldsymbol{F}_b$ represents the external body forces. The flow diffusion and convection are created from from viscous and inertial forces, respectively [66]. The former originates from the friction between moving fluid layers, and its magnitude increases with the fluid viscosity [67]. The latter is created by the bulk movement of the fluid flow. In colloidal fluid-particle systems, the fluid momentum can be transferred to aggregates via both viscous and inertial forces [40]. The Reynolds number at the aggregate length-scale (Re_{agg}) can be used to compare the magnitude of the hydrodynamic forces experienced by aggregates in different sheared systems [9],

$$\mathrm{Re}_{agg} = \frac{\dot{\gamma} \left(2 \, R_g \right)^2}{\nu} \tag{2.15}$$

where $\dot{\gamma}$ is the shear rate and $\nu = \mu / \rho_f$ is the kinematic viscosity of the fluid. The higher the Reynolds number, the larger will be the hydrodynamic forces in the system [10]. In many CFD studies of single aggregates in shear flows, it is assumed that the inertial forces are negligible at low Reynolds numbers, i.e., $\mathrm{Re}_{agg} \ll 1$ [8, 9, 56, 68, 69]. However, recent CFD investigations that modelled both convection and diffusion showed that inertial forces affect the colloidal aggregation mechanism even at $\mathrm{Re}_{agg} = 0.03$ [2]. This indicates that, to model the real behaviour of aggregates, inertial forces should not be neglected.

Since the shear rate scales with the Reynolds number, this parameter is often used in experiments as a proxy for the magnitude of the hydrodynamic forces [9, 17, 43]. Additionally, the average shear rate of the system is used in PBMs to predict the rate of aggregation and breakage [18, 20, 41]. The mathematical expressions of these two mechanisms and their relationship with the average shear rate are detailed in Chapter 3.

2.3 Population balance modelling of shear-induced colloidal aggregation: a brief introduction

As explained in Chapter 1, the shear-induced aggregation of colloidal particles is a crucial step in many solid-liquid separation processes [6], and the population balance model (PBM) can be used to control the final floc size and structure in aggregating systems [20]. The PBM approach is a statistical method that can predict how the properties of a certain population evolve over time [70], e.g., the size and morphology of flocs during aggregation [18]. The first PBM of colloidal aggregation was proposed by von Smoluchoski [71] in 1917. He modelled the aggregation of colloidal particles as an irreversible mechanism, i.e., the flocs could only change their physical properties by aggregating with other flocs. As experimental research on colloidal aggregates advanced, it was discovered that flocs could also break and restructure in parallel to aggregation depending on the magnitude of the fluid-particle forces in the system [5, 43, 46, 72]. To incorporate these two new mechanisms in the PBM, modifications to the original model from Smoluchoski [71] were proposed over the last decades [18, 20, 36, 73]. Recent PBM investigations have confirmed that the shear-induced aggregation can be modelled by accounting for the aggregation, breakage, and restructuring mechanisms [18, 21, 22, 36, 37].

There are two major PBMs that are currently used to model shear-induced aggregation [20, 74]: the method of classes (MOC) and the quadrature method of moments (QMOM). The advantages and downsides of the MOC and QMOM are presented in the Sections 2.3.1 and 2.3.2, respectively. Then, a direct comparison between these two methods is provided in the Section 2.3.3.

2.3.1 Method of classes (MOC)

The PBM based on the MOC tracks the number density or the average number of flocs per unit volume (N_i) of different floc class sizes (i) over time [74]. As presented in Figure 2.7, the MOC can directly retrieve the aggregate floc size distribution (FSD), where each rectangle represent a floc class size [74].

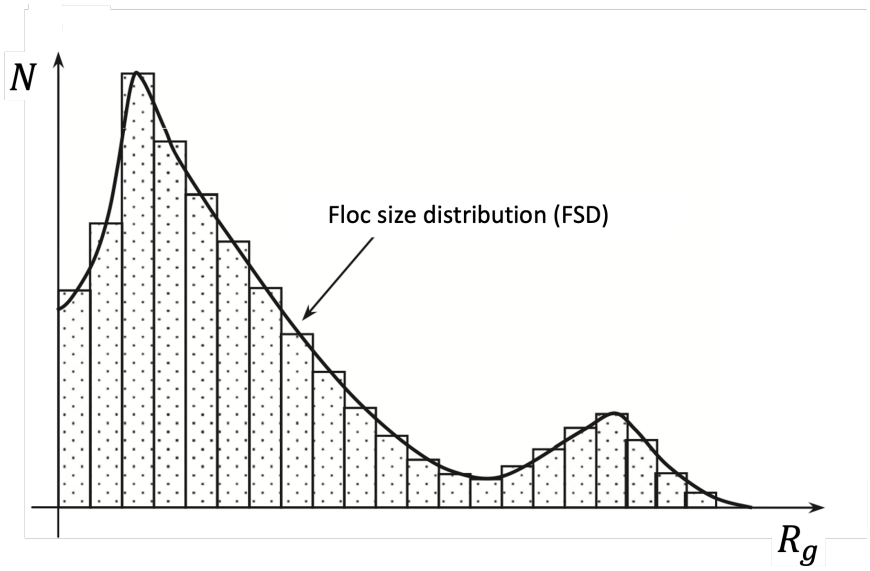

Figure 2.7: Modelling of the aggregate floc size distribution (FSD) based on the method of classes (MOC). The parameters N and R_g are the number density and the radius of gyration, respectively (Modified from Yeoh et al. [74]).

In a closed system, the population balance equation (PBE) from the MOC is given by [20]

$$\frac{dN_i}{dt} = A_i^B - A_i^D + B_i^B - B_i^D \tag{2.16}$$

where A_i^B and A_i^D are the birth and death terms of the aggregation mechanism, respectively, and B_i^B and B_i^D are the birth and death terms of the breakage mechanism, in that order. The birth and death terms denote the formation and disappearance of the i-th floc class size [20], and are illustrated in Figure 2.8. As can be seen, the aggregation and breakage mechanisms can both increase and reduce the number density. In shear-induced aggregation, the fluid momentum contributes to both the aggregation and breakage of flocs [18]. This effect can be accounted for in Equation 2.16 by writing the birth and death terms as a function of the average shear rate experienced by the flocs [20].

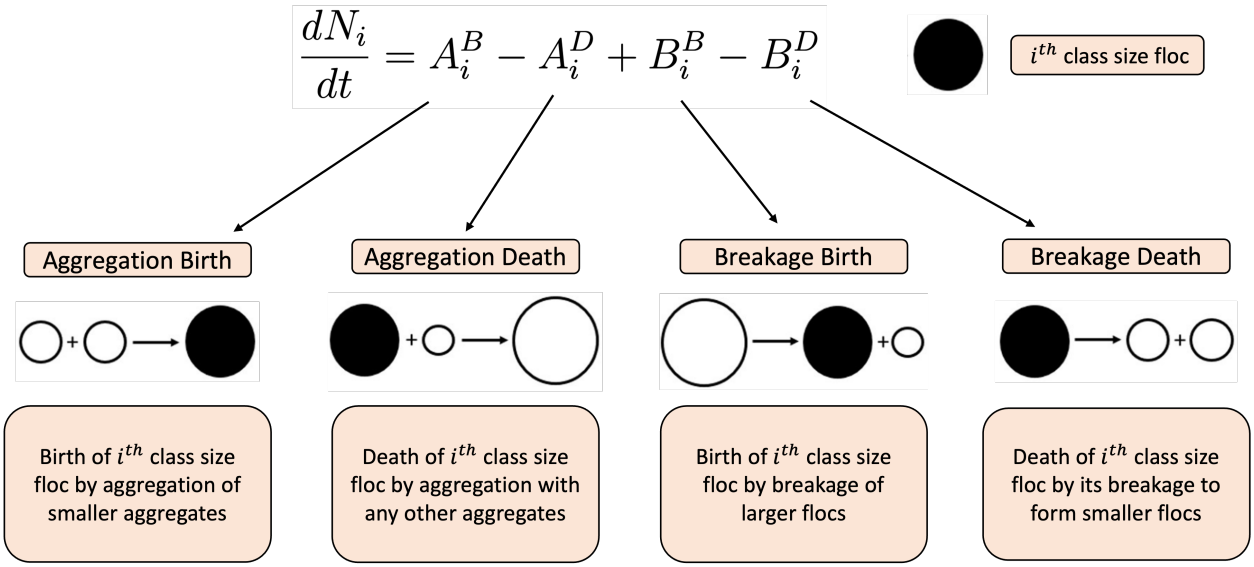

Figure 2.8: Population balance equation (PBE) from the MOC (Modified from Jeldres et al. [20]).

In the MOC, there is one population balance equation (2.16) for each class size. Since populations of aggregates often present a broad range of sizes [17, 48], it would be computationally demanding and therefore impractical to model most aggregation processes via MOC [75]. To overcome this issue, Hounslow et al. [75] and Spicer and Pratsinis [73] developed a lumped form of the MOC for the modelling of colloidal aggregation and breakage mechanisms. In their approach, the number of primary particles of a floc from the i-th class size follows the geometric progression $n_{p,i} = 2^{i-1}$, i.e., the aggregate size is doubled with the linear increase in the class size. As a result, a large range of floc sizes can be covered with a small number of population balance equations, e.g., a MOC with 25 class sizes that models flocs with primary particle size $r_o = 1.0\ \mu m$ and morphology $D_f = 2.4$ covers a size range from $R_{g,1} = 1.0\ \mu m$ (singlets) to $R_{g,25} = 1024\ \mu m$.

In a subsequent study, Selomulya et al. [18] enhanced the PBM previously described [73, 75] by including a restructuring mechanism in the model. They achieved that by adding the differential equation

$$\frac{dD_f}{dt} = t_r^{-1}\left(D_{f,ss} - D_f\right) \tag{2.17}$$

where t_r^{-1} is the aggregate rate of restructuring, and $D_{f,ss}$ is the mass fractal dimension at steady-state, i.e., the fractal dimension that is reached at the end of the shear-induced aggregation experiment. To validate the effectiveness of this new approach, Selomulya et al.

[18] compared their predictions using a PBM with Equation (2.17) with their data obtained from aggregation experiments in turbulent flows. Both are presented in Figure 2.9. As can be seen, Equation (2.17) accurately predicts the structural variation of flocs and their steady state fractal dimension at different shear rates.

The PBM from Selomulya et al. [18] also provided satisfactory predictions of the volume-mean floc size evolution with time (D_{43}). These results confirmed that the evolution of floc size and morphology in shear-induced experiments can be accurately predicted via PBM by accounting for the combined effects of aggregation, breakage, and restructuring mechanisms. Due to the successful predictions of Selomulya et al. [18], their PBM continues to be used in the modelling of shear-induced aggregation experiments [21, 22, 36, 37].

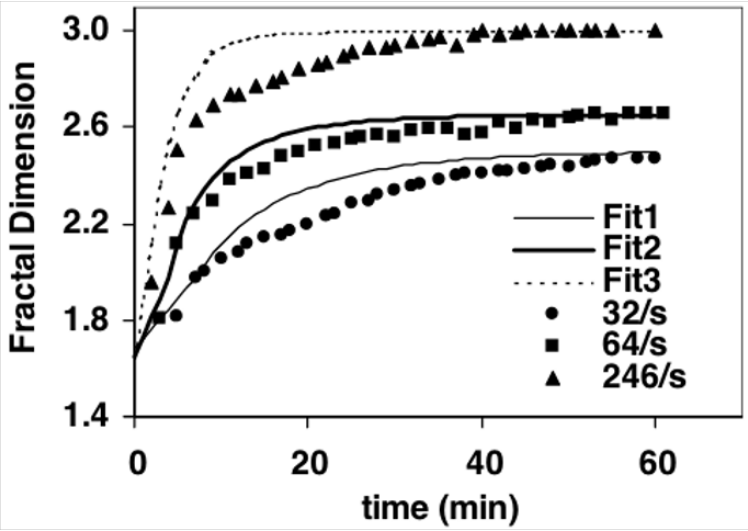

Figure 2.9: Evolution of the floc morphology in shear-induced aggregation from Selomulya et al. [18]. The symbols corresponds to experimental data points, and the continuous and dashed lines are the results from Equation (2.17).

2.3.2 Quadrature method of moments (QMOM)

In colloidal aggregation, the quadrature method of moments (QMOM) tracks the rate of change of the moments of the FSD with time [76]

$$\frac{dm_k}{dt} = A_k^B - A_k^D + B_k^B - B_k^D \tag{2.18}$$

where m_k is the k-th moment of the distribution, A_k^B and A_k^D are the aggregation birth and death terms, respectively, and B_k^B and B_k^D are the breakage birth and death terms,

in that order. Even though the terms on the right-hand-side of Equation (2.18) have the same physical meaning of the terms from the MOC PBE, Equation (2.16), they expand into different mathematical expressions [18, 76]. To solve Equation 2.18 with high accuracy and time efficiency, the QMOM uses the quadrature approximation [76]

$$m_k = \int_0^{+\infty} n' \, L^k \, dL \approx \sum_{i=1}^{n_{\text{nodes}}} w_i \, L_i^k \tag{2.19}$$

where n' is the continuous number density, L_i and w_i are the floc length and weight of node i, and n_{node} is the total number of nodes. Figure 2.10 illustrates how the quadrature approximation works, where four nodes are used to determine the moment of the distribution. As can be seen, with only four data points, the QMOM can retrieve different moments at a given time. The moments can be used to obtain the weighted average size of FSD, i.e., $D_{pq} = m_p/m_q$ [77]. Hence, the QMOM is significantly faster than the MOC to retrieve the average floc size. For instance, only two QMOM PBEs must be solved to determine the evolution of $D_{32} = m_3/m_2$ with time, whereas the MOC uses twenty-five PBEs to first obtain the floc size distribution and then calculates D_{32} via Equation 2.8. It is important to mention that the the FSD can also be retrieved from moments, but this approach is computationally expensive and often not recommended [20]. Additionally, there are no QMOM investigations in which the floc morphology is tracked over time, and most studies assume a fixed value of D_f to characterize the aggregate throughout the entire simulation [19, 41, 77, 78].

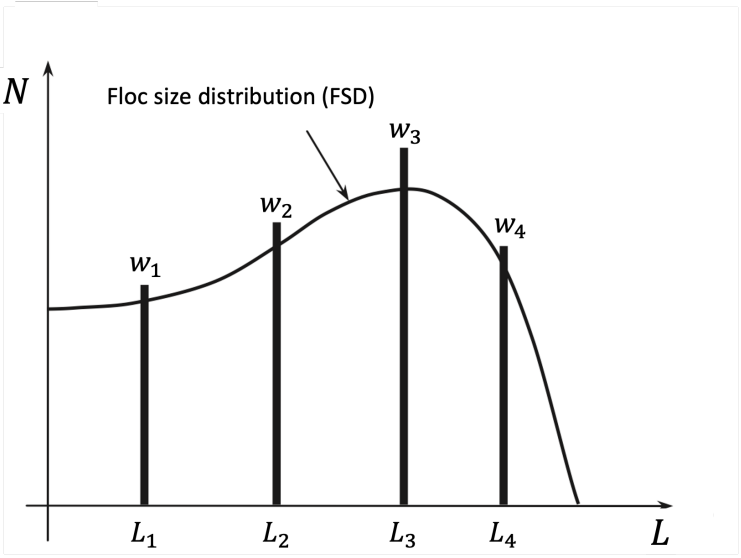

Figure 2.10: Illustration of the quadrature method of moments (QMOM), where N is the number density, L_i is floc length, and w_i is the weight (Modified from Yeoh et al. [74]).

Due to the high computational efficiency of the QMOM, this approach can be coupled with large-scale CFD simulations of shear-induced aggregation, where the weighted average floc size is the physical parameter of interest from the population of aggregates [19, 41]. For example, Wang et al. [41] used QMOM-CFD to model shear-induced aggregation in laminar vortex flows. This type of flow induces periodic oscillations in the shear rate, and Wang et al. [41] used it to test the effectiveness of using the average shear rate (G) to characterize the rate of aggregation and breakage in the system. They compared QMOM results using the G and the local shear rate ($\dot{\gamma}$). They observed that the both G and $\dot{\gamma}$ produced approximately the same PBM results. Similar observations were also found for aggregation in turbulent flows by Marchisio et al. [19]. They concluded that the average shear rate can be used in PBMs instead of the local shear rate as long as the aggregation and breakage timescales are shorter than the macromixing timescale, i.e., at the mixing vessel length-scale.

2.3.3 Comparison between MOC and QMOM

In summary, the MOC and QMOM are the most commonly used methods to track the physical properties of colloidal aggregates in shear-induced aggregation [20, 74]. The QMOM is computationally faster than the MOC to retrieve the moments and weighted average sizes of populations of aggregates, and is often preferentially coupled with CFD [79]. However,

the MOC can directly calculate the FSD and it can also track the change in aggregate morphology with time [18]. Since the MOC provides a more detailed description of the physical properties of aggregates in sheared systems, this method will be used in the current study to investigate the floc breakage and restructuring mechanisms.

2.4 Aggregate breakage and restructuring in shear flow

Due to the detrimental effect of floc breakup on the efficiency of solid-liquid separation systems, there has been an increased interest in measuring the aggregate strength, i.e., its resistance to breakage [14, 53], and in more fully understanding the floc breakage and restructuring mechanisms at the aggregate length-scale [9, 10]. This section summarizes the relevant studies in this research area and their potential for improving PBMs. Section 2.4.1 describes how the floc strength can be indirectly measured and used in PBMs to describe the breakage mechanism. Section 2.4.2 explains how the breakage and restructuring occurs at the aggregate length-scale in simple shear flows, and how the latest findings in this area can be used to improve current PBMs.

2.4.1 Strength

As explained in Chapter 1 and Section 2.2, the restructuring and breakage of flocs depend on the balance between the cohesive and hydrodynamic forces acting on the aggregate [10]. When the hydrodynamic forces (F_h) are orders of magnitude greater than the cohesive forces (F_c), the breakage mechanism is favoured, which increases the floc breakage frequency. When the system forces have the same order of magnitude, i.e., $F_h \approx F_c$, the restructuring mechanism is favoured, where flocs can form compact structures that are less prone to break [10]. The hydrodynamic force experienced by an aggregate can be approximated by the viscous force acting on a sphere with a radius equivalent to the floc radius of gyration [80]

$$F_{\text{viscous}} = \frac{5}{2}\pi\mu R_g^2\dot{\gamma} \tag{2.20}$$

As can be seen, F_{viscous} scales with the shear rate. Thus, the shear rate can be used as a proxy for the hydrodynamic forces. The steady-state floc size, R_g^{ss}, is typically assumed to scale with the shear rate via the power-law relationship [14, 53]

$$R_g^{ss} \propto \dot{\gamma}^{-p} \tag{2.21}$$

where p is a scaling exponent that provides an indirect measurement of the aggregate strength. Experiments [9, 38, 43, 81–85] and CFD investigations of single aggregates in shear flow [9, 40, 86–88] showed that $p = [0.35\ 0.60]$. Smaller values of p represent strong aggregates because of their greater resistance to breakage, i.e., they have a smaller decrease in size with the increase in shear rate. The parameter p also depends on the chemical nature and dosage of chemical destabilizers [43, 84] and on the initial floc morphology [9, 88], but it is independent of the primary particle size [9]. Equation (2.21) is used in PBMs to develop breakage kernels, which predict the breakup frequency of flocs with different sizes and morphologies [18]. The breakage kernel is crucial for the development of the breakage birth and death terms of PBEs [18], and is explained in detail in Section 3.2.2 of Chapter 3.

2.4.2 Shear-induced breakage and restructuring at aggregate length-scale

Simple shear flows are a combination of pure rotational and straining flows, which results in the rotation of immersed solid bodies [40]. During rotation, the solid object experiences periodic viscous stresses that consist of compression and elongation cycles. In the case of a perfect sphere, the maximum values of compression and elongation occur at -45^o and 45^o from the x-axis. The axes of maximum hydrodynamic stresses are also known as principal axes.

Blaser [39] developed an experimental approach to observe the effect of simple shear flows on the breakage and restructuring mechanisms at aggregate scale. He tracked the evolution of single aggregates in shear flow via image analysis in a controlled shear device. He observed that the aggregate rotated similarly to a solid sphere in simple shear flow, but the maximum compression and elongation stresses occurred along the flow streamlines ($\theta = 0^o$) instead of the principal axes of stress. Blaser [39] hypothesized that this discrepancy was due to aggregate rotation, which caused a retardation effect of the hydrodynamic stresses experienced by it. The experimental observations from Blaser [39] were later confirmed via numerical simulations by Horii et al. [16], who studied the evolution of non-fractal aggregates in simple shear flows. They specifically investigated flocs with a cohesive strength of similar magnitude to the hydrodynamic stresses at aggregate scale, thereby allowing the aggregates to endure several rotation cycles before breakage. They observed that the retardation effect in compression and elongation cycles facilitated the restructuring of flocs.

Although the work of Blaser [39] and Horii et al. [16] is crucial for understanding the breakage and restructuring mechanisms at aggregate scale, almost no information regarding the types of fragments formed from floc breakage could be obtained from these studies. To fill this research gap, Vanni and Gastaldi [69] developed a CFD method to monitor the evolution of internal stresses across the primary particles of aggregates. They performed simulations with low-density flocs ($D_f = \{1.7, 2.3\}$) in simple shear flows at low Reynolds number, i.e., $\mathrm{Re}_{agg} \approx 0$. From the simulation results, they observed that the maximum hydrodynamic stresses are experienced by the particles on the periphery of the floc. These stresses then distribute along primary particle filaments and concentrate close to the aggregate center of mass. This was the region where the floc breakup occurred, which was caused by the failure of a single inter-particle bond. Consequently, fragments of similar sizes were obtained from the breakage of low-density flocs. In a subsequent study, Vanni [68] investigated the propagation of stresses in high-density fractal aggregates at low Reynolds numbers. He discovered that the hydrodynamic stresses applied to dense flocs redistribute locally, keeping the majority of the stressed bonds at the aggregate periphery. This behaviour induced the breakage of flocs via erosion, where two fragments of dissimilar sizes are created: one with a small number of primary particles and the other with practically the same size of the parent floc. Vanni [68] also observed that the redistribution of stresses in high-density aggregates can cause a series of bond failures from the floc periphery towards its center of mass. This phenomenon behaves like a crack propagation mechanism, leading to the formation of fragments with similar sizes.

The work from Vanni [68, 69] provided a detailed analysis of the effect of aggregate morphology on the different floc breakage mechanisms in simple shear flow. However, in these studies, flow inertia was assumed to be negligible. Recent CFD simulations revealed that flow inertia has an important effect on the aggregation mechanism for Reynolds numbers as low as 0.03 [2]. Additionally, Saxena [40] investigated the breakage and restructuring of aggregates in simple shear flow while considering both viscous and inertial forces in the system. They used a CFD method to track the evolution of ten different aggregates with the same initial size ($R_g/r_o \approx 5.3$) and morphology ($D_f \approx 2.3$). His results indicated that the floc breakage always leads to the formation of two fragments, and that the fragment size is not affected by the Reynolds number. This means that similar aggregates can break into fragments of varying sizes at the same flow conditions, as illustrated in Figure 2.11. This

important finding goes against the simplifying assumption from most PBM studies, i.e., that floc breakage is always symmetric, and can only form fragments of equal sizes [18, 20, 36, 41]. Hence, there is a potential to improve current PBMs by developing new functions to determine the fragment size after floc breakage.

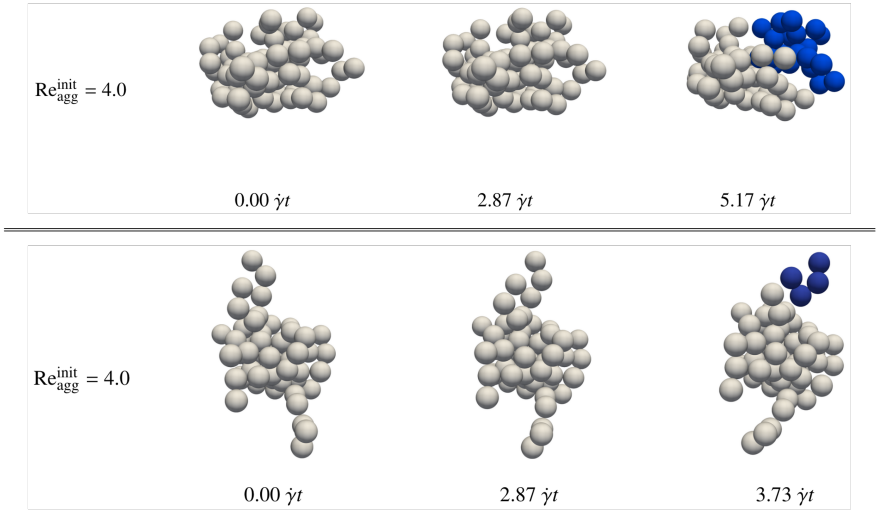

Figure 2.11: Evolution of two similar aggregates at the same Reynolds number. The particles highlighted in blue correspond to the fragment formed after breakage (modified from Saxena [40]).

2.5 Summary

The following points summarize the key information provided in this chapter:

- The evolution of colloidal aggregates in shear flows is controlled by the interplay between cohesive and hydrodynamic forces [10];
- Since aggregates have complex and fragile structures, they must be studied via in situ, non-intrusive techniques [17, 48];
- Shear-induced aggregation is dictated by the kinetic competition between aggregation, breakage, and restructuring mechanisms, which can be accurately modelled via PBM [18];
- When the aggregation and breakage time-scales are longer than the mixing time-scale, the average shear rate can correctly characterize the rate of aggregation and breakage in PBMs [19, 41];

- The floc breakage can occur via erosion and symmetric fragmentation mechanisms [68]. At finite Reynolds numbers, Saxena [40] observed that there is no strong prevalence of one type of breakage mechanism over another as both of them had similar occurrence frequencies. This indicates that fragments with varying sizes can be formed from floc breakage and they seem to have similar probabilities of occurring.

2.5.1 Identified Knowledge gaps

From this literature review, the following knowledge gaps can be identified:

- To the author's knowledge, the current PBM investigations in colloidal science are primarily focused on describing shear-induced aggregation [20]. Therefore, there is a need for population balance studies focused on modelling shear-induced breakage experiments;
- Most population balance studies assume that aggregate breakage is always symmetric, i.e., it can only form two fragments with equal sizes [18, 20, 36, 41]. However, recent CFD investigations conducted at finite Reynolds numbers showed that both symmetric and erosion breakage mechanisms have a similar chance of occurring [40]. Since these observations were made for only a small sample of aggregates, it is necessary to investigate the breakage mechanism that can best model the behaviour of populations of aggregates in aggregation and breakage experiments.

2.5.2 Proposed scope of the current study

Based on the information provided above, the major aim of this research project is to investigate the breakage and the restructuring of colloidal aggregates in simple shear flows. To achieve this goal, the following objectives were pursued:

- To model the breakage experiments of Cifuentes [17] via the MOC PBM;
- To investigate which type of breakage mechanism can best predict the evolution of the size and morphology of populations of aggregates in breakage experiments.

Chapter 3

Numerical methods

As explained in Section 2.5, the major objective of the current project is to investigate the restructuring and breakage of colloidal aggregates in laminar shear flow. To achieve this goal, a population balance model (PBM) is used to predict the evolution of the average floc size, the floc size distribution (FSD), and the global morphology of populations of aggregates from Cifuentes' [17] breakage experiments. A summary of the materials and experimental method from Cifuentes [17] is provided in Section 3.1. A detailed description of the equations that constitute the PBM is then provided: Section 3.2 delineates the population balance equation (PBE) and its the crucial parameters for the modelling of aggregation and breakage mechanisms; Section 3.3 describes the mass fractal dimension (D_f) ordinary differential equation (ODE), which can be used to model the restructuring of populations of aggregates; and Section 3.4 explains how the PBE and the D_f ODE can be numerically solved together to account for the aggregation, breakage, and restructuring mechanisms in laminar shear flow. Lastly, Section 3.5 provides a summary of the hypotheses and case studies that are investigated by in this work.

3.1 Experiments

Recently, Cifuentes [17] investigated the aggregation, breakage and restructuring of colloidal aggregates in laminar flow in a Taylor-Couette cell consisting of a rotating inner cylinder and a stationary outer cylinder. This experimental apparatus was chosen because the spatial average shear rate is approximately constant for laminar flow and can be easily determined by [89]

$$G = \frac{2 \cdot \omega_{in} \cdot R_{in} \cdot R_{out}}{R_{out}^2 - R_{in}^2} \tag{3.1}$$

where w_{in} and $R_{in} = 35.75$ mm are the angular velocity and radius of the inner cylinder, respectively, and $R_{out} = 38.25$ mm is the outer cylinder radius. Hence, the gap distance between the two concentric cylinders is $d_{gap} = 1.5$ mm, resulting in a critical Taylor number of $\mathrm{Ta}_{cri} = 42.07$ based on [90]

$$\mathrm{Ta}_{cri} = \frac{\pi^4\left(1 + \frac{d_{gap}}{2R_{in}}\right)}{5.71 \cdot 10^{-2}\left[1 - 0.652\left(\frac{d_{gap}}{R_{in}}\right)\right] + 5.6 \cdot 10^{-4}\left[1 - 0.652\left(\frac{d_{gap}}{R_{in}}\right)\right]^{-1}} \tag{3.2}$$

To ensure laminar flow in this apparatus, $\mathrm{Ta} < \mathrm{Ta}_{cri}$, which requires $G \leq 89.48\ \mathrm{s}^{-1}$ according to [89]

$$\mathrm{Ta} = \frac{\omega_{in}}{\nu}\sqrt{R_{in}\left(R_{out} - R_{in}\right)^3} \tag{3.3}$$

where ν is the kinematic viscosity. The aggregate size and structure were monitored via 2D image analysis (AOS PROMON 501 CMOS high-speed camera) by measuring the pixel R_g (see Equation (2.6)) and the global D_f (see Equation (2.2)), respectively. As discussed in Section 2.1.1, this is an in situ and non-intrusive measuring technique, and is therefore suitable for studying colloidal aggregates.

As can be seen in Figure 3.1, each experiment consisted of two major stages, 1) aggregation and 2) breakage. In the aggregation stage, a colloidal dispersion of latex particles ($d_o = 2\ \mu$m, $\rho_s = 1,055\ \mathrm{kg/m^3}$) was initially destabilized by adding it to a sodium chloride solution of 1.4 M (pH = 7.0), which was made with de-ionized water. The Hamaker constant for latex particles in water has a representative value of $A_h = 1.37 \cdot 10^{-20}$J, which was acquired from Prieve and Russell [91]. This electrolyte concentration was carefully chosen to prevent particle settling by matching the fluid solution and solid density, and to screen the electric double-layer forces from the system by staying above the critical coagulation concentration. To isolate the effect of shear on aggregation and breakage, the solids volume concentration was $C_v = 1 \cdot 10^{-4}$ for all experiments, which also minimized the overlapping of particles during image acquisition. Additionally, since the experiments were carried out at 20^o C and in very dilute conditions, the dynamic viscosity of the NaCl solution was assumed to be the same as water viscosity at this temperature, i.e., $\mu = 1 \cdot 10^{-3}\ \mathrm{Pa \cdot s}$.

After destabilizing the colloidal dispersion, the inner cylinder was set to rotate at its maximum speed of 442.5 RPM for 5 min to break any aggregate that was previously formed from pouring the colloidal particle suspension into the device. Then, the shear rate was reduced

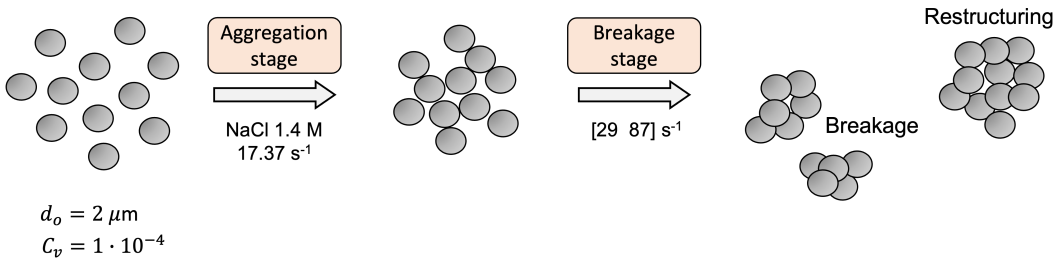

Figure 3.1: Summary of experimental procedure from Cifuentes [17]

to 17.6 s^{-1} (30 RPM) to initiate shear-induced aggregation. The end of the aggregation stage was assumed to occur when the flocs reached a steady-state size distribution. This was determined by comparing the size distributions after 2.5 hrs and 3 hrs of shearing. To guarantee that the suspension of aggregates were correctly characterized in the experiments, samples of around 3000 to 18000 flocs were analyzed at each time measurement.

Once the aggregation stage was completed, a step increase in the shear rate was made. The values of G ranged from 28.95 s^{-1} to 86.86 s^{-1}. This resulted in the restructuring and breakage of aggregates, and smaller steady-state size distributions were produced. As the time required to reach steady-state after the breakage stage depended on the shear rate magnitude, several measurements at regular intervals were done throughout the breakage experiment.

Since this project aims to investigate the breakage and restructuring of aggregates under laminar shear flow conditions, only the breakage stage of each experiment is modelled via PBM. Hence, the steady-state floc size distribution and morphology from the aggregation stage was considered to be the initial condition of the system for the PBM, i.e., at $t = 0$ min. A total of 15 experiments were modelled in the present work, three for each shear rate. The hydrodynamic forces acting on the population of aggregates for each experiment can be characterized by the Reynolds number based on the surface mean floc size, i.e.,

$$\mathrm{Re}_{D_{32}} = \frac{G\left(D_{32}\right)^2}{\nu} \tag{3.4}$$

Table 3.1 summarizes the different flow conditions of the experiments modelled in the present work, where $\mathrm{Re}^o_{D_{32}}$ is the floc population Reynolds number at $t = 0$ min. The initial average surface mean diameter ($\overline{D^o_{32}}$) was used to calculate $\mathrm{Re}^o_{D_{32}}$, where

$$\overline{D^o_{32}} = \frac{\sum_{k=1}^{15} D_{32}}{15} = 204\ \mu\mathrm{m} \tag{3.5}$$

Since $\mathrm{Re}^{o}_{D_{32}} > 1$ for all experiments, both flow inertia and viscous forces influence the breakage and restructuring phenomena, as explained by Saxena [40]. It is important to mention that this work used a simplified version of Cifuentes' experiment IDs, and Appendix A has a detailed description of his original tagging system. For more details on the imaging analysis technique and experimental protocols, please refer to Cifuentes [17].

Table 3.1: Flow field parameters

w_{in} (rpm)	G (s^{-1})	$\mathrm{Re}^{o}_{D_{32}}$	Exp. ID
50	28.95	1.27	1, 2, 3
60	34.75	1.53	4, 5, 6
100	57.91	2.54	7, 8, 9
130	7528	3.31	10, 11, 12
150	86.86	3.81	13, 14, 15

3.2 Population Balance Equation

In colloidal systems, the population balance equation (PBE) tracks the kinetic evolution of the aggregate physical properties over time. In this current work, the lumped discrete population balance from Spicer and Pratsinis [73] and Hounslow et al. [75] is used due to its low computational cost, ease of comparision with experimental data, and ability to retrieve the floc size distribution at each time step [18, 36]. For closed systems [73, 75],

$$\frac{dN_i}{dt} = A_i^B - A_i^D + B_i^B - B_i^D \tag{3.6}$$

where N_i is the number density or the average number of flocs per unit volume containing $n_{p,i} = 2^{i-1}$ primary particles. Thus, N_1 corresponds to the number density of primary particles or singlets in the system. Since this PBE follows a geometric progression of powers of two, the total number of primary particles within an aggregate is always doubled with the linear increase in the class size, i.e., $n_{p,i+1} = 2\, n_{p,i}$. This allows this PBE to track a wide range of aggregate sizes with a relatively small number of class sizes. Accordingly, in the

present work, 25 class sizes were tracked over time. Equation (3.6) corresponds to the net rate of change in the number density with time, accounting for the birth and death of flocs due to aggregation (A_i^B, A_i^D) and breakage (B_i^B, B_i^D). The equations for these four terms as well as their meaning are listed below:

- A_i^B: birth (or formation) of i-th class flocs due to the aggregation of flocs from smaller class sizes, i.e.

$$A_i^B = \sum_{j=1}^{i-2} 2^{j-i+1} \Lambda_{i-1,j} N_{i-1} N_j + \frac{1}{2} \Lambda_{i-1,i-1} N_{i-1}^2 \tag{3.7}$$

  where $\Lambda_{i,j}$ is the aggregation kernel.

- A_i^D: death (or disappearance) of i-th class flocs due to their aggregation with other flocs to form aggregates of larger size, where

$$A_i^D = -N_i \sum_{j=1}^{i-1} 2^{j-i} \Lambda_{i,j} N_j - N_i \sum_{j=i}^{n_c} \Lambda_{i,j} N_j \tag{3.8}$$

  where n_c is the total number of class sizes that are tracked by the PBE.

- B_i^B: birth of i-th class flocs due to the breakage of larger aggregates, i.e.,

$$B_i^B = \sum_{j=i}^{n_c} \Gamma_{i,j} S_j N_j \tag{3.9}$$

  where $\Gamma_{i,j}$ is the breakage distribution function and S_i is the breakage kernel.

- B_i^D: death of i-th class aggregates due their breakage to form smaller flocs, i.e.,

$$B_i^D = -S_i N_i \tag{3.10}$$

There are three critical parameters within Equations (3.7) to (3.10) that ultimately determine the aggregation and breakage kinetics, which are essential for the correct modelling of sheared colloidal systems. They are the aggregation kernel ($\Lambda_{i,j}$), the breakage kernel (S_i), and the the breakage distribution function ($\Gamma_{i,j}$) [20]. The meaning and expressions for each of these parameters are provided in the following subsections.

3.2.1 Aggregation kernel

The aggregation kernel, $\Lambda_{i,j}$, corresponds to the volumetric flowrate of i-th and j-th class flocs through the collision cross-section $R_{g,i} + R_{g,j}$ [71]. When multiplied by $N_i \cdot N_j$, it gives the aggregation frequency, i.e., the rate of collisions that results in aggregation [74]. This

parameter is determined by the sum of the perikinetic (P), orthokinetic (O), and differential settling (DS) collision mechanisms [20],

$$\Lambda_{i,j} = \Lambda_{i,j}^{\mathrm{P}} + \Lambda_{i,j}^{\mathrm{O}} + \Lambda_{i,j}^{\mathrm{DS}} \tag{3.11}$$

In Cifuentes' experiments [17], there is no differential settling because particles were neutrally buoyant in the sodium chloride solution. To determine the relative influence of the orthokinetic and perikinetic collision mechanisms, the Péclet number is used, which corresponds to the dimensionless ratio between the viscous and the Brownian forces of the system [92]:

$$\mathrm{Pe} = \frac{6\pi\mu G r_o^3}{k_b T} \tag{3.12}$$

where r_o is the primary particle radius, k_B is the Boltzmann constant, and T is the absolute temperature. In Cifuentes' experiments [17], the Péclet number at the lowest shear rate ($G = 17.6\mathrm{s}^{-1}$) is $\mathrm{Pe} \approx 1 \times 10^5$, which indicates that the perikinetic collision mechanism is also negligible. Hence, the collision frequency is driven only by the orthokinetic (shear-induced) mechanism, i.e.,

$$\Lambda_{i,j} = \Lambda_{i,j}^{\mathrm{O}} = \beta_{i,j} \cdot \alpha_{i,j} \tag{3.13}$$

where $\beta_{i,j}$ corresponds to the rectilinear collision kernel from Smoluchowski [71], and $\alpha_{i,j}$ is the collision efficiency, which accounts for the effect of hydrodynamic and cohesive interactions on floc trajectories. [60], as shown in Figure 3.2.

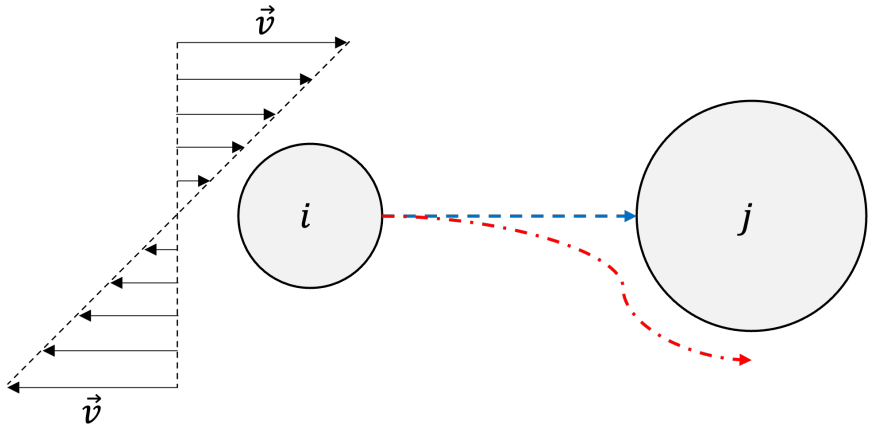

Figure 3.2: Illustration of floc trajectory in simple shear flow. The dashed arrow represents the rectilinear trajectory assumed in Smoluchowski's collision kernel [71], and the dashed-point arrow corresponds to the actual floc trajectory, which is accounted for in shear-induced collisions by including $\alpha_{i,j}$ in Equation (3.13).

The rectilinear collision kernel is given by the well-established, analytical expression [71]

$$\beta_{ij} = \frac{4}{3} G \left(R_{g,i} + R_{g,j} \right)^3 \tag{3.14}$$

where $R_{g,i} = r_o \left(n_{p,i} \right)^{1/D_f}$ is the radius of gyration of the i-th aggregate class size [18]. Since the total number of primary particles of class i flocs is $n_{p,i} = 2^{i-1}$, the radius of gyration simplifies to

$$R_{g,i} = r_o 2^{(i-1)/D_f} \tag{3.15}$$

By substituting Equation (3.15) into Equation (3.14), the influence of the aggregate fractal nature is accounted for in the collision frequency, in which porous flocs ($D_f \approx 1.8$) have a higher chance of colliding when compared to compact flocs ($D_f \approx 2.4$). Concerning the collision efficiency equation, since different models have been proposed over the last decades, a critical review of the literature on this topic is provided below.

Collision efficiency

In unstable colloidal dispersions, as flocs approach one another, they deviate from rectilinear trajectories due to short-range hydrodynamic and colloidal interactions [60]. At the particle scale, lubrication and Van der Waals forces occur. The former tends to decrease the collision frequency between aggregates, whereas the latter enhances it [93]. At the aggregate scale, the flow disturbance caused by the presence of flocs in the fluid also decreases the frequency of floc collisions [2, 55]. To include these effects in the shear-induced collision kernel (3.13), the collision efficiency is used, which is defined as the ratio between the effective aggregation frequency and the rectilinear collision frequency [60].

Collision efficiency models are often obtained by investigating the relative trajectories of solid spheres [63, 64, 94] and permeable spheres in simple shear flow [60, 95]. In the doublet formation stage, homocoagulation [94] and heterocoagulation [63, 64] studies showed that the collision efficiency is a function of the dimensionless ratio between hydrodynamic and cohesive forces, also known as the flow number ($Fl_{i,j}^{\mathrm{sp}}$) [94]:

$$\alpha_{i,j}^{sp} \approx \left(Fl_{i,j}^{\mathrm{sp}} \right)^{-0.18} \quad ; \quad Fl_{i,j}^{\mathrm{sp}} = \frac{6\pi\mu R_{g,i}^3 \left(1 + \lambda_{i,j} \right)}{8A} \tag{3.16}$$

where $\lambda_{i,j} = R_{g,j}/R_{g,i}$ is the size ratio for $j < i$. Equation (3.16) reveals that the collision efficiency of equally sized flocs is higher than that for flocs with different sizes. Kusters et al.

[60] extended this model to determine the collision efficiency of impermeable porous flocs, $\alpha^{i}_{i,j}$, by modifying $Fl^{\mathrm{sp}}_{i,j}$,

$$Fl^{\mathrm{i}}_{i,j} = Fl^{\mathrm{sp}}_{i,j} \cdot \left[\frac{2\lambda_{i,j} R_{g,i}}{r_o\big(1+\lambda_{i,j}\big)} \right] \tag{3.17}$$

The term in the square brackets of Equation (3.17) is the ratio between the attractive forces of solid particles and porous flocs, respectively, which accounts for the fractal nature of aggregates in the collision efficiency. Kusters et al. [60] also proposed a new collision efficiency, $\alpha^{\mathrm{p}}_{i,j}$, that considers the influence of flow penetration on aggregate trajectories by modelling flocs as spheres containing a permeable shell and an impermeable core. It assumes that floc trajectories follow the streamlines inside and around a uniformly porous sphere, which was previously studied by Adler [95]. This shell-core model defines the collision efficiency as a function of only two parameters: the size ratio, $\lambda_{i,j}$, and the dimensionless size of the largest colliding floc:

$$\xi_i = \frac{R_{g,i}}{\sqrt{\kappa_i}} \tag{3.18}$$

where $R_{g,i}$ is the shell radius, and κ_i is the floc permeability. This dimensionless floc size is also referred to as Debye's shielding ratio. As can be seen in Figure 3.3, the collision efficiency of permeable flocs tends to exponentially decrease with ξ_i, and this decay is more pronounced for collisions between flocs of different size, i.e., lower values of $\lambda_{i,j}$. According to Kusters et al. [60], floc collisions for $\lambda_{i,j} \geq 0.2$ are approximately the same as $\lambda_{i,j} = 1$. Additionally, when $\lambda_{i,j} \in \,]0.1\ \ 0.2[$, the collision efficiency can be obtained via linear interpolation between the two curves from Figure 3.3.

To calculate ξ_i, it is first necessary to determine the floc permeability, which is a function of the floc density (ϕ_i), a shielding coefficient that accounts for aggregate morphology (C_s), and the primary particle radius (r_o),

$$\kappa_i = \frac{3 - 4.5 \cdot \phi_i^{1/3} + 4.5 \cdot \phi_i^{5/3} - 3 \cdot \phi_i^{2}}{9\phi_i\big(3 + 2\phi_i^{5/3}\big)C_s} \cdot (2r_o^2) \tag{3.19}$$

The shielding coefficient is 0.724 for doublet collisions [96] and is approximately 0.50 for collisions between larger aggregates [60]. The floc density is defined as

$$\phi_i = \phi_o \left(\frac{R_{g,i}}{r_o} \right)^{D_f - 3} \tag{3.20}$$

where $\phi_o = 1$ is the packing density ($1 -$ minimum porosity). Since the shell-core model does not consider the effect of Van der Waals forces, Kusters et al. [60] suggests that the final

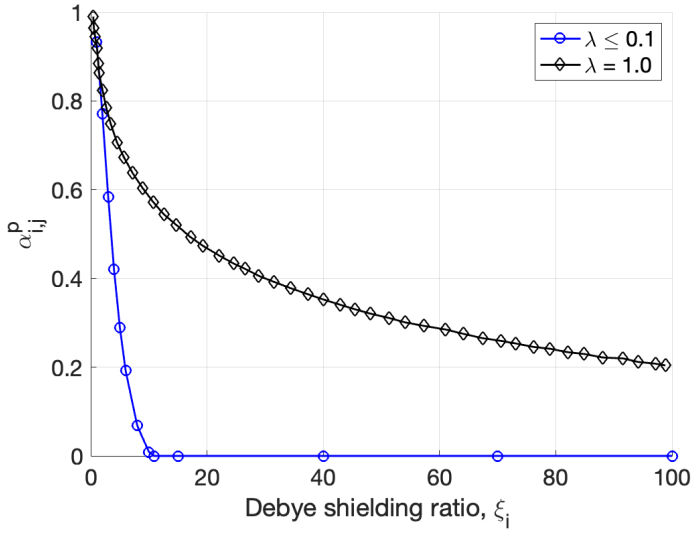

Figure 3.3: Shell-core model collision efficiency, $\alpha^{\mathrm{p}}_{i,j}$, as a function of dimensionless floc size, ξ_i, for two size ratios, $\lambda_{i,j}$ (modified from [60]).

collision efficiency should be the largest value between the collision efficiency for impermeable ($\alpha^{\mathrm{i}}_{i,j}$) and permeable flocs ($\alpha^{\mathrm{p}}_{i,j}$), i.e.,

$$\alpha_{i,j} = \begin{cases} \alpha^{\mathrm{sp}}_{i,j} \approx \left(Fl_{\mathrm{sp}}\right)^{-0.18}; & \text{if } (i \text{ and } j) = 1 \\ \alpha^{\mathrm{i}}_{i,j} \approx \left(Fl_{\mathrm{sp}}\right)^{-0.18}; & \text{if } \left(i \text{ or } j\right) > 1, \text{ and } \alpha^{if}_{i,j} > \alpha^{pf}_{i,j} \\ \alpha^{\mathrm{p}}_{i,j} = f(\lambda, \xi_i) \qquad ; & \text{if } \left(i \text{ or } j\right) > 1, \text{ and } \alpha^{f}_{i,j} \leq \alpha^{pf}_{i,j} \end{cases} \tag{3.21}$$

Although Kusters et al. [60] developed one of the most comprehensive collision efficiency approaches from a physical perspective, its implementation is complex and computationally demanding because it requires several equations and conditional operations. Selomulya et al. [18] simplified the Kusters et al. [60] model by developing an analogous empirical equation,

$$\alpha_{i,j} = \alpha_{\max} \cdot \frac{\exp\left[-x \left(1 - \frac{\max(i,j)}{\min(i,j)}\right)^2 \right]}{\left(i \times j\right)^y} \tag{3.22}$$

where $\alpha_{\max} \in [0\ 1]$ is the maximum collision efficiency, and $\{x, y\}$ are other fitting parameters. The numerator of Equation (3.22) models the influence of size ratio in floc collisions, whereas the denominator includes the effect of hydrodynamic forces acting on the aggregate, which scale with the floc size. Selomulya et al. [18] used $\left(\alpha_{\max}, x, y\right) = \left(1.0, 0.1, 0.1\right)$ to model

the colloidal aggregation in turbulent flows, and the PBM predictions closely matched their experimental observations. Several subsequent studies in this area implemented Equation (3.22) in their population balance models [21, 22, 36, 37, 42], also using $\left(x, y\right) = \left(0.1, 0.1\right)$, but varying $\alpha_{\max}$ with different simulation set ups [42] or the type and dosage of flocculants [21, 22, 36].

Despite the fact that good population balance predictions for shear-induced aggregation have been obtained by using Selomulya's [18] collision efficiency correlation, there are essential differences between this empirical approximation and Kusters et al. [60] original model. This can be clearly observed by comparing Figures 3.4 (a) and 3.4 (b), which show how the collision efficiency varies with different combinations of class sizes (i, j). The values of $\{\alpha_{\max}, x, y\}$ in Figure 3.4 (b) were carefully chosen to attempt to match the predictions of Kusters' original model using Equation (3.22). When $i = 1$, as j increases, the collision efficiency from Selomulya et al. [18] underestimates $\alpha_{i,j}$ when compared to Kusters et al. [60]. When $i = [15\ 25]$ and $j \geq 15$, Equation (3.22) predicts an almost asymptotic behaviour for $\alpha_{i,j}$, which actually does not occur in the Kusters' [60] model. Furthermore, the initial growth in $\alpha_{i,j}$ for $j \geq 15$ occurs at very small values of i when Equation (3.22) is used, but this increase takes place at much greater values of i based on the original model [60]. For instance, $\alpha_{6,20}^{\text{Selomulya}} \approx \alpha_{15,20}^{\text{Kusters}}$. The difference between the predictions can be minimized by substituting the class indices (i, j) in Equation (3.22) by the total number of primary particles forming the aggregates, i.e., (n_i, n_j). This modification was initially proposed by Vlieghe et al. [77], and the collision efficiency values for this approach are displayed in Figure 3.4 (c). Even though this modification produces values of $\alpha_{i,j}$ that are much closer to the original model [60], the Vlieghe et al. [77] collision efficiency model is not written in terms of the mass fractal dimension, and thus predicts the same collision efficiency for different D_f.

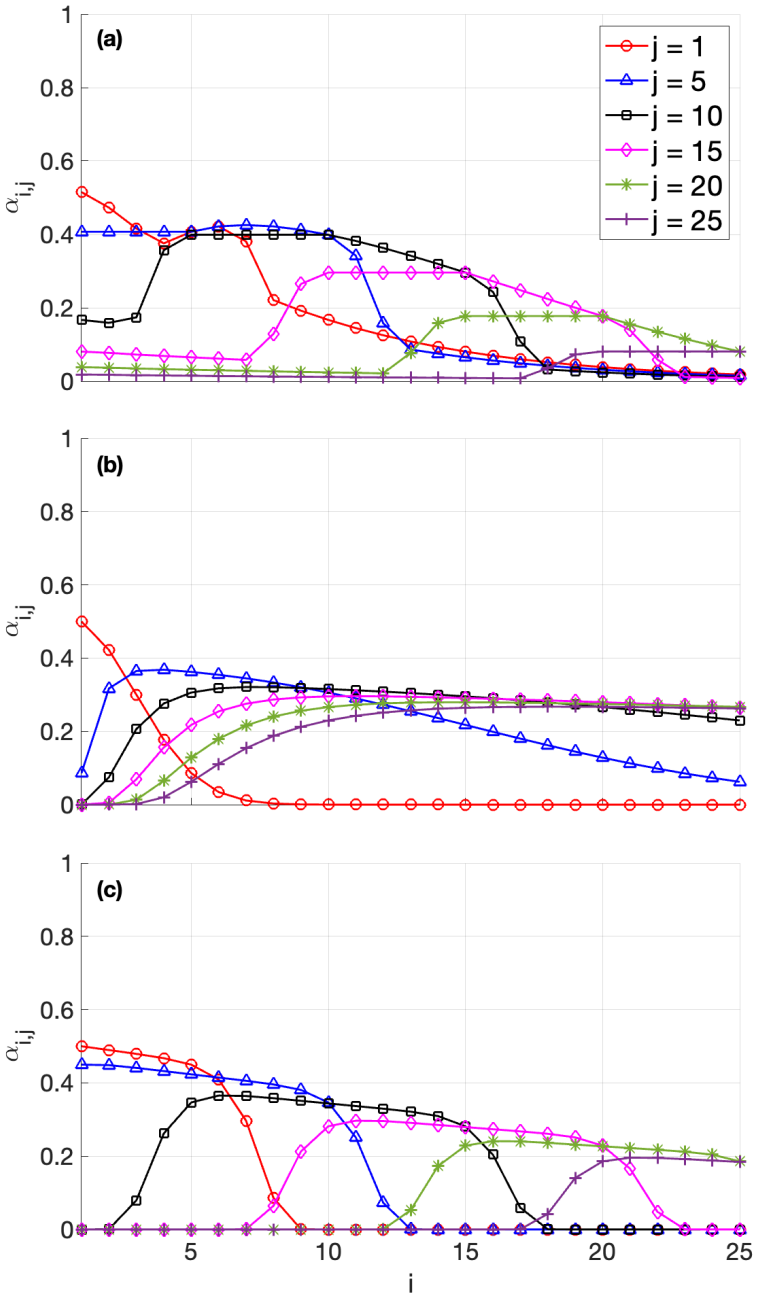

Figure 3.4: Comparison among (a) Kusters et al. [60] original collision efficiency model ($A = 1.37 \times 10^{-20}$ J, $d_o = 2\mu$m, $D_f = 2.5$) and its empirical approximations from (b) Selomulya et al. [18] ($\alpha_{\max} = 0.5$, $x = 0.1$, $y = 0.1$) and (c) Vlieghe et al. [77] ($\alpha_{\max} = 0.5$, $x = 0.0001$, $y = 0.03$).

To address the shortcomings of the collision efficiency approaches of Selomulya et al. [18] and Vlieghe et al. [77], we re-wrote Equation (3.4) in terms of the dimensionless aggregate

size $R^*_{g,i} = R_{g,i}/r_o$ instead of class index i, and varied y with the mass fractal dimension:

$$\alpha_{i,j} = \alpha_{\max} \cdot \frac{\exp\left[x\left(1 - \frac{\max(R^*_{g,i}, R^*_{g,j})}{\min(R^*_{g,i}, R^*_{g,j})}\right)^2\right]}{(R^*_{g,i} \cdot R^*_{g,j})^y} \quad ; \quad y = 0.3315 \cdot D_f - 0.717 \quad , \quad D_f \in [2.3\ 2.8] \quad (3.23)$$

The $y = f(D_f)$ was obtained by varying D_f from 2.3 to 2.8 and choosing the best value of y that could match the maximum collision efficiency for $j = 20$ from Kusters et al. [60] model. Then, $y = f(D_f)$ was obtained from the linear regression of y and D_f values. The curve of $j = 20$ was used as a reference because it guaranteed that the other peaks for $j < 20$ were not too low and for $j > 20$ were not too high when compared to the original model [60]. Figure 3.5 shows Kusters et al. [60] and Equation (3.23) for $D_f = \{2.4, 2.7\}$. Comparing Figures 3.5 {(a),(b)} and {(c),(d)}, it is clear that our empirical model can qualitatively capture the intricate details of Kusters et al. [60] collision efficiency. Interestingly, when $\{\alpha_{\max}, x, y\} = \{0.35, -0.25, 0\}$, Equation (3.23) retrieves the same collision efficiency values from Kroll-Rabotin et al. [2], who simulated finite Re collisions between solid spheres with different size ratios.

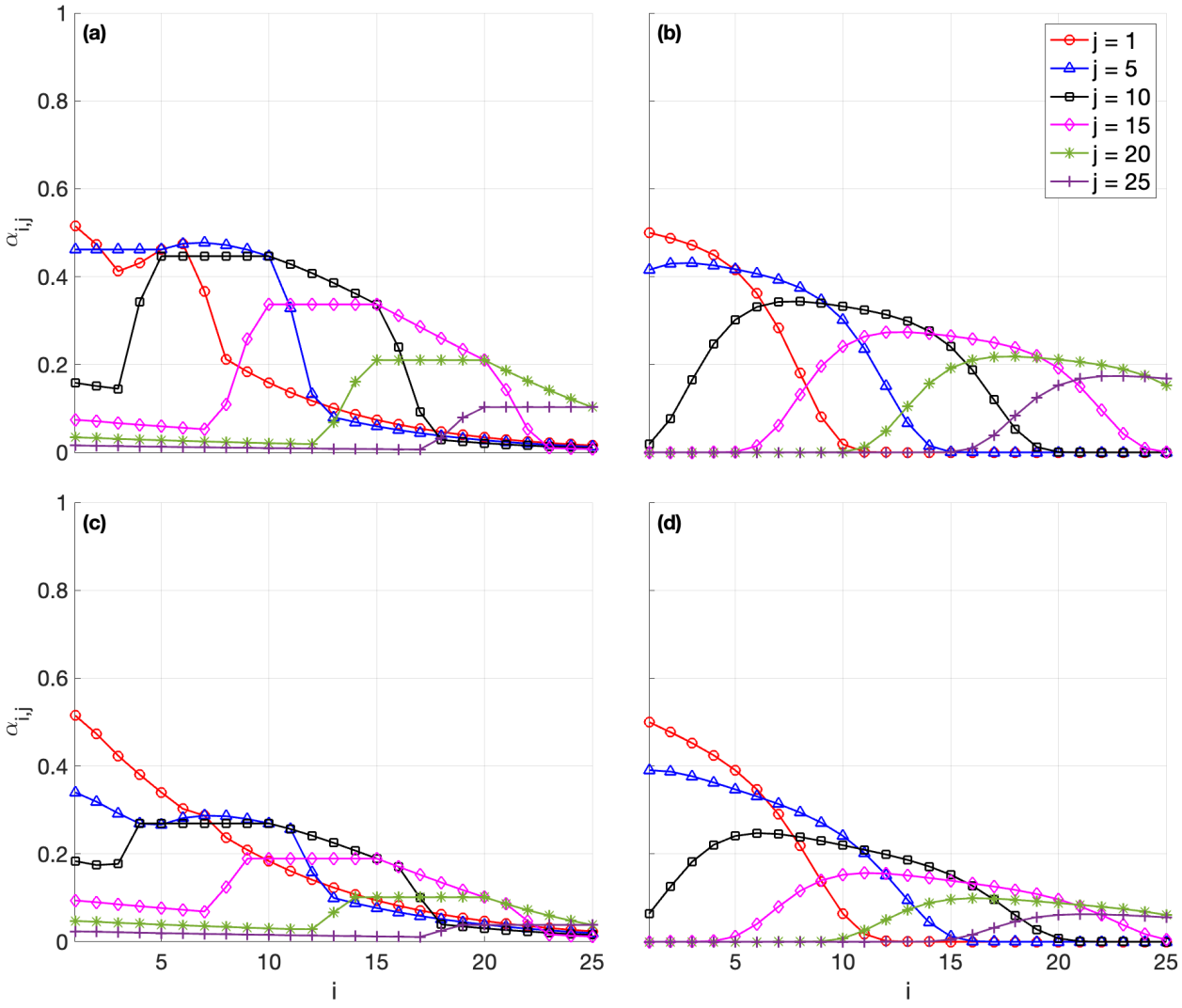

Figure 3.5: Comparison between the Kusters' [60] original collision efficiency model and the empirical approximation proposed during the current study. In figures (a) and (b), $D_f = 2.4$, whereas in figures (c) and (d), $D_f = 2.7$. The paramters $A_h = 1.37 \times 10^{-20}$ J and $d_o = 2\mu$m were used in to obtain $\alpha_{i,j}$ values from Kusters' model [60], which are is presented in figures (a) and (c). The values $(\alpha_{\max}, x) = (0.5, 0.02)$ were used to obtain the $\alpha_{i,j}$ values from the collision efficiency model of the current work, which are presented in figures (b) and (d).

In Cifuentes' [17] breakage experiments, the observed flocs were quite compact ($D_f \geq 2.2$) and, according to Saxena et al. [10], the flow disturbance caused by dense aggregates is similar to that of solid rigid spheres. Therefore, the collision efficiency of compact flocs might be approximated by the one for solid spheres. To validate this hypothesis and investigate the role of permeability in floc collisions, two different sets of $\{\alpha_{\max}, x, y\}$ values were chosen for Equation (3.23), which are summarized in Table 3.2.

Table 3.2: Parameters of Equation (3.23) for the modelling two different types of collisions.

Collision type	Symbol	$\alpha_{\max}$	x	y
Permeable flocs	α^{p}	0.50	0.02	$0.3315 \cdot D_f - 0.717$
Impermeable flocs	α^{i}	0.35	0.25	0.00

In summary, the collision efficiency is often included in the orthokinetic collision mechanism to account for the hydrodynamic and cohesive interactions between flocs, which affect the aggregation trajectories is shear flow [93]. Kusters et al. [60] proposed one of the most comprehensive collision efficiency models, which includes the effect of system forces and floc permeability in collisions. Due to the inherent complexity of Kusters' [60] model, Selomulya et al. [18] and Vlieghe et al. [77] developed empirical approximations that were thought to obtain similar values to Kusters' collision efficiency model. In the current work, we showed that there are clear differences between the collision efficiency models from Selomulya et al. [18], Vlieghe et al. [77], and Kusters et al. [60]. To overcome these differences, we proposed a modified version of Selomulyas' collision efficiency, i.e., Equation (3.23), which is qualitatively equivalent to Kusters' original model (see Figure 3.5). Equation (3.23) can also determine the collision efficiency of impermeable solid rigid spheres at finite Reynolds numbers, which were investigate via CFD by Kroll-Rabotin et al. [2]. To investigate the role of floc permeability in the modelling of breakage experiments, two different collision types are investigated in this work using Equation (3.23), which are summarized in Table 3.2.

3.2.2 Breakage Kernel

The breakage kernel, S_i, determines the fragmentation rate of class i aggregates due to the effect of shear. When aggregates are formed only from the destabilization of primary particles, i.e., without the addition of polymer flocculants, two different models can be used to calculate the breakage kernel [20]. The first one is an empirical power-law relationship [77, 97],

$$S_i = c_1 \cdot G^{c_2} \cdot \left(\frac{R_{g,i}}{R_p} \right)^{c_3} \tag{3.24}$$

where c_1, c_2, and c_3 are fitting parameters. The second approach consists of a semi-empirical model that was initially proposed by Delichatsios and Probstein [98] to describe

the breakage frequency of droplets in turbulent flows, and then it was modified by Kusters [99] to predict the fragmentation rate of colloidal flocs. It assumes that the local shear rate experienced by a class i aggregate varies in magnitude according to a normal distribution and that there is a critical shear rate, $G_{b,i}$, that causes the breakage of this aggregate. In laminar flow, Kusters [99] proposer the following breakage kernel equation:

$$S_i = \left(\frac{2}{\pi}\right)^{1/2} G \exp\left[-\left(\frac{G_{b,i}}{G}\right)^2\right] \tag{3.25}$$

According to Wang et al. [41], the critical breakage shear rate in laminar flow is related to aggregate size:

$$G_{b,i} = \sqrt{\frac{B}{\left(R_{g,i}\right)^{2/p}}} \tag{3.26}$$

where B is a fitting parameter and p the scaling exponent obtained from the aggregate strength relationship between floc steady-state size and shear rate [see Equation (2.21)]. According to Selomulya et al. [18], who initially proposed Equation (3.26), $p = 2.0$. However, based on recent experiments [9, 17, 82, 85, 88] and simulations [9, 40, 87], $p \approx 0.5$. This indicates that $G_{b,i}$ scales with the aggregate area, which makes more sense from a physical standpoint. Equation (3.26) also reveals that $G_{b,i}$ is a local property of the aggregate because it depends on the floc size and strength.

Since the exponential breakage kernel, Equation (3.25), comes from a phenomenological understanding of aggregate breakage, this model is not limited to experimental conditions, unlike the empirical power-law breakage kernel. Accordingly, only the exponential breakage kernel was considered in the current work, with $p \approx 0.5$.

3.2.3 Breakage distribution function

The breakage distribution function, $\Gamma_{i,j}$, describes the formation of flocs from the i-th class size due to the breakage of aggregates from the j-th class. In other words, it determines the size of fragments that are formed after each breakage event. Most population balance studies on colloidal aggregation and breakage assume symmetric binary breakage [11, 18, 19, 22, 36, 37, 41, 42], in which any breakage event results in two identical fragments with half the size of the original floc. Hence, in the lumped discrete PBE from [73, 75], a floc from the $j = i + 1$ class can only break into two fragments from the i-th class size.

Although the symmetric binary breakage is relatively easy to implement and produced good predictions of aggregate average size in previous population balance studies [11, 18, 19, 22, 36, 37, 41, 42], recent CFD simulations at low Reynolds numbers, i.e., negligible flow inertia, showed that the breakage of compact flocs is not always symmetric, as they can also break via an erosion mechanism [68]. This behaviour was also observed by Saxena [40] at finite Reynolds number, where both convection and diffusion are accounted for in the fluid-particle interactions. In this work, the breakage and restructuring of ten different aggregates with the same initial D_f and R_g was investigated via CFD simulations. It was observed that colloidal aggregates do not follow any particular breakage mechanism in simple shear flow, i.e., fragments of varying sizes occur regardless of the system shear rate.

Despite the fact that Saxena's [40] findings cannot be extrapolated to a population of aggregates due to the small number of simulated aggregates in this study, it is worthwhile to investigate via population balance modelling the fragmentation mechanism can better predict the breakage and restructuring kinetics of aggregates. To perform this analysis, we propose a new breakage distribution function, where the probability of forming a fragment of k primary particles from the breakage of a j-th class floc follows a geometric progression, i.e.,

$$w_{k,j} = \frac{r^{k-1}\,(1-r)}{1-r^{n_j^b}} \tag{3.27}$$

where r is the common ratio, i.e., the ratio between two consecutive numbers of the geometric sequence, and $n_j^b = n_{p,j}/2$ is the number of breakage scenarios for the j-th class floc. To vary the value of r for different breakage scenarios, we define a new fitting parameter, $s = r^{-n_{p,j}/4} \in \,]0\ 1[$, which corresponds to the chance of producing a fragment with a quarter of the size of the parent floc compared to the chance of creating aggregates half the size of their parent aggregate. The effect of s on the fragment size probability ($w_{k,j}$) is illustrated in Figure 3.6 for the case of an aggregate from class size $j = 4$, where $n_{p,4} = 8$ and $n_4^b = 4$. As can be seen, when $s \to 0$, the probability of creating any aggregate smaller that $n_{p,j}/2$ drops to 0, i.e., only binary breakage occurs. Conversely, if $s \to 1$, the chance of producing an aggregate of $n_j/2$ particles is the same as $n_j/4$, so the geometric progression is actually flat, in which uniform binary breakage takes place. If s has intermediate values between 0 and 1, the breakage mechanism is non-uniform, that is, the fragment size probabilities are neither symmetric nor uniform, transitioning between these two breakage mechanisms according to

Equation (3.27).

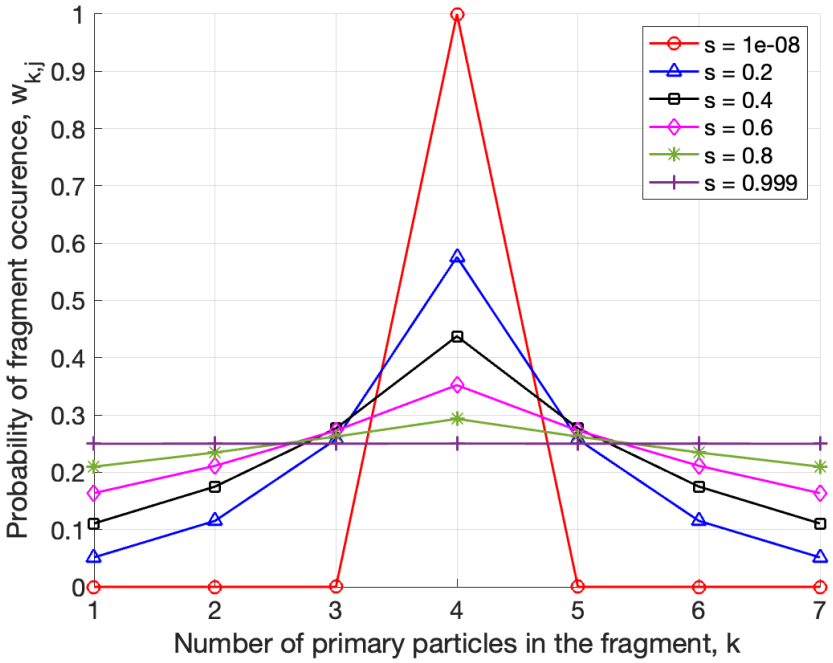

Figure 3.6: Breakage probabilities of class $j = 4$ aggregates ($n_{p,j} = 8$) for different values of s parameter.

Since all breakage scenarios must be accounted for in our model, the breakage distribution function ($\Gamma_{i,j}$) is therefore written as

$$\Gamma_{i,j} = \begin{cases} \sum_{k=n_{p,i}}^{n_{p,i+1}-1} \mathrm{w}_{k,j} \cdot f_{k,j} \cdot \iota_{k,i}; \quad i = 1 \\ \sum_{k=n_{p,i}}^{n_{p,i+1}-1} \mathrm{w}_{k,j} \cdot f_{k,j} \cdot \iota_{k,i} + \sum_{k=n_{p,i-1}}^{n_{p,i}-1} \mathrm{w}_{kj} \cdot f_{k,j} \cdot \left(1 - \iota_{k,i}\right); \quad i \in [2 \;\; (j-1)] \\ \sum_{k=n_{p,i-1}}^{n_{p,i}-1} \mathrm{w}_{k,j} \cdot f_{k,j} \cdot \left(1 - \iota_{k,i}\right); \quad i = j \end{cases} \tag{3.28}$$

where $f_{k,j}$ is the total number of fragments with k primary particles that can be produced from the breakage of the j-th class parent floc, i.e.,

$$f_{k,j} = \begin{cases} 1; & k = n_{p,j-1} \neq 2^{j-2} \\ 2; & k = n_{p,j-1} = 2^{j-2} \end{cases} \tag{3.29}$$

and $\iota_{k,i}$ is the percentage of a fragment with k primary particles that belongs to a i-th class size floc, given by

$$\iota_{k,i} = \frac{n_{p,i+1} - k}{n_{p,i+1} - n_{p,i}}; \quad n_{p,i} \leq k < n_{p,i+1} \tag{3.30}$$

Figure 3.7 illustrates the four different breakage scenarios of class $j = 4$ aggregates ($n_j = 8$) for different values of s. When $s = 1{\cdot}10^{-8}$, symmetric binary breakage takes place, creating flocs with only four primary particles because the other types of fragments have zero chance of happening; that is, ($w_{k,j} = 0.25$). When $s = 0.9999$, uniform binary breakage occurs, where all fragments have the same birth probability, i.e., $w_{k,j} = 0.25$. Finally, when $s = 0.5$, the breakage is non-uniform and $w_{k,j}$ follows the geometric progression from Equation (3.27). It is important to mention that only binary fragmentation was considered regardless of the breakage mechanism; that is, each breakage event produces only two fragments, i.e., $\sum_{i=1}^{j} \Gamma_{i,j} = 2$ for any value of s.

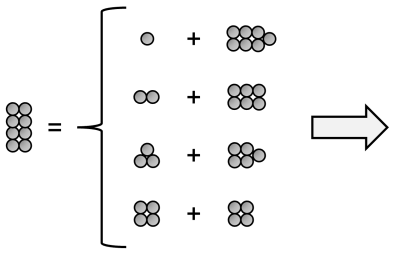

k	$f_{k,j}$	$\iota_{k,i}$	$s = 1{\cdot}10^{-8}$ $w_{k,j}$	$s = 0.9999$ $w_{k,j}$	$s = 0.5$ $w_{k,j}$
1	1	1	0	0.25	0.14
2	1	1	0	0.25	0.20
3	1	0.5	0	0.25	0.28
4	2	1	1	0.25	0.39
5	1	0.75	0	0.25	0.28
6	1	0.5	0	0.25	0.20
7	1	0.25	0	0.25	0.14

Figure 3.7: Breakage probabilities of class $j = 4$ aggregates ($n_{p,j} = 8$) for different values of s parameter.

In summary, the binary symmetric breakage is often assumed to be the only breakage mechanism in PBMs for shear-induced aggregation [11, 18, 19, 22, 36, 37, 41, 42]. Recent CFD studies from Saxena [40] showed that different breakage mechanisms can take place at the same flow conditions, and there is no strong prevalence of one type of breakage mechanism over another as both of them had similar occurrence frequencies. Since Saxena's [40] CFD simulations were limited to only a small number of aggregates, the current study developed a new breakage distribution function to investigate the breakage mechanism that can best predict the behaviour of populations of aggregates from Cifuentes' [17] breakage

experiments.

3.3 Fractal dimension ODE

The fractal dimension ordinary differential equation (ODE) describes the rate of change in the mass fractal dimension with time [18, 37],

$$\frac{dD_f}{dt} = t_r^{-1}\left(D_{f,ss} - D_f\right) \tag{3.31}$$

where t_r^{-1} is the rate of aggregate restructuring and $D_{f,ss}$ is the steady-state fractal dimension. This equation was initially proposed by Selomulya et al. [18], who successfully predicted the evolution of the mass fractal dimension in shear-induced aggregation experiments. This approach assumes that fractal dimension does not vary with aggregate size, where the morphology of all class sizes at a given time is represented by a single value of D_f. Hence, Equation 3.31 can only obtain the global morphology of populations of aggregates.

In order to determine t_r^{-1}, Selomulya et al. [18] proposed the following equation:

$$t_r^{-1} = c_1\left(\frac{D_{32}}{d_o}\right)^{c_2} + c_3 AB \tag{3.32}$$

where $\{c_1, c_2, c_3\}$ are fitting parameters and $AB = f(A_i^B, A_i^D, B_i^B, B_i^D)$ is a coefficient that compounds the effect of aggregation and breakage kinetics based on the birth and death terms of the PBE Equation (3.6). Later, Bonanomi et al. [37] criticized Equation (3.32), showing that $c_3 AB \ll c_1\left(\frac{D_{32}}{d_o}\right)^{c_2}$ and that the validation of $\{c_1, c_2\}$ values was not provided by Selomulya et al. [18]. To overcome these issues, Bonanomi et al. [37] used t_r^{-1} as a fitting parameter, which varied with the system shear rate. More recent population balance studies on shear-induced aggregation, which also considered t_r^{-1} a fitting parameter, obtained reasonably good predictions when compared to experimental data [22, 36, 42]. Therefore, the current work also uses t_r^{-1} as a fitting parameter.

Since many population balance studies investigated shear-induced colloidal aggregation, the steady-state fractal dimension was always considered equal to the maximum fractal dimension, i.e., $D_{f,ss} = D_{f,\max}$ [18, 22, 36, 37, 42]. However, as can be seen in Figure 3.8 (a), this assumption cannot be made for Cifuentes' experiments [17], where $D_{f,\max}$ mostly occurred at the second data point of the breakage stage. Moreover, the experiments at lower shear rates produced oscillations in D_f values, and therefore $D_{f,ss}$ could not be obtained

based on the average of the last experiment data points. Thus, to obtain a good overall prediction of D_f with time, we considered $D_{f,ss}$ to be a fitting parameter.

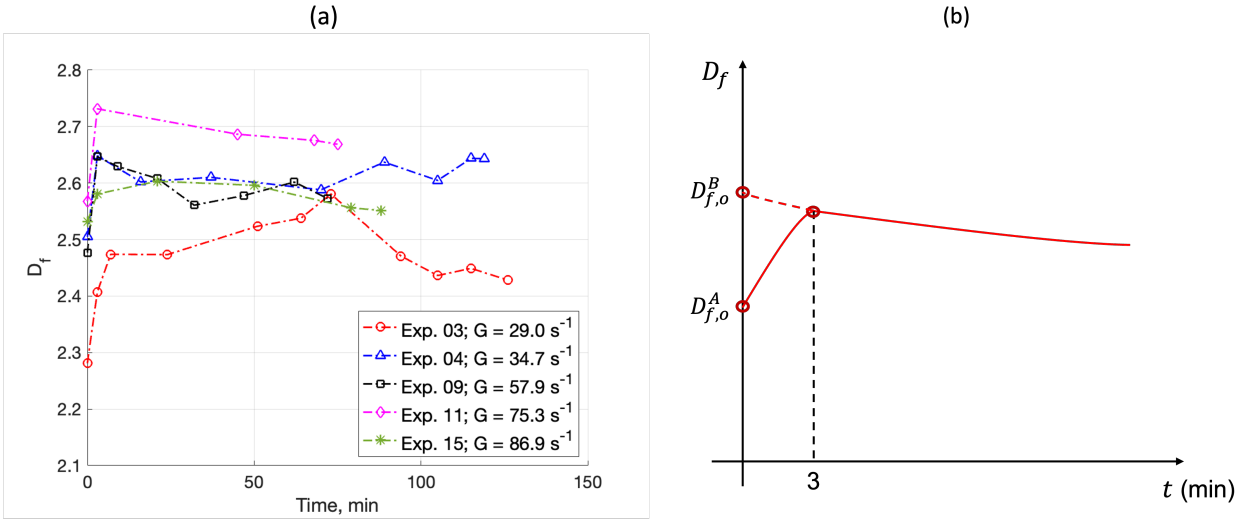

Figure 3.8: a) Example of mass fractal dimension kinetics of Cifuentes breakage stage experiments [17] at different shear rates; b) Illustration of the short-term and long-term restructuring kinetics, and the two different initial fractal dimensions considered in this work.

In order to solve Equation (3.31), the initial fractal dimension at 0 min ($D_{f,o}$) must be provided as an input parameter. As presented in Figure 3.8 (b), two different values of $D_{f,o}$ are considered in this work, one obtained from the last data point of Cifuentes' aggregation stage ($D^A_{f,o}$), and the other one inferred from the kinetic trend of the breakage stage ($D^B_{f,o}$). The reason for considering these two different initial values comes from the fact that the measurements in Cifuentes' experiments were periodic, i.e., not continuous, and that the first data point in the breakage stage always occurred 3 min after the step increase in the shear rate. As a consequence, the sharp increase in the fractal dimension between 0 min and 3 min might have occurred in the first few seconds after the shear rate increase, which justifies inferring $D_{f,o}$ from the breakage stage data. Additionally, two different restructuring mechanisms were observed in at least one experiment for each shear rate: rapid densification followed by a slow elongation. Since these two restructuring mechanisms cannot be modelled at the same time by Equation (3.31), the two different $D_{f,o}$ values were considered in this study. Therefore, when $D_{f,o} = D^A_{f,o}$, Equation (3.31) can only model the short-term densification, and when $D_{f,o} = D^B_{f,o}$, Equation (3.31) models the long-term densification.

3.4 Numerical method to solve the PBM

Based on the information presented in the Sections 3.2 and 3.3, a total of 26 ordinary differential equations must be solved numerically at each time step, of which one equation tracks the global mass fractal dimension (3.31), and 25 PBEs (3.6) determine the aggregate size distribution. Hence, the initial condition of this ODE system is $\boldsymbol{y_o} = [D_{f,o}\ \boldsymbol{N_o}]$. The ode45 built-in function from MATLAB R2021a was used in this work, which solves the ODE system via the 4^{th} and 5^{th} order Runge-Kutta explicit method. The code developed in this work was built upon a template code available in the Appendix A of Selomyla PhD thesis [72]. This template code was also used by Selomulya et al. [18] to model shear-induced aggregation in turbulent flows via PBM.

To guarantee that the solids mass is conserved in this PBM model, the absolute relative error ($|E_{r,m}|$) between the initial solids volume (V_o^{s}) and time m solids volume (V_m^{s}) is monitored at each time step. When $|E_{r,m}| > 1 \cdot 10^{-4}$, the simulation stops and the model parameters are readjusted.

3.5 Summary of case studies and hypotheses

Table 3.3 summarizes the four different case studies investigated in this work, which allows us to investigate the effect of modelling short-term ($D_{f,o}^{A}$) and long-term restructuring ($D_{f,o}^{B}$), and to determine whether aggregates collide similarly to either solid rigid spheres (α^{i}) or permeable flocs (α^{p}).

Table 3.3: Summary of case studies

Case study ID	Collision efficiency model	Initial fractal dimension
1	α^{i}	$D_{f,o}^{A}$
2	α^{p}	$D_{f,o}^{B}$
3	α^{i}	$D_{f,o}^{A}$
4	α^{p}	$D_{f,o}^{B}$

Based on the discussion from Section 3.2, three hypotheses will be investigated in this work:

- Since dense flocs ($D_f \geq 2.3$) disturb the flow similarly to solid rigid spheres [10], floc permeability does not play a major role in the collision efficiency, i.e., α^{p} and α^{i} models should retrieve similar population balance resulSts.
- Since the breakage of compact flocs ($D_f \geq 2.3$) can form aggregates of different sizes [40, 68] and there is no strongly favoured breakage mechanism [40], the assumption made by most population balance studies that floc breakage always generates fragments of equal sizes [18, 19, 22, 36, 37, 41, 42] is not correct. This hypothesis will be confirmed if $s \gg 0$ (fitting parameter from the breakage distribution function, see Section 3.2.3).
- In Cifuentes' [17] breakage stage, the initial short-term densification of aggregates is instantaneous, i.e., it occurs much faster than the observed time scale and measurement sampling time. This hypothesis will be correct if the population balance predictions using $D_{f,o}^{B}$ are more accurate than those obtained using $D_{f,o}^{A}$.

Chapter 4

Results and Discussion

This chapter presents and discusses the PBM results of the four case studies that were summarized in Section 3.5. First, the restructuring of aggregates is analyzed in Section 4.1 for the two initial fractal dimensions considered in this work: one focused on capturing the short-term densification ($D^A_{f,o}$); and the other focused on modelling the long-term restructuring ($D^B_{f,o}$). Then, the effect of these two initial conditions is discussed with regard to the average floc size and floc size distribution (FSD) in Section 4.2. The influence of the floc permeability in shear-induced collisions is also investigated in this section by comparing the average floc size and FSD results of the four PBM case studies to the experimental data from Cifuentes [17]. In this analysis, the case study that best models the experiments is selected. The physical meaning of the fitting parameters from the breakage kernel and breakage distribution function is then extracted from the PBM results involving the best case study.

4.1 Aggregate Restructuring

As explained in Section 3.3, the restructuring of populations of aggregates was modelled by the mass fractal dimension ODE Equation (3.31). To solve this equation, the initial fractal dimension was provided to the model. It should be recalled that the parameter $D^A_{f,o}$ was directly extracted from the last data point of the aggregation stage of Cifuentes' [17] experiments, whereas $D^B_{f,o}$ was inferred from the breakage stage, as illustrated in Figure 3.8 (b). Additionally, the aggregate rate of restructuring (t_r^{-1}) was manually changed until the D_f ODE matched the mass fractal dimension history of each experiment.

Figure 4.1 summarizes the evolution of the mass fractal dimension over time for the different initial conditions considered in this work, i.e., $D^A_{f,o}$ and $D^B_{f,o}$. The symbols represent

the data points and the continuous lines correspond to the PBM predictions. When $D_{f,o}^{A}$ is used, the fractal dimension ODE Equation (3.31) correctly models the initial short-term aggregate densification and the steady-state fractal dimension for all shear rates. However, when the maximum fractal dimension occurs at $t = 3$ min and $D_{f,o}^{A}$ is used, Equation (3.31) does not model the long-term floc elongation, and thus misses an important part of aggregate restructuring history. This can be observed for several experiments at different shear rates, e.g., Experiments 6 (Figure 4.1 (b)), 7 to 9 (Figure 4.1 (c)), 10 and 11 (Figure 4.1 (d)), and 13 (Figure 4.1 (e)). This modelling issue is solved by employing $D_{f,o}^{B}$ as the initial fractal dimension, where the long-term restructuring is clearly observed in the aforementioned experiments. Additionally, when $D_{f,\max} \approx D_{f,\mathrm{ss}}$, the fractal dimension remains practically constant throughout the entire duration of an experiment for simulations using $D_{f,o}^{B}$.

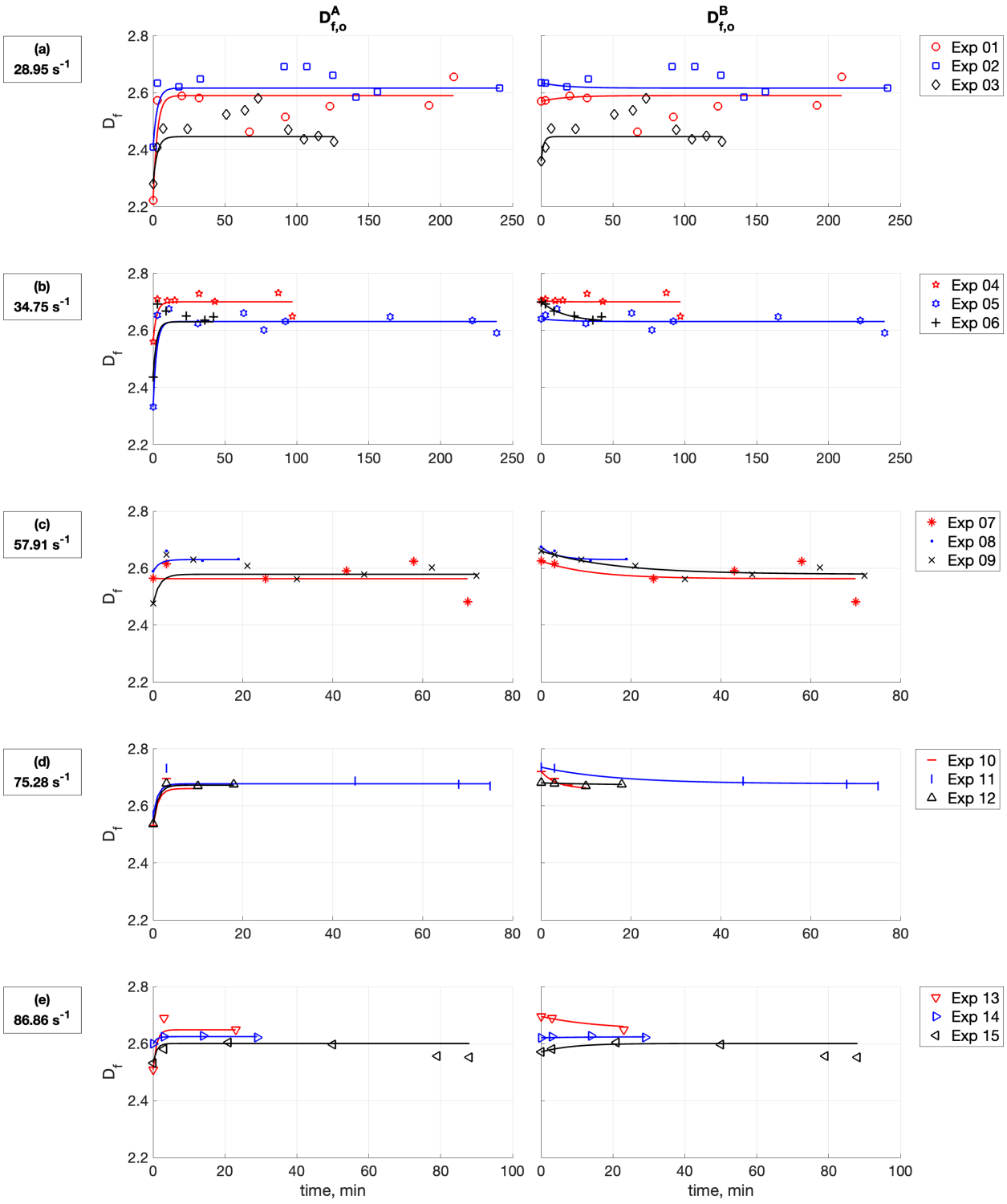

Figure 4.1: Mass fractal dimension evolution at different shear rates and initial conditions for all experiments modelled in this work. The continuous lines correspond to the population balance predictions, and the symbols represent the experimental data points.

Comparing the experimental data of Figures 4.1 (a) to (e), it seems that the fractal dimension at $G = 28.95\ \text{s}^{-1}$ has greater oscillations when compared to the experiments at higher shear rates. This visual observation is confirmed by calculating the average absolute relative error between the D_f data points of the experiment and the corresponding PBM, as shown in Table 4.1. These oscillations can be explained by the fact that, at lower shear rates, aggregates tend to experience more compression and elongation cycles during rotation because of the lower hydrodynamic stresses acting on them [10, 16]. Regarding $D_{f,o}^{A}$, which was obtained from the last data point of the aggregation stage, it was expected that it would be approximately the same for the 15 experiments modelled in this work. However, it ranged from 2.22 to 2.60, indicating that there was a noticeable difference in the initial aggregate morphology among experiments. Concerning $D_{f,o}^{B}$ and $D_{f,ss}$, which were both inferred from the breakage stage experimental data, both parameters should vary with the shear rate because the increase in hydrodynamic forces tends to create smaller and more compact flocs [9, 40, 43]. However, they both presented weak correlations with G, with $R^2 \approx 0.11$ for linear, exponential, and power-law fits. We believe that the differences between the expected and actual behaviour of parameters $\left(D_{f,o}^{A}, D_{f,o}^{B}, D_{f,ss}\right)$ is related to the methodology used to calculate the perimeter fractal dimension, which provides a single value to represent the morphology of samples containing thousands of aggregates, i.e., it can only retrieve the global morphology of floc populations. Additionally, colloidal aggregates are very fragile and sensitive to small variations in experimental conditions, making it very difficult to reproduce the initial and steady-state fractal dimensions.

Table 4.1 displays the average rate of restructuring ($\overline{t_r^{-1}}$) for the different shear rates and initial conditions modelled in this work. As can be seen, at any shear rate, the rate of restructuring is greater for $D_{f,o}^{A}$ when compared to the values for $D_{f,o}^{B}$. This difference is even more pronounced when $G \geq 57.91\ \text{s}^{-1}$, where $\left(\overline{t_r^{-1}}\right)_A$ is one order of magnitude higher than $\left(\overline{t_r^{-1}}\right)_B$. These results were expected because, when $D_{f,o}^{A}$ is used, there is a steeper change in floc morphology over time. It is important to mention that the rate of restructuring for $D_{f,o}^{A}$ varied with the shear rate following the linear relationship $\overline{t_r^{-1}} = m \cdot G$, where $m = 2.0 \cdot 10^{-4}$ ($R^2 = 1.0$). Bonanomi et al. [37], who modelled turbulent aggregation, also obtained a linear correlation between these two parameters, with $m = 2.375 \cdot 10^{-5}$. Even though this simple function can produce good predictions of the evolution of D_f with shear rate, the small values of m indicate that t_r^{-1} does not scale with the G.

Table 4.1: Aggregate restructuring results for the two initial conditions ($D^A_{f,o}$,$D^B_{f,o}$) considered in this work.

		Shear rate G s^{-1}				
		28.95	34.75	57.91	75.38	86.86
$D^A_{f,o}$	$\overline{\lvert E_r \rvert}_{D_f}$ (%)	1.67	0.52	0.32	0.11	0.09
	t_r^{-1} $(10^3 \cdot s^{-1})$	5.79	6.95	11.6	15.1	17.4
$D^B_{f,o}$	$\overline{\lvert E_r \rvert}_{D_f}$ (%)	1.38	0.23	0.19	0.03	0.06
	t_r^{-1} $(10^3 \cdot s^{-1})$	4.00	1.50	2.50	2.33	1.33

4.2 Aggregate breakage

4.2.1 Modelling approach

As explained in Chapter 3, the birth and death terms from the breakage mechanism of the PBE are written in terms of the breakage kernel (S_i) and the breakage distribution function ($\Gamma_{i,j}$). The former determines the floc breakage frequency, and the latter establishes the type of fragments that are formed after breakage. Each of these terms has one fitting parameter, which can be adjusted to match the experimental evolution of the average floc size and the floc size distribution (FSD) with time. The fitting parameter B (from the breakage kernel) has a direct influence on the average floc size. Since $S_i \propto e^{-B}$ the breakage kernel decreases with the increase in B. Therefore, for a given experiment, larger values of B result in less aggregate breakup and therefore in a larger steady-state floc size. This is illustrated in Figure 4.2, which shows the PBM results for different values of B. In the first set of PBM simulations, the initial guess $B = 1.0 \times 10^{-13}$ $m^4.s^{-2}$ was used. This value was obtained by varying the order of magnitude of B until the absolute relative error of the total solids volume was $|E_r| \leq 3\,\%$.

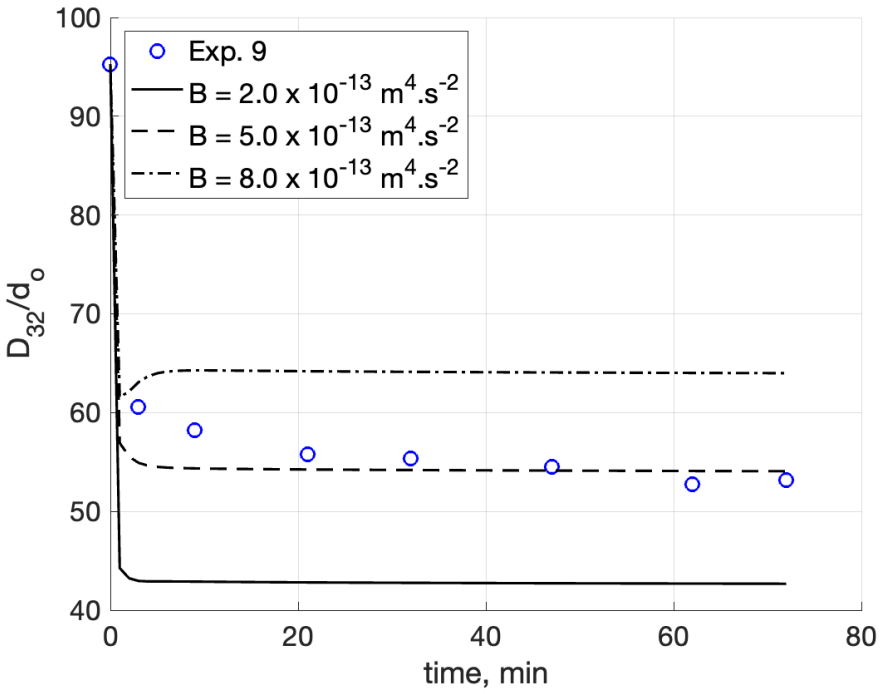

Figure 4.2: Effect of the fitting parameter B (from the breakage kernel) on the steady-state average floc size. The circles denote the data points from Exp. 9 ($G = 57.91$ s^{-1}), and the lines correspond to the PBM results for different values of B.

The fitting parameter s (from the breakage distribution function) controls how narrow the FSD can be by determining the breakage mechanism. If $s \approx 0$, the floc breakup is symmetric, producing two fragments of equal sizes. If $s \approx 1$, the breakage is uniform, where fragments of different sizes have the same probability of occurring. The effect of these two different breakage mechanisms on the FSD is demonstrated in Figure 4.3. As can be seen, symmetric fragmentation results in a narrow floc size distribution, whereas uniform breakage yields a broader FSD. Comparing the FSD from the experiment and the two PBM breakage scenarios of Figure 4.3, it seems that the actual breakage mechanism is non-uniform, i.e., the value of s that best model the experiment distribution is between 0 and 1. Thus, in the first run of simulations, the value $s = 0.5$ was considered as an initial guess for all experiments.

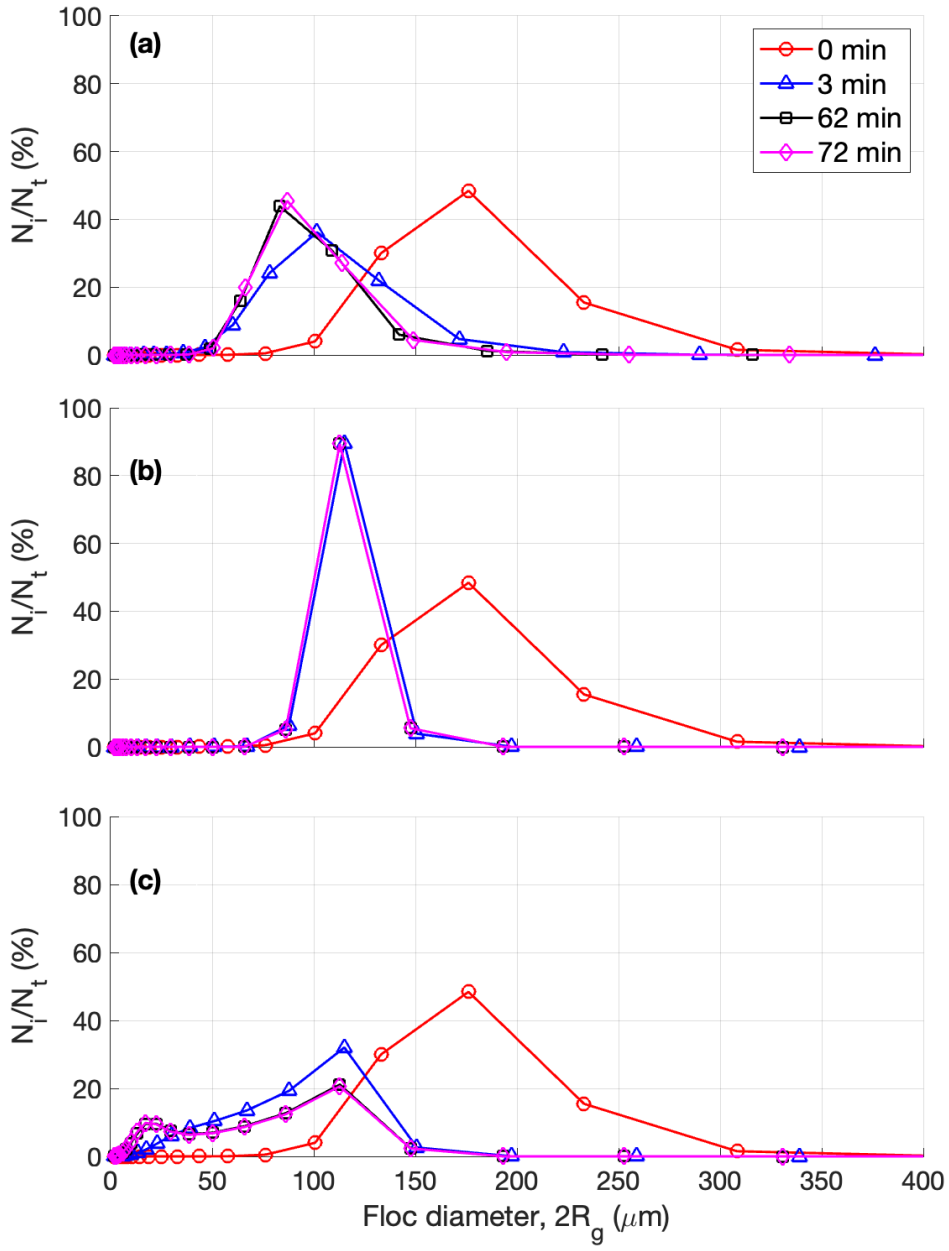

Figure 4.3: Effect of the fitting parameter s (from the breakage distribution function) on the floc size distribution (FSD): (a) data points from Exp. 9 ($G = 57.91$ s^{-1}); (b) PBM results for symmetric breakage ($s = 1.0 \times 10^{-6}$); (c) PBM results for uniform breakage ($s = 0.999$). Both PBM plots came from Case Study 1, which uses $D^A_{f,o}$ and α^{i}.

To model the average floc size and FSD, the following procedure was implemented: i) the fitting parameter B was adjusted while keeping $s = 0.5$ until the PBM predicted the steady-state surface mean diameter for each experiment; ii) the parameter s was modified while keeping B fixed until the experimental peak of the FSD at steady-state was retrieved

in the PBM results, as demonstrated in Figure 4.4; and iii) since the shape of the FSD can (slightly) affect the surface mean diameter evolution over time, the fitting parameter B was readjusted after finding the best value of s to model the experimental FSD.

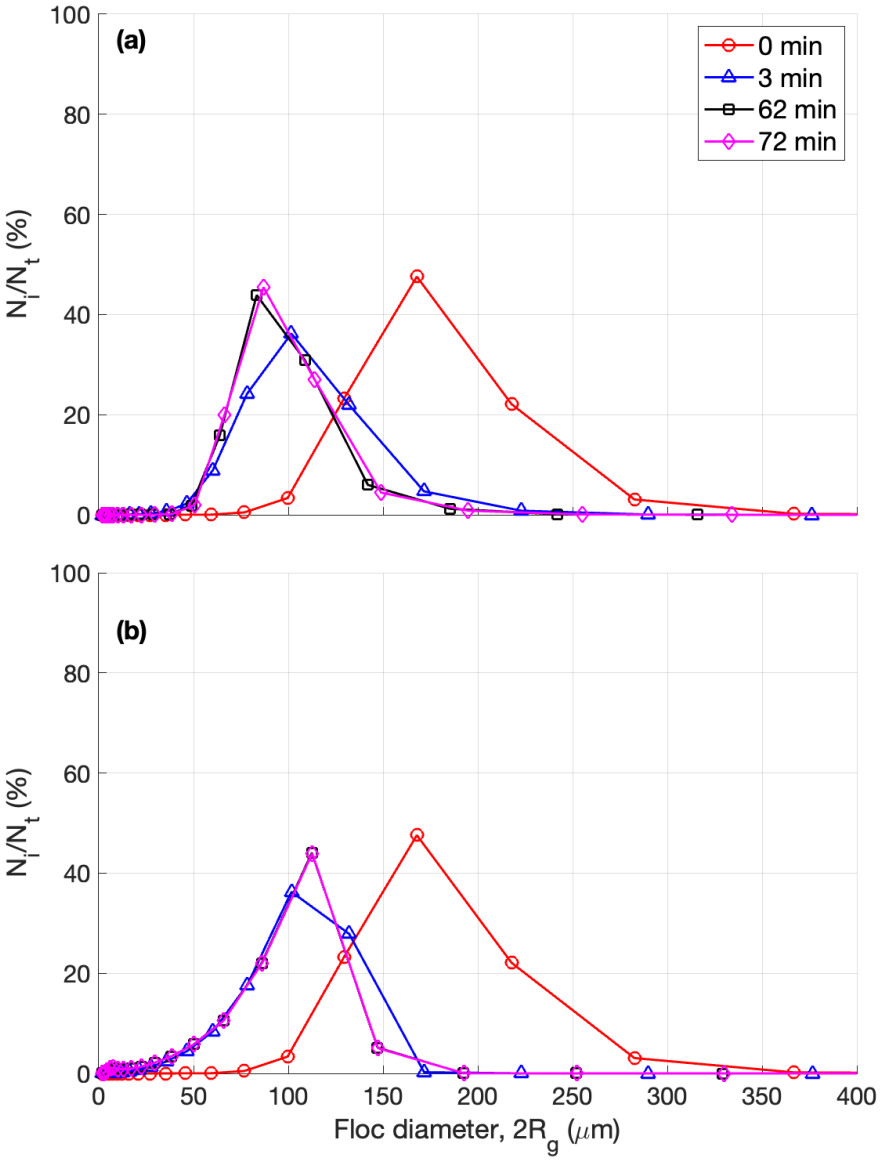

Figure 4.4: Modelling approach of the FSD, where the PBM results retrieve the same peak, i.e., y-axis value, of the experiment FSD at steady-state: (a) data points from Exp. 9 ($G = 57.91$ s^{-1}), where the steady-state FSD occurs at $t = 72$ min; (b) PBM results for Case Study 4 ($D^B_{f,o}$,α^{p}), where $s = 0.6$ and $B = 5.0 \times 10^{-13}$ m^4.s^{-2}.

In the following sections, the PBM predictions of the four case studies that were conducted in the present work are compared to Cifuentes' [17] breakage experiments. In Section 4.2.2,

the evolution of the dimensionless surface-mean aggregate diameter (D_{32}/d_o) is analyzed for different average shear rates. Similarly, the evolution of the FSD with time at different shear rates is discussed in Section 4.2.3, and the case study that best matches the experiment results is chosen. Then, Section 4.2.4 presents the values of the fitting parameters B and s for the best case study, and their physical meaning is discussed. To facilitate the comparison between the four case studies, the plots presented in the next two sections only show the results for one experiment per shear rate, and the average results from the fifteen experiments are summarized in Tables 4.2 and 4.3 . The experiments 01, 05, 09, 10, and 13 were chosen to represent the overall results at each shear rate because they have the greatest difference between $D_{f,o}^{A}$ and $D_{f,o}^{B}$ values, as shown in Figure 4.5. Hence, the impact of the initial fractal dimension on the modelling of the average floc size and FSD will be clearly seen in the plots presented in the next sections.

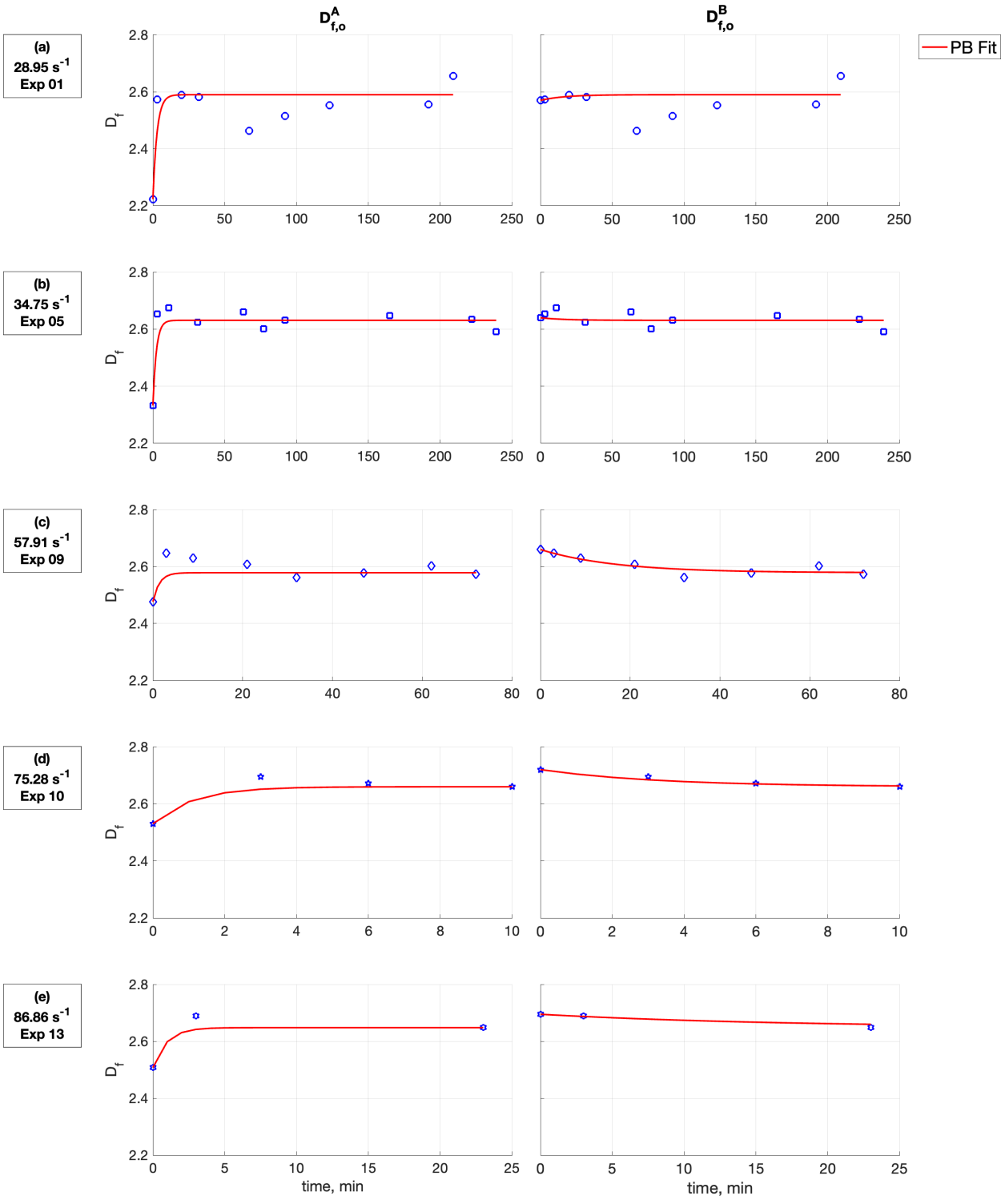

Figure 4.5: Mass fractal dimension evolution at different shear rates for the experiments with the highest difference between $D^A_{f,o}$ and $D^B_{f,o}$. The continuous lines correspond to the population balance predictions and the symbols are the experiment data points.

4.2.2 Average aggregate size

Figure 4.6 shows the evolution of the dimensionless average aggregate size over time at different shear rates for the four case studies investigated in this work. From the experimental data points, it is clear that the steady-state mean floc size decreases as the shear rate increases. This was expected because the hydrodynamic forces scale with shear rate, which results in smaller floc sizes for higher values of G. In all case studies, the PBM is able to predict the steady-state floc size for each experiment. However, the initial aggregate breakage at $t \leq 25$ min for the two lowest shear rates was over-predicted when the initial fractal dimension $D_{f,o}^{A}$ was considered. Interestingly, this over-prediction does not occur for the case studies using $D_{f,o}^{B}$. This confirms our hypothesis that the initial short-term aggregation occurs at the very first few seconds of the breakage stage and not at $t = 3$ min. For the higher shear rates, i.e., $G \geq 57.91$ s^{-1}, the PBM results are approximately the same for both $D_{f,o}^{A}$ and $D_{f,o}^{B}$ case studies. This can be explained by the fact that $|D_{f,o}^{A} - D_{f,o}^{B}|$ is lower at higher shear rates, which yields similar results for these two different initial fractal dimensions. This can be clearly seen in Figure 4.5, where $|D_{f,o}^{A} - D_{f,o}^{B}| \geq 0.30$ for $G < 57.91$ s^{-1}, and $|D_{f,o}^{A} - D_{f,o}^{B}| \leq 0.19$ for $G \geq 57.91$ s^{-1}.

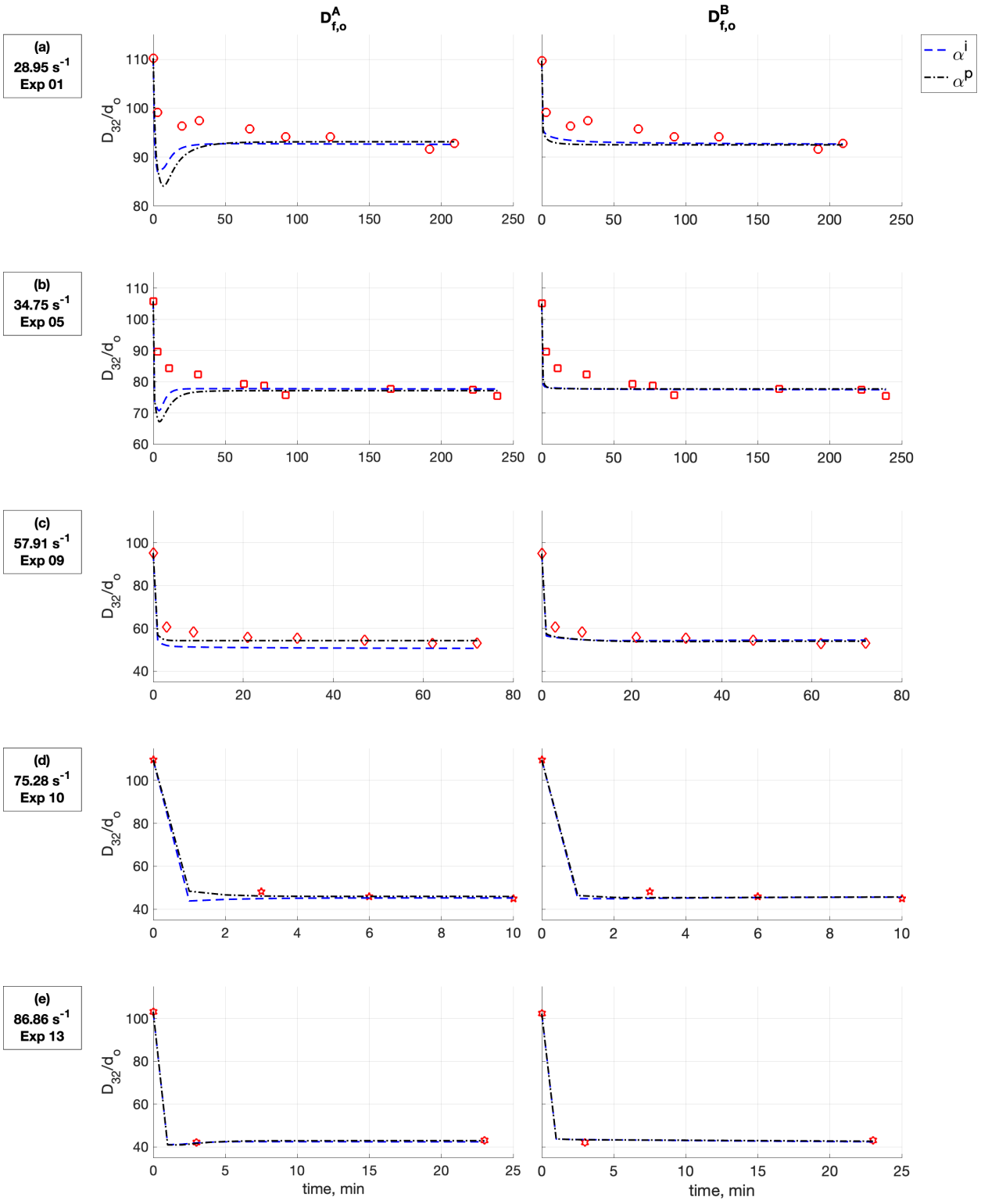

Figure 4.6: Dimensionless surface-mean floc size evolution at different shear rates. The symbols correspond to experimental data, whereas the dashed lines (−−) and dash-dotted lines (−·) represent PB results for α^i and α^p collision models, respectively.

Concerning the effect of floc permeability on the average aggregate size, simulations with both α^{i} and α^{p} resulted in similar PBM fits for all shear rates. This visual observation was quantitatively confirmed by comparing the average absolute relative error of the surface-mean floc size ($\overline{|E_r|}_{d_{32}}$) between case studies involving α^{i} and α^{p} for each initial fractal dimension, $D^A_{f,o}$ and $D^B_{f,o}$. The values of $\overline{|E_r|}_{d_{32}}$ are displayed in Table 4.2. These results indicate that the overall collisions between compact flocs ($D_f \geq 2.2$) are similar to collisions between solid rigid spheres. Moreover, it appears that the permeability can be neglected in collision efficiency models if the parameter of interest is the average floc size.

Table 4.2: Average absolute relative error of the surface-mean diameter, $\overline{|E_r|}_{d_{32}}$, for the four PBM case studies at different shear rates.

			Shear rate G (s^{-1})				
			28.95	34.75	57.91	75.38	86.86
$\overline{\lvert E_r\rvert}_{d_{32}}$ (%)	$D^A_{f,o}$	α^{i}	3.19	1.31	1.60	0.34	0.53
		α^{p}	3.38	1.60	1.21	0.35	0.54
	$D^B_{f,o}$	α^{i}	2.67	0.94	0.97	0.37	0.63
		α^{p}	2.82	0.92	1.01	0.30	50.59

4.2.3 Floc size distribution

Figure 4.7 displays the evolution of the aggregate size distribution based on the percentiles (d_{10}, d_{50}, d_{90}) for the different case studies investigated in this work. These percentiles were chosen because they can characterize the range of floc sizes in the distribution. Also, it is easier to compare the different case studies by using percentiles than by using a more conventional FSD plot. Comparing the experimental results at steady-state, smaller values of percentiles are obtained with the increase in the shear rate, which is a consequence of higher breakage rates. For the experiments conducted at the two lowest shear rates, when $D^A_{f,o}$ is considered, an over-prediction of floc breakage occurs for the percentiles d_{50} and d_{90}. Similarly to what was observed for the dimensionless floc size, this over-prediction does not occur when $D^B_{f,o}$ is used. However, for both initial fractal dimensions, the PBM predicts smaller d_{10} values throughout the entire simulation when compared to the experimental data. This error tends to decrease at higher shear rates, e.g., when $G \geq 75.28\ \mathrm{s}^{-1}$, the PBM predictions for d_{10} are very close to the experiment results. Comparing the overall PBM fits for the different collision scenarios, the simulations with both permeable and impermeable floc models yielded very similar results for the percentiles d_{50} and d_{90}. Nevertheless, the case

studies based on the permeable collision efficiency, α^{p}, obtained a better fit for d_{10}. This refutes our hypothesis that permeability does not play a major role in the collision efficiency of dense flocs.

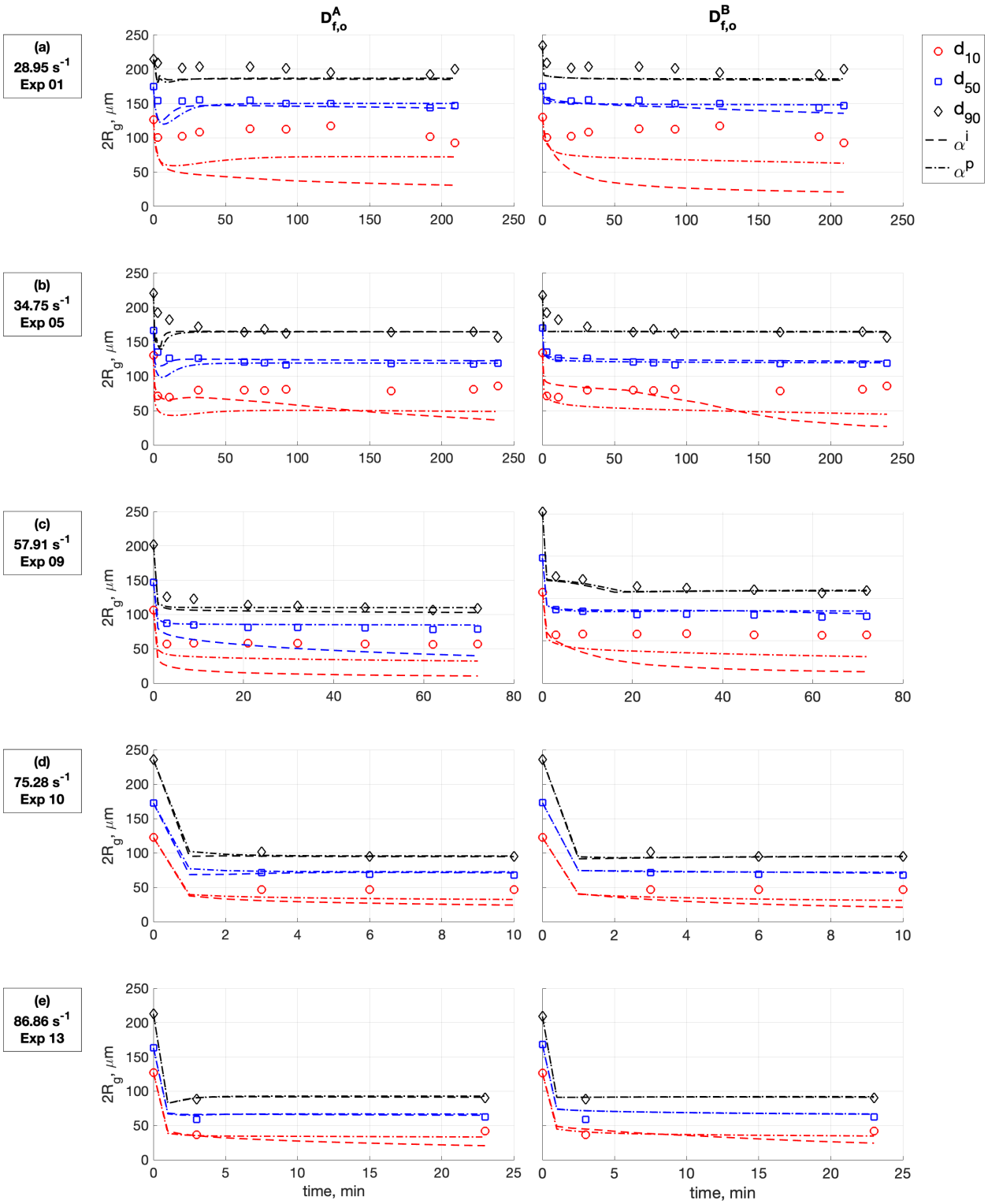

Figure 4.7: Evolution of aggregate size distribution at different shear rates. The symbols $\{\circ, \square, \diamond\}$ represent the percentiles $\{d_{10}, d_{50}, d_{90}\}$, whereas the dashed lines $(--)$ and dash-dotted lines $(-\cdot)$ represent PB results for α^{i} and α^{p} collision models, respectively.

Visual observations of the FSD evolution with time were quantitatively verified by calculating the absolute relative error ($\overline{|E_r|}$) of the percentiles d_{10}, d_{50}, and d_{90} for each case study, which is displayed in Table 4.3. From these results, we conclude that Case Study 4 is the one that best models the evolution of aggregate size and morphology over time. This case study uses $D^B_{f,o}$ is initial fractal dimension and that accounts for the effect of permeability in floc collision, using α^{p}.

Table 4.3: Average absolute relative error ($\overline{|E_r|}$) of the percentiles d_{10}, d_{50}, and d_{90} for the four PBM case studies at different shear rates. Results are in (%).

			Shear rate G (s^{-1})				
			28.95	34.75	57.91	75.38	86.86
$D^A_{f,o}$	α^{i}	$\overline{\lvert E_r\rvert}_{d_{10}}$	47.14	13.74	15.10	9.38	5.81
		$\overline{\lvert E_r\rvert}_{d_{50}}$	3.99	1.85	4.78	0.79	1.56
		$\overline{\lvert E_r\rvert}_{d_{90}}$	5.82	1.62	1.54	0.38	0.63
	α^{p}	$\overline{\lvert E_r\rvert}_{d_{10}}$	28.42	10.07	7.96	5.53	2.69
		$\overline{\lvert E_r\rvert}_{d_{50}}$	4.14	1.86	1.92	1.22	1.61
		$\overline{\lvert E_r\rvert}_{d_{90}}$	5.59	1.89	1.38	0.38	0.87
$D^B_{f,o}$	α^{i}	$\overline{\lvert E_r\rvert}_{d_{10}}$	50.49	15.58	13.52	9.33	6.31
		$\overline{\lvert E_r\rvert}_{d_{50}}$	3.95	1.92	1.78	1.14	1.77
		$\overline{\lvert E_r\rvert}_{d_{90}}$	5.64	0.98	0.93	0.27	0.65
	α^{p}	$\overline{\lvert E_r\rvert}_{d_{10}}$	26.18	7.89	7.68	5.46	3.22
		$\overline{\lvert E_r\rvert}_{d_{50}}$	2.79	2.26	1.88	1.21	1.69
		$\overline{\lvert E_r\rvert}_{d_{90}}$	4.98	1.15	1.02	0.25	0.72

4.2.4 Fitting parameters

Table 4.4 presents the average values and standard deviation of the fitting parameter s (from the breakage distribution function) for the PBM Case Study 4, which best modelled Cifuentes' [17] breakage experiments. Since s is considerably larger than zero for all shear rates, i.e., $s \gg 0$, this confirms our hypothesis that the breakage of flocs with $D_f \geq 2.2$ is not symmetric. Also, since the value of $\overline{s}$ is not close to 1, the driving breakage mechanism is non-uniform. This finding is particularly important because it refutes the assumption that the floc breakage is always symmetric in shear-induced aggregation [11, 18, 19, 22, 36, 37, 41, 42].

Table 4.4: Average values of the fitting parameter s (from the breakage distribution function) at different shear rates for Case Study 4, which used $D_{f,o}^{B}$ for initial fractal dimension and α^{p} for the collision efficiency.

G (s^{-1})	$\overline{s}$
28.95	0.45 ± 0.17
24.75	0.51 ± 0.08
57.91	0.59 ± 0.16
75.38	0.80 ± 0.10
86.86	0.54 ± 0.12

To investigate the physical meaning of B, the values of this fitting parameter from Case Study 4 are plotted against the Reynolds number of the average floc size at steady-state. This Reynolds number is defined as $\mathrm{Re}_{D_{32}}^{ss} = \nu^{-1}\, G \left(D_{32}^{ss}\right)^2$, which accounts for the fluid flow properties (viscosity and shear rate), as well as the average floc size. As shown in Figure 4.8, the parameter B increases with the floc population Reynolds number, and this behaviour can be modelled by the power-law relationship

$$B = 1 \cdot 10^{-12} \left(\mathrm{Re}_{D_{32}}^{ss}\right)^{1.95} \quad ; \quad R^2 = 0.951 \tag{4.1}$$

These results suggest that the critical shear rate that causes floc breakage (3.26) is proportional to the Reynolds number, i.e., $G_{b,i} \propto \mathrm{Re}_{D_{32}}^{ss}$. Equation 4.1 also indicates that the scaling exponent from the floc strength power-law correlation, i.e., $R_g^{ss} \propto G^{-p}$, is $p \approx 0.5$ for the aggregates of Cifuentes' [17] experiments. Since the proportionality constant of Equation 4.1 is $1 \cdot 10^{-12}$ $\mathrm{m}^4\,\mathrm{s}^{-2}$, the fitting parameter B does not scale with $\mathrm{Re}_{D_{32}}^{ss}$. This indicates that there might exist other physical parameters that affect B, and thus further investigations are required fully to understand the physical meaning of B. Nevertheless, Equation 4.1 can be used in future PBM studies on colloidal aggregation and breakage to provide the initial guess of B for the modelling of experiments.

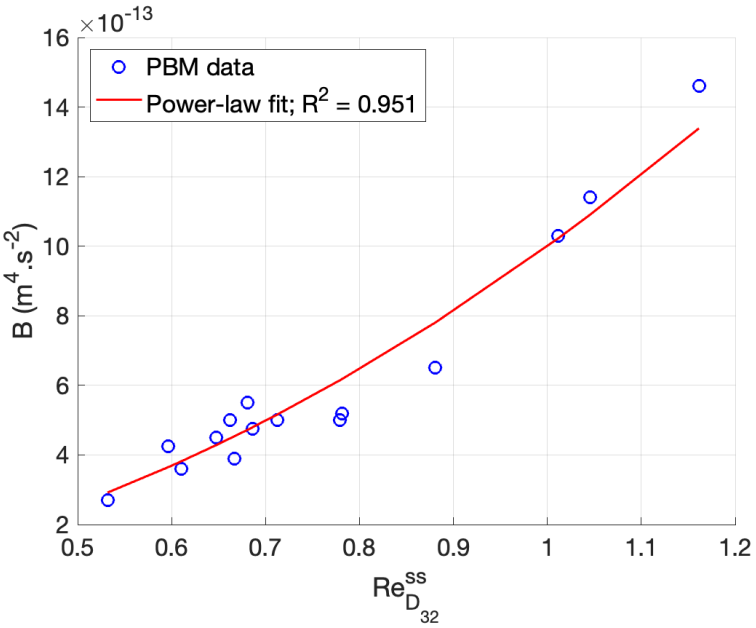

Figure 4.8: The fitting parameter B (from the breakage kernel) is a function of the Reynolds number of the average floc size at steady-state, i.e., $\mathrm{Re}_{D_{32}}^{ss} = \nu^{-1} G \left(d_{32}^{ss}\right)^2$.

Chapter 5

Conclusions and Recommendations

This chapter provides a summary of the major conclusions and novel contributions from this research project, and it lays out the recommendations for future studies.

5.1 Major conclusions

In the present work, the breakage and restructuring of colloidal aggregates in laminar shear flow were investigated through a population balance model (PBM) approach. The time evolution of the average size (D_{32}/d_o), the floc size distribution (d_{10}, d_{50}, d_{90}), and the morphology (D_f) of populations of aggregates from Cifuentes' [17] breakage experiments were modelled. The following conclusions were obtained from the PBM analysis:

- In Cifuentes' [17] breakage experiments, where there was a step increase in the shear rate, the colloidal aggregates experienced rapid densification followed by a long-term elongation. From PBM results, it was observed that the initial densification can be assumed instantaneous, i.e., it occurs as soon as the shear rate is increased. This assumption allows the PBM to model the long-term elongation of flocs, which produces more accurate predictions of the evolution of the floc average diameter and floc size distribution (FSD) over time.
- The influence of floc permeability on the collision efficiency of flocs was investigated by comparing the PBM results for two different collision scenarios, one that modelled permeable floc collisions and the other that modelled impermeable floc collisions. The PBM predictions of average floc size and percentiles d_{50} and d_{90} were approximately the same for the two collision models, but d_{10} was considerably underestimated in the case of impermeable floc collisions. These results reveal that floc permeability plays an

important role in the prediction of collisions between small aggregates and it should be accounted for when the parameter of interest is the FSD.

- The effect of different breakage mechanisms on the FSD was investigated in this work by developing a new breakage distribution function. From the PBM results, it was observed that floc collisions are not symmetric or uniform. Instead, they are non-uniform, where fragments of different sizes have different chances of occurring. This important finding refutes the simplifying assumption made by most PBMs in colloidal aggregation that flocs can only break symmetrically; that is, into two fragments of equal sizes [11, 18, 19, 22, 36, 37, 41, 42].
- The physical meaning of the fitting parameter B from the breakage kernel was investigated in this work. The PBM results revealed that B is a function of the floc population Reynolds number at steady-state, i.e., $B = f(\mathrm{Re}_{D_{32}}^{ss})$. This important relationship confirms our assumption that the scaling exponent of the aggregate strength correlation, $R_g \propto G^{-p}$, is $p = 0.5$ for the aggregates from Cifuentes' [17] experiments. Additionally, the function $B = f(\mathrm{Re}_{D_{32}}^{ss})$ can be used to obtain the initial guess of B in PBM simulations.

5.2 Novel contributions

As explained in Chapters 1 and 2, there is a large body of scientific literature on shear-induced aggregation due to its importance to the separation of colloidal particles from solid-liquid systems. However, only a few studies have focused on understanding the breakage and restructuring mechanisms, which can also occur during aggregation. To the author's knowledge, there are no PBM investigations of floc breakage and restructuring. Therefore, the major goal of this work was to fill this research gap by modelling these two mechanisms via PBM. To achieve this goal, several modifications were proposed to the aggregation and breakage kernels of existing PBMs to model Cifuentes' [17] breakage experiments. These modifications can be summarized as follows:

- A new breakage distribution function was developed to investigate the effect of different breakage mechanisms on the FSD. This function allows the PBM to predict the FSD of colloidal aggregates at different shear rates. This was confirmed by comparing the PBM and experimental results for the percentiles d_{10}, d_{50}, and d_{90}, and the mode of

the FSD at steady-state. The new breakage distribution function can now be used in future PBMs to model the FSD of colloidal aggregates in shear-induced aggregation.

- A new collision efficiency equation was proposed in this work, which can model two different floc collisions mechanisms: one that considers the permeability of flocs based on the shell-core model from Kusters et al. [60], and the other that models flocs as solid rigid spheres, which is based on the CFD simulations at finite Reynolds numbers from Kroll-Rabotin [2]. Concerning the collisions between permeable flocs, our collision efficiency model accounts for the effect of floc restructuring, where the collision efficiency varies with the fractal dimension. This behaviour was neglected in previous approximations of Kusters' [60] original model that were proposed by Selomulya et al. [18] and Vlieghe et al. [77].

5.3 Recommendations for future work

The current work increased the fundamental understanding of how the breakage and restructuring mechanisms occur at a statistical level, i.e., for populations of colloidal aggregates. Since this was the first time that a PBM was used to predict the behaviour of aggregates from breakage experiments, the experiments modelled in this work were performed at ideal conditions, e.g., they were carried out under laminar shear flow and at very dilute solid concentrations. The goal of this experimental setup was to study the isolated effect of shear on the breakage and restructuring mechanisms and to be able to characterize the hydrodynamic and cohesive forces with accuracy. However, these experimental conditions are seldom used in industry. In fact, most shear-induced aggregation systems operate at turbulent flow conditions with high solid concentrations, and they often use polymer flocculants as chemical destabilizers because they can form stronger aggregates; that is, flocs that are less prone to break [11, 22]. Hence, future studies could investigate the aggregation, breakage, and restructuring mechanisms via PBM for more realistic experimental conditions. The following list provides some ideas for future PBM investigations in this research area:

- Investigate the effect of solids concentration and fluid rheology on the breakage and restructuring of aggregates in laminar shear flows.
- Study the dominant breakage mechanism of populations of aggregates in turbulent flows at dilute solid volume concentrations.

- Investigate the effect of different polymer flocculants on the modelling of floc collisions and the breakage kernel.
- Model the FSD of experiments where the shear-induced aggregation is favoured over breakage.

The size and structure of the populations of aggregates studied in this work were characterized by the radius of gyration (R_g) and the mass fractal dimension (D_f), respectively. While R_g is a local property, i.e., it can be measured for each observed aggregate, D_f is a global parameter: that is, the morphology of the floc populations is represented using a single value of D_f over time. From our PBM results, it was observed that the initial fractal dimension was not reproducible among experiments at the same shear rate, and we believe that this is related to the inaccuracy of approximating the morphology of floc populations by a single value. Hence, there is a need for new experimental techniques to determine the local D_f. Liang et al. [53] provided a great summary of different parameters that can be used to track the local morphology of flocs based on other physical parameters, e.g., the convexity and circularity. These morphological parameters have been recently used to investigate the distribution of floc morphology in sequenced flocculation [49] and turbulent aggregation [48]. Therefore, there is the potential in future works to establish accurate correlations between the local D_f and the circularity and convexity of flocs, which can increase the accuracy of PBMs.

References

[1] Diógenes R. L. Vedoy and João B. P. Soares. "Water-soluble polymers for oil sands tailing treatment: A Review." In: *The Canadian Journal of Chemical Engineering* 93.5 (May 2015), pp. 888–904. ISSN: 00084034. DOI: 10.1002/cjce.22129. URL: https://onlinelibrary.wiley.com/doi/10.1002/cjce.22129 (visited on 06/20/2022).

[2] Jean-Sébastien Kroll-Rabotin et al. "Multiscale Simulation of Non-Metallic Inclusion Aggregation in a Fully Resolved Bubble Swarm in Liquid Steel." In: *Metals* 10.4 (Apr. 17, 2020), p. 517. ISSN: 2075-4701. DOI: 10.3390/met10040517. URL: https://www.mdpi.com/2075-4701/10/4/517 (visited on 05/26/2021).

[3] Yicheng Long, Tadeusz Dabros, and Hassan Hamza. "Structure of water/solids/asphaltenes aggregates and effect of mixing temperature on settling rate in solvent-diluted bitumen." In: *Fuel* 83.7 (May 2004), pp. 823–832. ISSN: 00162361. DOI: 10.1016/j.fuel.2003.10.026. URL: https://linkinghub.elsevier.com/retrieve/pii/S0016236103003521 (visited on 06/20/2022).

[4] Mika Sillanpää et al. "Removal of natural organic matter in drinking water treatment by coagulation: A comprehensive review." In: *Chemosphere* 190 (Jan. 2018), pp. 54–71. ISSN: 00456535. DOI: 10.1016/j.chemosphere.2017.09.113. URL: https://linkinghub.elsevier.com/retrieve/pii/S0045653517315382 (visited on 06/20/2022).

[5] C. Selomulya et al. "Aggregation Mechanisms of Latex of Different Particle Sizes in a Controlled Shear Environment." In: *Langmuir* 18.6 (Mar. 1, 2002), pp. 1974–1984. ISSN: 0743-7463, 1520-5827. DOI: 10.1021/la010702h. URL: https://pubs.acs.org/doi/10.1021/la010702h (visited on 12/01/2021).

[6] John Gregory and Charles R. O'Melia. "Fundamentals of flocculation." In: *Critical Reviews in Environmental Control* 19.3 (Jan. 1989), pp. 185–230. ISSN: 1040-838X. DOI: 10.1080/10643388909388365. URL: http://www.tandfonline.com/doi/abs/10.1080/10643388909388365 (visited on 06/20/2022).

[7] Jacob N Israelachvili. *Intermolecular and Surface Forces*. 3rd ed. Elsevier Inc, 2011. 706 pp. ISBN: 978-0-12-391927-4. URL: https://www.elsevier.com/books/intermolecular-and-surface-forces/israelachvili/978-0-12-391927-4.

[8] Volker Becker et al. "Restructuring of colloidal aggregates in shear flows and limitations of the free-draining approximation." In: *Journal of Colloid and Interface Science* 339.2 (Nov. 2009), pp. 362–372. ISSN: 00219797. DOI: 10.1016/j.jcis.2009.07.022. URL:

https://linkinghub.elsevier.com/retrieve/pii/S0021979709009503 (visited on 04/07/2020).

[9] Yogesh M. Harshe, Marco Lattuada, and Miroslav Soos. "Experimental and Modeling Study of Breakage and Restructuring of Open and Dense Colloidal Aggregates." In: *Langmuir* 27.10 (May 17, 2011), pp. 5739–5752. ISSN: 0743-7463, 1520-5827. DOI: 10.1021/la1046589. URL: https://pubs.acs.org/doi/10.1021/la1046589 (visited on 05/27/2021).

[10] Akash Saxena, Jean-Sébastien Kroll-Rabotin, and R. Sean Sanders. "Numerical investigation of the respective roles of cohesive and hydrodynamic forces in aggregate restructuring under shear flow." In: *Journal of Colloid and Interface Science* 608 (Feb. 2022), pp. 355–365. ISSN: 00219797. DOI: 10.1016/j.jcis.2021.08.208. URL: https://linkinghub.elsevier.com/retrieve/pii/S0021979721014442 (visited on 02/04/2022).

[11] Vahid Vajihinejad and João B.P. Soares. "Monitoring polymer flocculation in oil sands tailings: A population balance model approach." In: *Chemical Engineering Journal* 346 (Aug. 2018), pp. 447–457. ISSN: 13858947. DOI: 10.1016/j.cej.2018.04.039. URL: https://linkinghub.elsevier.com/retrieve/pii/S1385894718306041 (visited on 04/07/2020).

[12] Cordelia Selomulya et al. "Evidence of Shear Rate Dependence on Restructuring and Breakup of Latex Aggregates." In: *Journal of Colloid and Interface Science* 236.1 (Apr. 2001), pp. 67–77. ISSN: 00219797. DOI: 10.1006/jcis.2000.7372. URL: https://linkinghub.elsevier.com/retrieve/pii/S0021979700973727 (visited on 12/01/2021).

[13] Farid Vaezi G., R. Sean Sanders, and Jacob H. Masliyah. "Flocculation kinetics and aggregate structure of kaolinite mixtures in laminar tube flow." In: *Journal of Colloid and Interface Science* 355.1 (Mar. 2011), pp. 96–105. ISSN: 00219797. DOI: 10.1016/j.jcis.2010.11.068. URL: https://linkinghub.elsevier.com/retrieve/pii/S0021979710013469 (visited on 04/07/2020).

[14] P. Jarvis et al. "A review of floc strength and breakage." In: *Water Research* 39.14 (Sept. 2005), pp. 3121–3137. ISSN: 00431354. DOI: 10.1016/j.watres.2005.05.022. URL: https://linkinghub.elsevier.com/retrieve/pii/S0043135405002794 (visited on 07/23/2022).

[15] M Boller and Stefan Blaser. "Particles Under Stress." In: 37 (1998), pp. 9–29. DOI: https://doi.org/10.1016/S0273-1223(98)00303-5.

[16] Kento Horii, Reiko Yamada, and Shusaku Harada. "Strength Deterioration of Nonfractal Particle Aggregates in Simple Shear Flow." In: *Langmuir* 31.29 (July 28, 2015), pp. 7909–7918. ISSN: 0743-7463, 1520-5827. DOI: 10.1021/acs.langmuir.5b00197. URL: https://pubs.acs.org/doi/10.1021/acs.langmuir.5b00197 (visited on 07/25/2022).

[17] Gustavo Andres Cifuentes. "Aggregate Breakage in Laminar Couette Flow." M.Sc. thesis. University of Alberta, 2022. 123 pp. URL: https://doi.org/10.7939/r3-zzp7-4t94.

[18] C Selomulya et al. "Understanding the role of restructuring in flocculation: The application of a population balance model." In: *Chemical Engineering Science* (2003), p. 12.

[19] Daniele L. Marchisio et al. "Role of turbulent shear rate distribution in aggregation and breakage processes." In: *AIChE Journal* 52.1 (Jan. 2006), pp. 158–173. ISSN: 0001-1541, 1547-5905. DOI: 10.1002/aic.10614. URL: https://onlinelibrary.wiley.com/doi/10.1002/aic.10614 (visited on 10/22/2021).

[20] Ricardo I. Jeldres, Phillip D. Fawell, and Brendan J. Florio. "Population balance modelling to describe the particle aggregation process: A review." In: *Powder Technology* 326 (Feb. 2018), pp. 190–207. ISSN: 00325910. DOI: 10.1016/j.powtec.2017.12.033. URL: https://linkinghub.elsevier.com/retrieve/pii/S003259101730983X (visited on 10/22/2021).

[21] E. Antunes et al. "Modelling PCC flocculation by bridging mechanism using population balances: Effect of polymer characteristics on flocculation." In: *Chemical Engineering Science* 65.12 (June 2010), pp. 3798–3807. ISSN: 00092509. DOI: 10.1016/j.ces.2010.03.020. URL: https://linkinghub.elsevier.com/retrieve/pii/S0009250910001685 (visited on 11/09/2022).

[22] S. Seghir, A. Hasseine, and M.G. Rasteiro. "Describing the flocculation of PCC particles using population balance modelling approaches." In: *Chemical Engineering Research and Design* 186 (Oct. 2022), pp. 638–646. ISSN: 02638762. DOI: 10.1016/j.cherd.2022.08.038. URL: https://linkinghub.elsevier.com/retrieve/pii/S0263876222004506 (visited on 09/20/2022).

[23] Raffaele Mezzenga et al. "Understanding foods as soft materials." In: *Nature Materials* 4.10 (Oct. 2005), pp. 729–740. ISSN: 1476-1122, 1476-4660. DOI: 10.1038/nmat1496. URL: https://www.nature.com/articles/nmat1496 (visited on 12/08/2022).

[24] Lucrèce Nicoud et al. "A multiscale view of therapeutic protein aggregation: A colloid science perspective." In: *Biotechnology Journal* 10.3 (Mar. 2015), pp. 367–378. ISSN: 18606768. DOI: 10.1002/biot.201400858. URL: https://onlinelibrary.wiley.com/doi/10.1002/biot.201400858 (visited on 12/08/2022).

[25] Babkir Ali and Amit Kumar. "Development of life cycle water footprints for oil sands-based transportation fuel production." In: *Energy* 131 (July 2017), pp. 41–49. ISSN: 03605442. DOI: 10.1016/j.energy.2017.05.021. URL: https://linkinghub.elsevier.com/retrieve/pii/S0360544217307752 (visited on 08/04/2022).

[26] K. L. Kasperski and R. J. Mikula. "Waste Streams of Mined Oil Sands: Characteristics and Remediation." In: *Elements* 7.6 (Dec. 1, 2011), pp. 387–392. ISSN: 1811-5209, 1811-5217. DOI: 10.2113/gselements.7.6.387. URL: https://pubs.geoscienceworld.org/elements/article/7/6/387-392/137908 (visited on 08/05/2022).

[27] Jacob H. Masliyah et al. *Handbook on Theory and Practice of Bitumen Recovery from Athabasca Oil Sands*. Vol. 2. 2 vols. Kingsley Knowledge Publishing, Jan. 2013. ISBN: 978-1-92683203.

[28] Jacob H. Masliyah, Jan Czarnecki, and Xu Zhenghe. *Handbook on Theory and Practice of Bitumen Recovery from Athabasca Oil Sands*. Vol. 1. 2 vols. Kingsley Knowledge Publishing, Jan. 2011. ISBN: 978-1-92683203.

[29] Richard A. Frank et al. "Profiling Oil Sands Mixtures from Industrial Developments and Natural Groundwaters for Source Identification." In: *Environmental Science & Technology* 48.5 (Mar. 4, 2014), pp. 2660–2670. ISSN: 0013-936X, 1520-5851. DOI: 10.1021/es500131k. URL: https://pubs.acs.org/doi/10.1021/es500131k (visited on 08/05/2022).

[30] Pierre Gosselin et al. *Environmental and health impacts of canada's oil sands industry, (2010)*. The Royal Society of Canada, Oct. 2010. URL: https://rsc-src.ca/en/environmental-and-health-impacts-canadas-oil-sands-industry.

[31] Ravi Neelakantan, Farid Vaezi G., and R. Sean Sanders. "Effect of shear on the yield stress and aggregate structure of flocculant-dosed, concentrated kaolinite suspensions." In: *Minerals Engineering* 123 (July 2018), pp. 95–103. ISSN: 08926875. DOI: 10.1016/j.mineng.2018.03.016. URL: https://linkinghub.elsevier.com/retrieve/pii/S0892687518301237 (visited on 05/19/2022).

[32] Lifeng Zhang and Brian G. Thomas. "State of the Art in Evaluation and Control of Steel Cleanliness." In: *ISIJ International* 43.3 (2003), pp. 271–291. ISSN: 0915-1559. DOI: 10.2355/isijinternational.43.271. URL: http://www.jstage.jst.go.jp/article/isijinternational1989/43/3/43_3_271/_article (visited on 06/21/2022).

[33] Jean-Pierre Bellot et al. "Toward Better Control of Inclusion Cleanliness in a Gas Stirred Ladle Using Multiscale Numerical Modeling." In: *Materials* 11.7 (July 10, 2018), p. 1179. ISSN: 1996-1944. DOI: 10.3390/ma11071179. URL: http://www.mdpi.com/1996-1944/11/7/1179 (visited on 06/21/2022).

[34] Elisabete Antunes et al. "Use of New Branched Cationic Polyacrylamides to Improve Retention and Drainage in Papermaking." In: *Industrial & Engineering Chemistry Research* 47.23 (Dec. 3, 2008), pp. 9370–9375. ISSN: 0888-5885, 1520-5045. DOI: 10.1021/ie801216t. URL: https://pubs.acs.org/doi/10.1021/ie801216t (visited on 12/07/2022).

[35] Martin A. Hubbe and Robert A. Gill. "Fillers for Papermaking: A Review of their Properties, Usage Practices, and their Mechanistic Role." In: *BioResources* 11.1 (Feb. 2, 2016), pp. 2886–2963. ISSN: 1930-2126. DOI: 10.15376/biores.11.1.2886-2963. URL: http://ojs.cnr.ncsu.edu/index.php/BioRes/article/view/8676 (visited on 12/08/2022).

[36] Ricardo I. Jeldres, Fernando Concha, and Pedro G. Toledo. "Population balance modelling of particle flocculation with attention to aggregate restructuring and permeability." In: *Advances in Colloid and Interface Science* 224 (Oct. 2015), pp. 62–71. ISSN: 00018686. DOI: 10.1016/j.cis.2015.07.009. URL: https://linkinghub.elsevier.com/retrieve/pii/S0001868615001153 (visited on 05/27/2021).

[37] Eleonora Bonanomi et al. "Analysis and Control of a Turbulent Coagulator." In: *Industrial & Engineering Chemistry Research* 43.19 (Sept. 1, 2004), pp. 6112–6124. ISSN: 0888-5885, 1520-5045. DOI: 10.1021/ie034236y. URL: https://pubs.acs.org/doi/10.1021/ie034236y (visited on 09/20/2022).

[38] Debashish Saha et al. "Breakup of Finite-Size Colloidal Aggregates in Turbulent Flow Investigated by Three-Dimensional (3D) Particle Tracking Velocimetry." In: *Langmuir* 32.1 (Jan. 12, 2016), pp. 55–65. ISSN: 0743-7463, 1520-5827. DOI: 10.1021/acs.langmuir.5b03804. URL: https://pubs.acs.org/doi/10.1021/acs.langmuir.5b03804 (visited on 05/27/2021).

[39] Stefan Blaser. "Flocs in Shear and Strain Flows." In: *Journal of Colloid and Interface Science* 225.2 (May 2000), pp. 273–284. ISSN: 00219797. DOI: 10.1006/jcis.1999.6671. URL: https://linkinghub.elsevier.com/retrieve/pii/S0021979799966717 (visited on 07/25/2022).

[40] Akash Saxena, Jean-Sébastien Kroll-Rabotin, and R. Sean Sanders. "Numerical investigation of the respective roles of cohesive and hydrodynamic forces in aggregate restructuring under shear flow." PhD thesis. 2022.

[41] L. Wang et al. "CFD simulation of aggregation and breakage processes in laminar Taylor–Couette flow." In: *Journal of Colloid and Interface Science* 282.2 (Feb. 2005), pp. 380–396. ISSN: 00219797. DOI: 10.1016/j.jcis.2004.08.127. URL: https://linkinghub.elsevier.com/retrieve/pii/S0021979704008409 (visited on 10/22/2021).

[42] Miroslav Soos, Jan Sefcik, and Massimo Morbidelli. "Investigation of aggregation, breakage and restructuring kinetics of colloidal dispersions in turbulent flows by population balance modeling and static light scattering." In: *Chemical Engineering Science* 61.8 (Apr. 2006), pp. 2349–2363. ISSN: 00092509. DOI: 10.1016/j.ces.2005.11.001. URL: https://linkinghub.elsevier.com/retrieve/pii/S000925090500833X (visited on 10/22/2021).

[43] R. C. Sonntag and W. B. Russel. "Structure and Breakup of Flocs Subjected to Fluid Stresses: I. Shear Experiments." In: 113.2 (1986), pp. 399–413. DOI: https://doi.org/10.1016/0021-9797(86)90175-X.

[44] John Gregory. "The density of particle aggregates." In: (1997), p. 13.

[45] S. Lazzari et al. "Fractal-like structures in colloid science." In: *Advances in Colloid and Interface Science* 235 (Sept. 2016), pp. 1–13. ISSN: 00018686. DOI: 10.1016/j.cis.2016.05.002. URL: https://linkinghub.elsevier.com/retrieve/pii/S0001868615300567 (visited on 05/17/2022).

[46] Teresa Serra and Xavier Casamitjana. "Structure of the Aggregates During the Process of Aggregation and Breakup Under a Shear Flow." In: *Journal of Colloid and Interface Science* 206.2 (Oct. 1998), pp. 505–511. ISSN: 00219797. DOI: 10.1006/jcis.1998.5714. URL: https://linkinghub.elsevier.com/retrieve/pii/S0021979798957149 (visited on 07/25/2022).

[47] Amgad S. Moussa et al. "Effect of Solid Volume Fraction on Aggregation and Breakage in Colloidal Suspensions in Batch and Continuous Stirred Tanks." In: *Langmuir* 23.4 (Feb. 1, 2007), pp. 1664–1673. ISSN: 0743-7463, 1520-5827. DOI: 10.1021/la062138m. URL: https://pubs.acs.org/doi/10.1021/la062138m (visited on 07/26/2022).

[48] Mélody Vlieghe et al. "*In situ* characterization of floc morphology by image analysis in a turbulent Taylor-Couette reactor." In: *AIChE Journal* 60.7 (July 2014), pp. 2389–2403. ISSN: 00011541. DOI: 10.1002/aic.14431. URL: https://onlinelibrary.wiley.com/doi/10.1002/aic.14431 (visited on 10/22/2021).

[49] Léa Guérin et al. "Dynamics of aggregate size and shape properties under sequenced flocculation in a turbulent Taylor-Couette reactor." In: *Journal of Colloid and Interface Science* 491 (Apr. 2017), pp. 167–178. ISSN: 00219797. DOI: 10.1016/j.jcis.2016.12.042. URL: https://linkinghub.elsevier.com/retrieve/pii/S0021979716310426 (visited on 07/25/2022).

[50] G.C. Bushell et al. "On techniques for the measurement of the mass fractal dimension of aggregates." In: *Advances in Colloid and Interface Science* 95.1 (Jan. 2002), pp. 1–50. ISSN: 00018686. DOI: 10.1016/S0001-8686(00)00078-6. URL: https://linkinghub.elsevier.com/retrieve/pii/S0001868600000786 (visited on 04/07/2020).

[51] Petra Bubakova, Martin Pivokonsky, and Petr Filip. "Effect of shear rate on aggregate size and structure in the process of aggregation and at steady state." In: *Powder Technology* 235 (Feb. 2013), pp. 540–549. ISSN: 00325910. DOI: 10.1016/j.powtec.2012.11.014. URL: https://linkinghub.elsevier.com/retrieve/pii/S0032591012007632 (visited on 10/22/2021).

[52] Lyonel Ehrl, Miroslav Soos, and Marco Lattuada. "Generation and Geometrical Analysis of Dense Clusters with Variable Fractal Dimension." In: *The Journal of Physical Chemistry B* 113.31 (Aug. 6, 2009), pp. 10587–10599. ISSN: 1520-6106, 1520-5207. DOI: 10.1021/jp903557m. URL: https://pubs.acs.org/doi/10.1021/jp903557m (visited on 10/22/2021).

[53] Long Liang et al. "A review of the modern characterization techniques for flocs in mineral processing." In: *Minerals Engineering* 84 (Dec. 2015), pp. 130–144. ISSN: 08926875. DOI: 10.1016/j.mineng.2015.10.011. URL: https://linkinghub.elsevier.com/retrieve/pii/S0892687515301072 (visited on 07/23/2022).

[54] Patrick T. Spicer, Wolfgang Keller, and Sotiris E. Pratsinis. "The Effect of Impeller Type on Floc Size and Structure during Shear-Induced Flocculation." In: *Journal of Colloid and Interface Science* 184.1 (Dec. 1996), pp. 112–122. ISSN: 00219797. DOI: 10.1006/jcis.1996.0601. URL: https://linkinghub.elsevier.com/retrieve/pii/S0021979796906013 (visited on 01/12/2023).

[55] Graziano Frungieri and Marco Vanni. "Aggregation and breakup of colloidal particle aggregates in shear flow: A combined Monte Carlo - Stokesian dynamics approach." In: *Powder Technology* 388 (Aug. 2021), pp. 357–370. ISSN: 00325910. DOI: 10.1016/j.powtec.2021.04.076. URL: https://linkinghub.elsevier.com/retrieve/pii/S0032591021003636 (visited on 07/25/2022).

[56] Yogesh M. Harshe and Marco Lattuada. "Universal Breakup of Colloidal Clusters in Simple Shear Flow." In: *The Journal of Physical Chemistry B* 120.29 (July 28, 2016), pp. 7244–7252. ISSN: 1520-6106, 1520-5207. DOI: 10.1021/acs.jpcb.6b03220. URL: https://pubs.acs.org/doi/10.1021/acs.jpcb.6b03220 (visited on 05/27/2021).

[57] Christopher M. Sorensen and Gregory C. Roberts. "The Prefactor of Fractal Aggregates." In: *Journal of Colloid and Interface Science* 186.2 (Feb. 1997), pp. 447–452. ISSN: 00219797. DOI: 10.1006/jcis.1996.4664. URL: https://linkinghub.elsevier.com/retrieve/pii/S0021979796946640 (visited on 10/26/2022).

[58] *Engineering Statistics Handbook*. NIST, 2012. URL: https://doi.org/10.18434/M32189.

[59] Henk G. Merkus. *Particle size measurements: fundamentals, practice, quality*. Particle technology series v. 17. OCLC: ocn244766026. New York: Springer, 2009. 533 pp. ISBN: 978-1-4020-9015-8 978-1-4020-9016-5.

[60] Karl A. Kusters, Johan G. Wijers, and Dirk Thoenes. "Aggregation kinetics of small particles in agitated vessels." In: *Chemical Engineering Science* 52.1 (Jan. 1997), pp. 107–121. ISSN: 00092509. DOI: 10.1016/S0009-2509(96)00375-2. URL: https://linkinghub.elsevier.com/retrieve/pii/S0009250996003752 (visited on 03/01/2022).

[61] H.C. Hamaker. "The London—van der Waals attraction between spherical particles." In: *Physica* 4.10 (Oct. 1937), pp. 1058–1072. ISSN: 00318914. DOI: 10.1016/S0031-8914(37)80203-7. URL: https://linkinghub.elsevier.com/retrieve/pii/S0031891437802037 (visited on 04/07/2020).

[62] John C. Berg. *An introduction to interfaces & colloids: the bridge to nanoscience*. OCLC: ocn498932462. Singapore ; Hackensack, NJ: World Scientific, 2010. 785 pp. ISBN: 978-981-4299-82-4 978-981-4293-07-5.

[63] P.M Adler. "Heterocoagulation in shear flow." In: *Journal of Colloid and Interface Science* 83.1 (Sept. 1981), pp. 106–115. ISSN: 00219797. DOI: 10.1016/0021-9797(81)90015-1. URL: https://linkinghub.elsevier.com/retrieve/pii/0021979781900151 (visited on 02/11/2022).

[64] Ko Higashitani et al. "Kinetic theory of shear coagulation for particles in a viscous fluid." In: *JOURNAL OF CHEMICAL ENGINEERING OF JAPAN* 15.4 (1982), pp. 299–304. ISSN: 0021-9592, 1881-1299. DOI: 10.1252/jcej.15.299. URL: http://www.jstage.jst.go.jp/article/jcej1968/15/4/15_4_299/_article (visited on 11/04/2022).

[65] John P. Pantina and Eric M. Furst. "Elasticity and Critical Bending Moment of Model Colloidal Aggregates." In: *Physical Review Letters* 94.13 (Apr. 7, 2005), p. 138301. ISSN: 0031-9007, 1079-7114. DOI: 10.1103/PhysRevLett.94.138301. URL: https://link.aps.org/doi/10.1103/PhysRevLett.94.138301 (visited on 07/07/2022).

[66] Pijush K. Kundu, Ira M. Cohen, and David R. Dowling. *Fluid mechanics*. 5th ed. OCLC: ocn713567396. Waltham, MA: Academic Press, 2012. 891 pp. ISBN: 978-0-12-382100-3.

[67] Yunus A. Çengel and John M. Cimbala. *Fluid mechanics: fundamentals and applications*. Third edition. New York: McGraw Hill, 2014. 1000 pp. ISBN: 978-0-07-338032-2.

[68] Marco Vanni. "Accurate modelling of flow induced stresses in rigid colloidal aggregates." In: *Computer Physics Communications* 192 (July 2015), pp. 70–90. ISSN: 00104655. DOI: 10.1016/j.cpc.2015.02.022. URL: https://linkinghub.elsevier.com/retrieve/pii/S0010465515000806 (visited on 03/24/2021).

[69] Marco Vanni and Andrea Gastaldi. "Hydrodynamic Forces and Critical Stresses in Low-Density Aggregates under Shear Flow." In: *Langmuir* 27.21 (Nov. 1, 2011), pp. 12822–12833. ISSN: 0743-7463, 1520-5827. DOI: 10.1021/la2024549. URL: https://pubs.acs.org/doi/10.1021/la2024549 (visited on 05/19/2022).

[70] Doraiswami Ramkrishna. *Population Balances: Theory and Applications to Particulate Systems in Engineering*. 1st. Academic Press, 2000. ISBN: 978-0-08-053924-9. URL: https://www.elsevier.com/books/population-balances/ramkrishna/978-0-12-576970-9.

[71] M. V. Smoluchowski. "Versuch einer mathematischen Theorie der Koagulations-Kinetic Kolloider Losungen." In: 92 (1917), pp. 129–168.

[72] C. Selomulya. "The Effect Of Shear On Flocculation And Floc Size/Structure." PhD thesis. The University Of New South Wales, 2001.

[73] Patrick T. Spicer and Sotiris E. Pratsinis. "Coagulation and fragmentation: Universal steady-state particle-size distribution." In: *AIChE Journal* 42.6 (June 1996), pp. 1612–1620. ISSN: 0001-1541, 1547-5905. DOI: 10.1002/aic.690420612. URL: https://onlinelibrary.wiley.com/doi/10.1002/aic.690420612 (visited on 08/12/2021).

[74] Guan Heng Yeoh, Chi Pok Cheung, and Jiyuan Tu. *Multiphase Flow Analysis Using Population Balance Modeling*. https://doi.org/10.1016/C2011-0-05568-0. Elsevier, 2014. ISBN: 978-0-08-098229-8. URL: https://www.sciencedirect.com/book/9780080982298/multiphase-flow-analysis-using-population-balance-modeling (visited on 03/25/2022).

[75] M. J. Hounslow, R. L. Ryall, and V. R. Marshall. "A discretized population balance for nucleation, growth, and aggregation." In: *AIChE Journal* 34.11 (Nov. 1988), pp. 1821–1832. ISSN: 0001-1541, 1547-5905. DOI: 10.1002/aic.690341108. URL: https://onlinelibrary.wiley.com/doi/10.1002/aic.690341108 (visited on 10/22/2021).

[76] Daniele L. Marchisio, R.Dennis Vigil, and Rodney O. Fox. "Quadrature method of moments for aggregation–breakage processes." In: *Journal of Colloid and Interface Science* 258.2 (Feb. 2003), pp. 322–334. ISSN: 00219797. DOI: 10.1016/S0021-9797(02)00054-1. URL: https://linkinghub.elsevier.com/retrieve/pii/S0021979702000541 (visited on 10/22/2021).

[77] Mélody Vlieghe et al. "QMOM-based population balance model involving a fractal dimension for the flocculation of latex particles." In: *Chemical Engineering Science* 155 (Nov. 2016), pp. 65–82. ISSN: 00092509. DOI: 10.1016/j.ces.2016.07.044. URL: https://linkinghub.elsevier.com/retrieve/pii/S0009250916304183 (visited on 10/22/2021).

[78] Daniele L. Marchisio et al. "Quadrature method of moments for population-balance equations." In: *AIChE Journal* 49.5 (May 2003), pp. 1266–1276. ISSN: 00011541, 15475905. DOI: 10.1002/aic.690490517. URL: https://onlinelibrary.wiley.com/doi/10.1002/aic.690490517 (visited on 10/22/2021).

[79] Daniele L. Marchisio, R. Dennis Vigil, and Rodney O. Fox. "Implementation of the quadrature method of moments in CFD codes for aggregation–breakage problems." In: *Chemical Engineering Science* 58.15 (Aug. 2003), pp. 3337–3351. ISSN: 00092509. DOI: 10.1016/S0009-2509(03)00211-2. URL: https://linkinghub.elsevier.com/retrieve/pii/S0009250903002112 (visited on 10/22/2021).

[80] C. Coufort and A. Line. "Forces on Spherical Particles in Terms of Upstream Flow Characteristics." In: *Chemical Engineering Research and Design* 81.9 (Oct. 2003), pp. 1206–1211. ISSN: 02638762. DOI: 10.1205/026387603770866399. URL: https://linkinghub.elsevier.com/retrieve/pii/S0263876203724186 (visited on 08/15/2022).

[81] Motoyoshi Kobayashi, Yasuhisa Adachi, and Setsuo Ooi. "Breakup of Fractal Flocs in a Turbulent Flow." In: *Langmuir* 15.13 (June 1, 1999), pp. 4351–4356. ISSN: 0743-7463, 1520-5827. DOI: 10.1021/la980763o. URL: https://pubs.acs.org/doi/10.1021/la980763o (visited on 07/25/2022).

[82] Lyonel Ehrl, Miroslav Soos, and Massimo Morbidelli. "Dependence of Aggregate Strength, Structure, and Light Scattering Properties on Primary Particle Size under Turbulent Conditions in Stirred Tank." In: *Langmuir* 24.7 (Apr. 1, 2008), pp. 3070–3081. ISSN: 0743-7463, 1520-5827. DOI: 10.1021/la7032302. URL: https://pubs.acs.org/doi/10.1021/la7032302 (visited on 07/25/2022).

[83] Miroslav Soos et al. "Aggregate Breakup in a Contracting Nozzle." In: *Langmuir* 26.1 (Jan. 5, 2010), pp. 10–18. ISSN: 0743-7463, 1520-5827. DOI: 10.1021/la903982n. URL: https://pubs.acs.org/doi/10.1021/la903982n (visited on 07/25/2022).

[84] Yasuhisa Adachi et al. "Size, orientation, and strength of Na-montmorillonite flocs flowing in a laminar shear flow." In: *Colloid and Polymer Science* 297.7 (Aug. 2019), pp. 979–987. ISSN: 0303-402X, 1435-1536. DOI: 10.1007/s00396-019-04532-3. URL: http://link.springer.com/10.1007/s00396-019-04532-3 (visited on 08/16/2022).

[85] Denis Bouyer, Alain Liné, and Zdravka Do-Quang. "Experimental analysis of floc size distribution under different hydrodynamics in a mixing tank." In: *AIChE Journal* 50.9 (Sept. 2004), pp. 2064–2081. ISSN: 00011541. DOI: 10.1002/aic.10242. URL: https://onlinelibrary.wiley.com/doi/10.1002/aic.10242 (visited on 08/16/2022).

[86] M.L. Eggersdorfer et al. "Fragmentation and restructuring of soft-agglomerates under shear." In: *Journal of Colloid and Interface Science* 342.2 (Feb. 2010), pp. 261–268. ISSN: 00219797. DOI: 10.1016/j.jcis.2009.10.062. URL: https://linkinghub.elsevier.com/retrieve/pii/S0021979709013976 (visited on 08/16/2022).

[87] Martin Kroupa et al. "Size and Structure of Clusters Formed by Shear Induced Coagulation: Modeling by Discrete Element Method." In: *Langmuir* 31.28 (July 21, 2015), pp. 7727–7737. ISSN: 0743-7463, 1520-5827. DOI: 10.1021/acs.langmuir.5b01046. URL: https://pubs.acs.org/doi/10.1021/acs.langmuir.5b01046 (visited on 08/16/2022).

[88] Alessio Zaccone et al. "Breakup of dense colloidal aggregates under hydrodynamic stresses." In: *Physical Review E* 79.6 (June 3, 2009), p. 061401. ISSN: 1539-3755, 1550-2376. DOI: 10.1103/PhysRevE.79.061401. URL: https://link.aps.org/doi/10.1103/PhysRevE.79.061401 (visited on 07/25/2022).

[89] Christopher W. Macosko. *Rheology: principles, measurements, and applications*. Advances in interfacial engineering series. New York: VCH, 1994. 550 pp. ISBN: 978-1-56081-579-2.

[90] G. I. Taylor. "VIII. Stability of a viscous liquid contained between two rotating cylinders." In: *The Royal Society* 223.605 (1923), pp. 289–343. DOI: 10.1098/rsta.1923.0008.

[91] Dennis C Prieve and William B Russel. "Simplified predictions of Hamaker constants from Lifshitz theory." In: *Journal of Colloid and Interface Science* 125.1 (Sept. 1988), pp. 1–13. ISSN: 00219797. DOI: 10.1016/0021-9797(88)90048-3. URL: https://linkinghub.elsevier.com/retrieve/pii/0021979788900483 (visited on 01/04/2023).

[92] J F Brady and G Bossis. "Stokesian Dynamics." In: (), p. 47.

[93] Matthieu Gisselbrecht. "Simulation des interactions hydrodynamiques entre inclusions dans un métal liquide: établissement de noyaux d'agrégation dans les conditions représentatives du procédé de flottation." PhD thesis. Université de Lorraine, Oct. 2019. 177 pp.

[94] T. G. M. van de Ven and S. G. Mason. "The microrheology of colloidal dispersions VII. Orthokinetic doublet formation of spheres." In: *Colloid and Polymer Science* 255.5 (May 1977), pp. 468–479. ISSN: 0303-402X, 1435-1536. DOI: 10.1007/BF01536463. URL: http://link.springer.com/10.1007/BF01536463 (visited on 11/04/2022).

[95] P.M Adler. "Streamlines in and around porous particles." In: (1981).

[96] R. C. Sonntag and W. B. Russel. "Structure and Breakup of Flocs Subjected to Fluid Stresses: II. Theory." In: 115.2 (1987), pp. 378–389.

[97] M. Soos et al. "Population balance modeling of aggregation and breakage in turbulent Taylor–Couette flow." In: *Journal of Colloid and Interface Science* 307.2 (Mar. 2007), pp. 433–446. ISSN: 00219797. DOI: 10.1016/j.jcis.2006.12.016. URL: https://linkinghub.elsevier.com/retrieve/pii/S0021979706011234 (visited on 10/22/2021).

[98] Michael A. Delichatsios and Ronald F. Probstein. "The Effect of Coalescence on the Average Drop Size in Liquid-Liquid Dispersions." In: *Industrial & Engineering Chemistry Fundamentals* 15.2 (May 1976), pp. 134–138. ISSN: 0196-4313, 1541-4833. DOI: 10.1021/i160058a010. URL: https://pubs.acs.org/doi/abs/10.1021/i160058a010 (visited on 11/10/2021).

[99] KA Karl Kusters. "The influence of turbulence on aggregation of small particles in agitated vessels." Publisher: Technische Universiteit Eindhoven. PhD thesis. 1991. URL: https://research.tue.nl/en/publications/the-influence-of-turbulence-on-aggregation-of-small-particles-in-agitated-vessels(0e9672f3-d8cb-43ed-9b32-92ddbe7ade38).html (visited on 08/14/2021).

Appendix A

Tagging of experiments

This appendix presents the original tagging system that was used in Cifuentes [17] to label experiments, and it explains how the experiment tags were simplified in his thesis and in the current work. The main objective of this appendix is to clarify this information for future students who will carry on the research on the breakage and restructuring of colloidal aggregates in the Pipeline Transport Processes research group.

Cifuentes [17] completed a total of 30 shear-induced aggregation and breakage experiments, of which 19 were presented in his thesis. The original tagging system of experiments uses the date that they were performed and the run number of that day, e.g., the tags 0416 and 0416_02 corresponds to the first and second experiments conducted in April 16$^{\text{th}}$ of 2021. To facilitate the visualization of results in the present work and in Cifuentes [17], the original tags were simplified to Arabic numerals, e.g., the tag 0416 was reduced to Exp. 04 in the current work. The Table A.1 presents a list with the original and simplified tags of the experiments that were modelled in the current work, as well as their average shear rates.

Table A.1: Original and simplified tags of the experiments modelled in the present work.

Original tag	Simplified tag	Average shear rate, G (s^{-1})
0420	Exp 1	28.95
0422	Exp 2	28.95
0423	Exp 3	28.95
0416	Exp 4	34.75
0414	Exp 5	34.75
0416_02	Exp 6	34.75
0323_01	Exp 7	57.91
0315	Exp 8	57.91
0429	Exp 9	57.91
0331_02	Exp 10	75.28
0406_02	Exp 11	75.28
0407	Exp 12	75.28
0318	Exp 13	86.86
0318_02	Exp 14	86.86
0319	Exp 15	86.86

The results from Cifuentes [17] were divided in two major sections: the Particle Aggregation (Section 4.2); and the Aggregate Breakage (Section 4.3). A total of 15 experiments were presented in each section and their original and simplified tags can be found in Tables A.2 and A.3.

Table A.2: Original and simplified tags of the experiments presented in Section 4.2 (Particle aggregation) of Cifuentes [17].

Original tag	Simplified tag	Average shear rate, G (s^{-1})
0318	Exp 1	28.95
0319	Exp 2	28.95
0331	Exp 3	28.95
0331_02	Exp 4	34.75
0408	Exp 5	34.75
0407	Exp 6	34.75
0409	Exp 7	57.91
0414	Exp 8	57.91
0420	Exp 9	57.91
0421	Exp 10	75.28
0422	Exp 11	75.28
0423	Exp 12	75.28
0430	Exp 13	86.86
0406_02	Exp 14	86.86
0416_02	Exp 15	86.86

Table A.3: Original and simplified tags of the experiments presented in Section 4.3 (Aggregate breakage) of Cifuentes [17].

Original tag	Simplified tag	Average shear rate, G (s^{-1})
0420	Test 1	28.95
0421	Test 2	28.95
0423	Test 3	28.95
0412	Test 1	34.75
0414	Test 2	34.75
0416_02	Test 3	34.75
0312	Test 1	57.91
0315	Test 2	57.91
0429	Test 3	57.91
0407	Test 1	75.28
0331_02	Test 2	75.28
0406_02	Test 3	75.28
0318	Test 1	86.86
0319	Test 2	86.86
0422	Test 3	86.86